INFORMATION TO USERS

This manuscript has been reproduced from the microfilm master. UMI films the text directly from the original or copy submitted. Thus, some thesis and dissertation copies are in typewriter face, while others may be from any type of computer printer.

The quality of this reproduction is dependent upon the quality of the copy submitted. Broken or indistinct print, colored or poor quality illustrations and photographs, print bleedthrough, substandard margins, and improper alignment can adversely affect reproduction.

In the unlikely event that the author did not send UMI a complete manuscript and there are missing pages, these will be noted. Also, if unauthorized copyright material had to be removed, a note will indicate the deletion.

Oversize materials (e.g., maps, drawings, charts) are reproduced by sectioning the original, beginning at the upper left-hand corner and continuing from left to right in equal sections with small overlaps.

ProQuest Information and Learning
300 North Zeeb Road, Ann Arbor, MI 48106-1346 USA
800-521-0600

A momentum-dependent Lattice Hamiltonian model for simulations of heavy ion collisions

by

Declan Persram

Department of Physics
McGill University. Montréal
December 2000

A Thesis submitted to the
Faculty of Graduate Studies and Research
in partial fulfillment of the requirements for the degree of
Doctor of Philosophy

Abstract

We investigate both directed and elliptic flow and linear momentum transfer in intermediate energy heavy ion collisions. The model that we have adapted for this work is the BUU transport equation solved with a momentum-dependent lattice Hamiltonian algorithm. We introduce an extension of this transport model that consistently takes into account the momentum-dependent in-medium modification of the nucleon-nucleon collision cross section. Comparison with linear momentum transfer data favours a soft momentum-dependent nuclear mean field of compressibility K=215 MeV. Analysis of higher energy elliptic flow data favours a momentum-dependent over that of a momentum-independent nuclear mean field. Furthermore, we find that both the linear momentum transfer and elliptic flow data favour an in-medium nucleon-nucleon cross section over the free space cross section.

Résumé

Nous étudions le flot dirigé, le flot elliptique et le transfert d'impulsion linéaire dans les collisions d'ions lourds aux énergies intermédiaires. Pour ce faire, nous avons utilisé un modèle BUU avec un algorithme hamiltonien sur réseau et un champ moyen qui dépend de l'impulsion. Nous généralisons le modèle en introduisant une évaluation self-consistante de la section efficace nucléon-nucléon dans le milieu. Des comparaisons avec des données sur le transfert d'impulsion linéaire suggèrent un champ moyen qui dépend de l'impulsion, avec une compressibilité d'environ 215 MeV. Des résultats conséquents sont obtenus en examinant les résultats de flot elliptique à plus haute énergie. Nous constatons un raprochement global des résultats du modèle avec les données expérimentales avec l'usage de sections efficaces qui découlent du champ moyen avec une dépendance en impulsion.

Acknowledgments

I would like to extend much thanks to all the people who have made the time spent here both enjoyable and enlightening. In particular, I would like to thank my supervisor, Charles Gale, for the help, encouragement and patience provided by him over the last few years without whom, this work would not have been possible. I would also like to thank my parents for their encouragement and support in allowing me to pursue my goals. I am indebted to Subal Das Gupta for invaluable discussions providing me with a deeper understanding of the work presented in this thesis.

During my studies, I twice visited the National Superconducting Cyclotron Laboratory at Michigan State University as a visiting researcher. To this, I owe many thanks to Betty Tsang and Pawel Danielewicz for their interest, encouragement and financial support during those stays. I would also like to extend my thanks to Paul Mercure and Juan Gallego for their invaluable computer support throughout the years.

I would also like to thank my office mates Marko Milek and Claude Théoret, who have provided much comic relief, allowing for a tense-free environment. Much thanks also goes to Susan Moss and other Biftek cronies for keeping me alive. Thanks also to Andy Hare, Imran Rahman, Mike Tan, Dave Winters and Yashar Aghababaie for the many warped table discussions of physics and the life contained within. An additional thanks goes to Andy for proof-reading this thesis and for providing many helpful suggestions.

Statement of Originality

This work completes a five year investigation of intermediate energy heavy ion collisions with the BUU model. The main features of this model as presented in this work are contained in the momentum-dependent lattice Hamiltonian solution for the mean fields. This is the first implementation of such a model and as such has increased the predictive power of the BUU model at low energies. In addition we have, for the first time, implemented a self-consistent in-medium nucleon-nucleon scattering cross section, thus consistently taking into account the effects a momentum-dependent potential has on both the mean field and the in-medium nucleon-nucleon cross section.

Contents

List of Figures

List of Tables

Chapter 1

Introduction

For the past two decades, the study of heavy ion collisions has been very popular. The impetus for this trend arose from the need to better understand the behaviour of matter at extreme densities and/or temperatures. Extreme in this case is defined as matter at and around several times the density of an atomic nucleus. Early nuclear physics experiments led to the discovery of the latter to be about 0.16 nucleons per cubic fm (1 fm=10^{-15} m)[1]. In addition, theoretical modeling of supernovæ and neutron stars implied the need to understand the behaviour of matter up to ten times this density[2, 3, 4]. In these studies, the matter is typically characterized by the compressibility[5, 6, 7] of the equation of state.[1] Furthermore, more recent advances in high energy nuclear physics have predicted the existence of a new state of matter, the quark-gluon plasma, which is also expected to appear at high densities and/or temperatures[8, 9]. Thus, there are many active areas in nuclear physics and astrophysics where the need to understand high density matter is imperative and thus a study of the properties of *nuclear matter*[2] is warranted. To date, the

[1] From here-on we refer to the *incompressibility* coefficient as the *compressibility* K. This quantity is a measure of the change in volume of a system with respect to changes in pressure.

[2] Nuclear matter is formally defined as a uniform collection of an equal number of neutrons and protons extending out to infinity and is an idealization meant to approximate the conditions *inside* a large nucleus.

most practical avenue to embark on a study of dense nuclear matter is via heavy ion collisions.

The term "heavy ion" generally refers to an atomic nucleus with a mass in excess of the alpha particle (nucleus of a helium atom) mass of $A = 4$. Typically however, it refers to an atomic nucleus with 10→200 or more nucleons. A schematic diagram of a heavy ion *collision* is presented chapter 5 in figure 5.1 on page 82. Traditionally, the study of heavy ion collisions was conducted with a single beam of nuclei directed on a fixed target. As higher centre of mass energies were desired, collider geometries were adopted. The energy range available today spans a region of about 5 orders of magnitude from the Coulomb barrier (a few MeV per nucleon) to nucleon-nucleon centre of mass energies of $\sim$ 200 GeV. As the energy range at which collisions of heavy nuclei can be studied is large, many physical mechanisms can enter the picture: from sub-Coulomb barrier fusion at low energies, to single and composite particle production at intermediate energies, to high energy particle production accompanied by complete disassociation of the nuclei at high energies. At ultra-relativistic energies, QCD predicts a phase transition to a new state of matter: the quark-gluon plasma[8]. In an attempt to gain an understanding of the physics at work in these various scenarios, many dynamical models have been developed in the past and we will touch on a few of them.

The Fireball model[10, 11, 12] was an early realization that treated the colliding nuclei thermodynamically. In general, the participant regions were assumed to completely fuse in the initial stages of the collision. The total centre of mass energy present in this quasi-compound-nucleus was then shared among its constituents. The quasi-compound-nucleus was then allowed to expand to some prescribed freeze-out density after which the nucleons were assumed to stream freely into vacuum. The temperature of the system at the freeze-out density determined the momentum spectrum of the system. The Cascade model[13, 14] attempted to include two-body scattering process not present in the Fireball model by treating

the nucleus-nucleus collision as a succession of binary nucleon-nucleon collisions. Although this model does have some success at high energies (in fact, a more sophisticated realization of this idea is presently used to model collisions of ultra-relativistic nuclei), the exclusion of bulk nuclear properties, such as nucleon binding energies results in unrealistic behaviour at low energies, as is also the case with the Fireball model. Other models which have attempted to incorporate effects of the nuclear potential are the time-dependent Hartree-Fock model (TDHF)[15, 16, 17], the quantum-molecular-dynamics model (QMD)[18, 19, 20], and the Boltzmann-Uehling-Uhlenbeck model (BUU)[21, 22]. In the QMD model, the cascade algorithm (for two-body and higher scattering processes) is used in conjunction with a nuclear many-body potential calculated by summing nucleon-nucleon two-body and three-body interactions. The TDHF model treats the nuclear potential in the Hartree-Fock *mean field* approximation[23, 24, 25] originally used in the study of electron plasmas and does not contain *explicit* two-body interactions. The BUU model also uses a mean field nuclear potential. Coupled to this is a cascade algorithm that attempts to build in the nucleon-nucleon collisions. This is the model we adopt in this work.

The main features of the BUU model are the inclusion of a mean (potential energy) field and a cascade algorithm which attempts to model individual nucleon-nucleon collisions. The first accounts for the fact that a nucleon inside a nucleus feels a force due to the presence of the other nucleons. Any realistic description of a nucleus demands this scheme. The nuclear potential in this model is implemented via a *mean field* which, for a single nucleon, is computed by averaging the potential energy contributions from all neighbouring (not necessarily nearest neighbors only) nucleons. The mean field in this case will have nuclear, Coulomb and isospin contributions. Traditionally, the latter two which serve to distinguish the differences between a neutron and a proton were ignored as the BUU model was applied at energies where such effects were minimal. However, for low energy studies, these two effects can become significant and their inclusion is thus necessary. We will discuss

the mean field potential in greater depth in a forthcoming chapter. For now, we point out that although many authors utilize a BUU mean field that depends solely on density, there is strong experimental evidence in favour of a nuclear mean field that depends on both density *and* momentum[26]. In addition, comparison of BUU model simulations with experiment are strongly in favour of a mean field that includes density and momentum dependence as opposed to just a density dependence. We return to this point in chapter 3. For the cascade input, nucleon-nucleon collisions are permitted to occur under certain circumstances. One of these for instance is directly related to the nucleon-nucleon cross section, as the transition rate for two-nucleon scattering processes is directly tied to this quantity. As we shall see shortly, the value of the nucleon-nucleon cross section is modified in the presence of the nuclear medium. In particular, this modification will also depend on the form of the mean field potential[27]. In this work, we adopt a parameterization of the in-medium nucleon-nucleon cross section that is unique to momentum-dependent mean field potentials and show for the first time its relevance in the dynamics of heavy ion collisions. The other condition which must be met is included in order to satisfy symmetry properties of the nucleons, which are half-integer spin fermions. This feature is generally referred to as "Pauli blocking", as it attempts to prevent scattering into occupied states.

The BUU model is typically solved via the test-particle method[22, 28], in which the nucleon phase space distribution is projected onto a collection of point particles. The nucleon dynamics are then realized by the correspondence between the nucleons and the test particles. The test-particle solution for the BUU equation has in the past shown success in describing observables derived from heavy ion collisions in the energy range of a few hundred MeV to about 2 GeV per nucleon[22]. However, the test-particle method can do a poor job at conserving energy, and for low energy collisions, this presents potentially important technical problems. In particular, for momentum-dependent mean field potentials, the energy non-conservation can be

quite drastic[29].

The lattice Hamiltonian algorithm[30] is a generalization of the test-particle method that has provided for solutions of the BUU equation which exhibit excellent energy conservation. This method has in the past been implemented for a *momentum-independent* nuclear mean field potential[30]. However, due to its numerical complexity, a lattice Hamiltonian algorithm for *momentum-dependent* nuclear mean field potentials has in the past not surfaced. In this work, we extend, for the first time, the lattice Hamiltonian algorithm to incorporate momentum-dependent potentials[3] and apply the model thus realized to the study of low to intermediate energy heavy ion collisions.

Before we move on, it is instructive to consider some typical observables for heavy ion collisions as the validity of our model will be based on its ability to reproduce experimentally measured signals. We first consider a form of large scale collective motion, which is denoted by "flow" (for example, see [32]). In the course of a heavy ion collision, one of the main characteristics observed from experiments is the evidence of large scale collective motion indicative of fluid-like behaviour. An example of collective motion can be visualized by considering the compression of a sealed balloon along one axis. In this case, the balloon expands along the free axes, that is the axes where there is no compression. This expansion/compression is an example of a collective effect. Collisions of heavy nuclei also can display this behaviour. The head-on collision of two nuclei for example will produce a similar effect. For collisions with a non-zero impact parameter (c.f. figure 5.1) however, the direction of expansion is no longer symmetric about the reaction plane. As the spectator matter is predominantly in the reaction plane, early expansion in the latter is hindered and expansion is generally favoured out of the reaction plane. This asymmetry in the expansion pattern is known as *elliptic flow*[33]. We discuss the elliptic flow in more detail in chapter 6. In addition to the elliptic flow, colliding nuclei

[3]After our work was completed, we became aware of a parallel realization of this model [31].

can exhibit both attractive and repulsive flow. To imagine this, consider two nuclei on a collision path with a non-zero impact parameter. As the nuclei collide, several mechanisms can take place. For instance, the nuclei can "bounce off" one another, thus being deflected off their original paths, attaining momenta transverse to the beam direction. As they (the nuclei) still carry some of their forward momentum, the net effect is a flow of nucleons away from the interaction region. This is the commonly used "text-book" picture used to describe the scattering of two particles and is shown schematically in figure 5.1. This is an an example of repulsive *directed* flow. In addition to this repulsive behaviour, at low energies the attractive part of the nuclear mean field can dominate. Thus, instead of the nuclei being deflected away from one another, they temporarily exist in a bound meta-stable state and partially orbit as they pass by one another. Eventually, the nuclei release. This is a case of *attractive* directed flow. Both of these two flow mechanisms are also known as directed *in-plane* flow: that is to say most of the dynamics takes place in the reaction plane. In this work, we investigate the elliptic flow at intermediate energies, and show that this observable serves to distinguish the functional character of the nuclear mean field. It can also serve to characterize the *in-medium* nucleon-nucleon collision cross section. The study of directed flow has also served to characterize these two features of nuclear matter. We also perform a study of directed flow at low energies.

Another observable often studied in heavy ion collisions is the *linear momentum transfer*[34, 35, 36]. This observable mainly concerns itself with the opacity (or inversely, the transparency) of nuclear matter. This quantity essentially characterizes the ability of nuclear matter to absorb momenta and as such can be useful in extracting the in-medium nucleon-nucleon cross section. In addition, the momentum-dependence may also play a role in the linear momentum transfer. We will perform a study of this behaviour in a forthcoming chapter.

The remainder of this work is organized as follows. Chapter 2 introduces the

many-body nuclear problem and presents us with a transport equation to be utilized for a dynamical description of nuclear matter. Namely, the BUU equation. Chapter 3 presents us with the ingredients necessary for obtaining a solution of the BUU transport equation, that is, the mean field potential and nucleon-nucleon collision cross section. The bulk of these first two chapters serves to provide the theoretical background material necessary for further development of the model presented here. Chapter 3 concludes by introducing the in-medium nucleon-nucleon cross section we have adopted that is specific to momentum-dependent nuclear mean field potentials. In chapter 4, we show how we adapt the nuclear matter idealization to finite nuclei. In addition, this chapter presents the momentum-dependent Lattice Hamiltonian (numerical) solution we have chosen in this work. Furthermore we address some of the performance issues present in the numerical solution in terms of energy and momentum conservation. We also examine *qualitative* features of the model as applied to collisions of heavy ions. Once our model has been developed, we go on to test its validity in terms of comparison with experimentally measured signals. In chapter 5 we examine both directed flow and linear momentum transfer in the energy regime of $E_k/A \sim 20 \rightarrow 150$ MeV and test the predictive power of our model against recent experimental measurements[37]. In chapter 6 we perform an investigation of elliptic flow in the energy regime of $E_k/A \sim 200 \rightarrow 1000$ MeV and compare with some recently measured elliptic flow signals[38].

Chapter 2

The TDHF and BUU equations

In this chapter, we introduce the basic tools required for a transport description of heavy ion collisions. We first show what our input wave function should look like along with the corresponding operators required to extract observables. Then, we present the time-dependent Hartree-Fock equation (TDHF) as a *mean field* approximation to this many-body system with a non-zero interaction potential. We also extend the TDHF equation to a semi-classical regime which is governed by the Vlasov equation. Finally, we write an extension of the Vlasov equation which attempts to re-incorporate inter-particle correlations that have been integrated out via the mean field. This extension is referred to as the Boltzmann-Uehling-Uhlenbeck (BUU) equation.

2.1 Basic Ingredients

2.1.1 Many-Body Wave Function

One of the main goals in describing transport phenomena in heavy ion collisions is to describe the time evolution of a large system of nucleons subject to some physical constraints such as conservation laws and the reproduction of bulk nuclear properties. The quantum nature of such a system demands that it be describable in terms of a

wave function whose evolution is given by the time-dependent Schrödinger equation (TDSE):

$$i\hbar\frac{\partial}{\partial t}\Psi(\vec{r},t) = \hat{\mathcal{H}}\Psi(\vec{r},t). \tag{2.1}$$

Here, $\hat{\mathcal{H}}$ is the Hamiltonian operator and $\Psi(\vec{r},t)$ is the wave function of the many-body system. As the wave function contains information about all particles in our system and their mutual interactions, solutions of (2.1) are in general difficult if not impossible to construct. We thus have to abandon solving (2.1) from a first-principles approach and adopt phenomenological methods. To aid us here, we adopt the *Hartree-Fock* approximation[23, 24, 25]. In this picture, it is assumed that the total wave function can be separated into independent particle wave functions. Furthermore, since this total wave function represents a collection of spin 1/2 nucleons, it must obey Fermi statistics, and thus exhibit the proper anti-symmetrized behaviour[1]. The Slater determinant provides the means with which we can construct our wave function[39]. In the following, we mean $o_\alpha(q_i)$ to be a single-particle wave function characterized by generalized coordinate q_i with quantum numbers α. The totally anti-symmetric many-body wave function for a system of A fermions reads:

$$\begin{aligned}\Psi(q_1, q_2, \cdots, q_a) &= \frac{1}{\sqrt{A!}}\begin{vmatrix} o_\alpha(q_1) & o_\beta(q_1) & \cdots & o_\omega(q_1) \\ o_\alpha(q_2) & o_\beta(q_2) & \cdots & o_\omega(q_2) \\ \vdots & \vdots & \ddots & \vdots \\ o_\alpha(q_A) & o_\beta(q_A) & \cdots & o_\omega(q_A) \end{vmatrix} \\ &= \frac{1}{\sqrt{A!}}\sum_p (\pm 1)^p \mathcal{P}(o_\alpha(q_1)o_\beta(q_2)\cdots o_\omega(q_A)),\end{aligned} \tag{2.2}$$

where $\mathcal{P}$ is the permutation operator and we must sum over all permutations. The factor of $(\pm 1)^p$ in the last step forces Ψ to be totally antisymmetric and is equal

[1]The original Hartree approximation used a simple product of wave functions, thus neglecting the fermionic nature for half-integer spin particles present in this theory. The anti-symmetrized version of the *Hartree* approximation is known as the *Hartree-Fock* approximation.

to (-)+1 for (odd) even permutations. The time-dependence in the above wave function(s) from here-on is assumed.

2.1.2 Kinetic and Potential energy operators

In the previous section, we introduced one of the ingredients necessary for describing our many-body system, namely, the wave function. From equation (2.1) we will also need the specific form of our Hamiltonian operator. We will work in second quantization[40]. In this notation, the Fermion creation and annihilation operators satisfy the anti-commutation relations:

$$\begin{aligned} \{a_\alpha, a_\beta^\dagger\} &= \delta_{\alpha\beta} \\ \{a_\alpha, a_\beta\} &= 0 \\ \{a_\alpha^\dagger, a_\beta^\dagger\} &= 0. \end{aligned} \tag{2.3}$$

where $\{a_\alpha, a_\beta\}$ means $a_\alpha a_\beta + a_\beta a_\alpha$ and the Greek letters specify any complete basis. The total kinetic energy operator, which is a one-body operator reads:

$$\begin{aligned} \hat{T} &= \sum_{\alpha\beta} <\alpha|\hat{t}|\beta> a_\alpha^\dagger a_\beta \\ &= \sum_{\alpha\beta} t_{\alpha\beta} a_\alpha^\dagger a_\beta. \end{aligned} \tag{2.4}$$

For the potential energy operator, we must consider two or more single-particle state functions, as this operator speaks in terms of interactions. In other words, the potential energy operator $\hat{v}$ operates between two (in general, this can be extended to many) single-particle states[2]. In second quantized notation, for the two-body potential energy operator, we have:

$$\begin{aligned} \hat{V} &= \frac{1}{2} \sum_{\alpha\beta\gamma\delta} <\alpha\beta|\hat{v}|\gamma\delta> a_\alpha^\dagger a_\beta^\dagger a_\delta a_\gamma \\ &= \frac{1}{2} \sum_{\alpha\beta\gamma\delta} v_{\alpha\beta\gamma\delta}\, a_\alpha^\dagger a_\beta^\dagger a_\delta a_\gamma. \end{aligned} \tag{2.5}$$

[2]In the interest of simplicity, we consider for now two-body potentials only.

We now have our kinetic and potential energy operators as well as our many-body wave function. This puts us in a position to calculate the energy expectation values.

2.1.3 Expectation Values

The measurable elements of a quantum mechanical system are the expectation values of the system. They are probabilistic quantities which represent the average value (of a particular observable) that we would expect by performing the same measurement on a system many times. In the language of quantum mechanics, expectation values can be shown to be the product of the wave function probability density times the eigenvalue we wish to measure integrated over all possibilities, where the total probability is normalized to one. We wish to find the expectation values for the operators discussed in the previous section. The total kinetic energy expectation value is

$$\begin{aligned} <T> &= <\Psi|\hat{T}|\Psi> \\ &= \sum_{\alpha\beta} t_{\alpha\beta} <\Psi|a^{\dagger}_{\alpha}a_{\beta}|\Psi> \\ &= \sum_{\alpha\beta} t_{\alpha\beta}\rho_{\beta\alpha}. \end{aligned} \tag{2.6}$$

In the above, the *one-body density matrix* is identified as $\rho_{\alpha\beta} =< \Psi|a^{\dagger}_{\beta}a_{\alpha}|\Psi >$ and plays the role of the quantum analogue of the classical phase space density. For a detailed discussion on the one-body density matrix, the reader is referred to [41].

For the potential energy expectation value we write using (2.5)

$$\begin{aligned} <V> &= <\Psi|\hat{V}|\Psi> \\ &= \frac{1}{2}\sum_{\alpha\beta\gamma\delta} v_{\alpha\beta\gamma\delta} <\Psi|a^{\dagger}_{\alpha}a^{\dagger}_{\beta}a_{\delta}a_{\gamma}|\Psi> . \end{aligned} \tag{2.7}$$

Notice that it appears as though we do not have a one-body density analogous to the kinetic energy case. In this expression, we have a *two-body* density matrix. However, since our total state function $|\Psi>$ is written as a Slater determinant, the two-body

density matrix is factorizable as one-body density matrices as shown in the appendix A.1. The result for the potential energy expectation value is shown below,

$$<V> = \frac{1}{2}\sum_{\alpha\beta\gamma\delta} v_{\alpha\beta\gamma\delta}\left(\rho_{\gamma\alpha}\rho_{\delta\beta} - \rho_{\delta\alpha}\rho_{\gamma\beta}\right). \tag{2.8}$$

We see from equations (2.6) and (2.8) that we can specify the total energy of our system completely in terms of the one-body density matrix. This is not an accident, but is a direct consequence of the total wave function, which *is* a Slater determinant. As previously mentioned, by assuming that we could specify the many-body system with a collection of single-particle wave functions, we have adopted a *mean field* approach. This approach allows one to treat any particle interactions as an average or mean arising from all the particles in the system. We will exploit the ability of the one-body density matrix to totally describe the system to gain insight into the dynamics of the many-body problem.

2.2 The TDHF equation

Starting from the one-body density matrix

$$\rho_{\alpha\beta} = <\Psi|a_\beta^\dagger a_\alpha|\Psi>. \tag{2.9}$$

we write the time derivative as:

$$\dot{\rho}_{\alpha\beta} = \left(\frac{\partial}{\partial t}<\Psi|\right)a_\beta^\dagger a_\alpha|\Psi> + <\Psi|a_\beta^\dagger a_\alpha\left(\frac{\partial}{\partial t}|\Psi>\right)$$

The terms in the brackets can be taken directly from the (state space representation) time-dependent Schrödinger equation, where in this picture, all dynamical information is contained in the wave function and the operators are time-independent. Insertion of equation (2.1) and its complex conjugate into the above along with the use of the Jacobi identity $[A, BC] = [A, B]C + B[A, C]$ gives the following result:

$$\dot{\rho}_{\alpha\beta} = \frac{1}{i\hbar}<\Psi|[a_\beta^\dagger, \hat{\mathcal{H}}]a_\alpha + a_\beta^\dagger[a_\alpha, \hat{\mathcal{H}}]|\Psi> . \tag{2.10}$$

In the above result, $\hat{\mathcal{H}} = \hat{T} + \hat{V}$ where the kinetic and potential energy operators are given by equations (2.4) and (2.5) respectively. The right hand side of equation (2.10) can be recast in terms of the one-body density matrix and single-particle kinetic and potential energy operators by use of the fermion creation and annihilation anti-commutation relations already introduced and by the single-particle potential energy operator[3] which we now introduce as:

$$u_{\alpha\beta} = <\alpha|\hat{u}|\beta> = \sum_{\mu\nu}(v_{\alpha\mu\beta\nu} - v_{\alpha\mu\nu\beta})\rho_{\nu\mu}. \tag{2.11}$$

With the single-particle Hamiltonian (operator) $\hat{h} = \hat{t} + \hat{u}$ where $\hat{t}$ and $\hat{u}$ are the single-particle kinetic and potential energy operators respectively, and following appendix A.2, the time derivative of the one-body density matrix now reads:

$$\dot{\rho}_{\alpha\beta} = \frac{1}{i\hbar}\sum_{\mu}\left(<\alpha|\hat{h}|\mu>\rho_{\mu\beta} - \rho_{\alpha\mu}<\mu|\hat{h}|\beta>\right). \tag{2.12}$$

We see that both $\hat{t}$ and $\hat{u}$ from above act as one-body operators. The fact that the potential operator is written as a sum over basis states and the *two-particle* potential energy operator evaluated over all pairs of states reflects the mean field nature already discussed. Equation (2.12) is the *time-dependent* Hartree-Fock (TDHF) equation for the one-body density matrix. This is a purely quantum mechanical result which uses a mean field to characterize the total potential energy in the system. It is a non-linear self-consistent[4] equation used in the context of many-electron atoms[42]. It has also been used in the past in the study of electron plasmas[25] and heavy ion physics [16, 22, 43]. For an alternate derivation of the TDHF equation using the Ritz variational procedure, the reader is referred to the references [25, 44, 45].

Before we go on, we mention that the total energy of our system is obtained from the expectation value of the total Hamiltonian, that is, $E = <\mathcal{H}> = <T> + <V>$.

[3]This is the so-called *Hartree-Fock* potential energy operator.

[4]This can be seen most easily by considering the close connection that equations (2.12) and (2.1) share. In the TDSE, the potential energy expectation value is obtained once we have an eigenfunction of this operator. However, since the operator itself depends on this eigenfunction, we have a self-consistency requirement.

where the *total* kinetic and potential energy expectation values are from equations (2.6) and (2.8). We note the connection between the total energy of the system and the single-particle energies via the functional derivative:

$$\frac{\delta <\mathcal{H}>}{\delta \rho_{\beta\alpha}} = t_{\alpha\beta} + u_{\alpha\beta} \equiv h_{\alpha\beta}. \tag{2.13}$$

where and $u_{\alpha\beta}$ is the Hartree-Fock potential energy operator from equation (2.11). The $h_{\alpha\beta}$ is the single-particle Hamiltonian. Note that it is the $<\mathcal{H}>$ that gives the total energy in the system. The single-particle Hamiltonian h is the energy a particle would have in the presence of many other particles. It has been termed the "energy of removal" by Koopmans[46, 47, 48].

2.2.1 The Vlasov Equation

The previous section showed how we can describe the time evolution of a many-body system characterized by single-particle wave functions in terms of the one-body density matrix. We can expand on this result a little further to obtain another closely related transport equation. Recall that the TDHF equation (2.12) is written in terms of a general basis $|\alpha>$. If we make a basis transformation to a continuous basis $|\vec{\xi}>$ (where for example $|\vec{\xi}>$ can be the configuration space basis $|\vec{r}>$ or the momentum space basis $|\vec{p}>$), the TDHF equation then reads:

$$\dot{\rho}(\vec{\xi},\vec{\xi}') = \frac{1}{i\hbar}\int d^3\xi'' \left(h(\vec{\xi},\vec{\xi}'')\rho(\vec{\xi}'',\vec{\xi}') - \rho(\vec{\xi},\vec{\xi}'')h(\vec{\xi}'',\vec{\xi}')\right). \tag{2.14}$$

Now let us consider a Wigner integral transform of the continuous basis one-body density matrix. The two transforms below are equivalent.

$$\begin{aligned} f_w(\vec{r},\vec{p}) &= \frac{1}{(2\pi\hbar)^3}\int d^3s\, e^{+i\vec{s}\cdot\vec{r}/\hbar}\rho_{\vec{p}+\frac{\vec{s}}{2},\vec{p}-\frac{\vec{s}}{2}} \\ &= \frac{1}{(2\pi\hbar)^3}\int d^3s\, e^{-i\vec{p}\cdot\vec{s}/\hbar}\rho_{\vec{r}+\frac{\vec{s}}{2},\vec{r}-\frac{\vec{s}}{2}} \end{aligned} \tag{2.15}$$

In the above, we have introduced the compact notation $\rho_{\vec{r}\vec{r}'} = \rho(\vec{r},\vec{r}')$. Taking the time derivative of the Wigner integral transform and using equation (2.14), we

obtain the following two equations where we have used the first of (2.15) for the kinetic contribution and the second for the potential contribution.

$$\begin{aligned} \dot{f}_w^{kin}(\vec{r},\vec{p}) &= \frac{1}{i\hbar}\frac{1}{(2\pi\hbar)^3}\int\int d^3s\, d^3p'\, e^{+i\vec{s}\cdot\vec{r}/\hbar} \\ &\times \left(t_{\vec{p}+\vec{s}/2,\vec{p}'}\rho_{\vec{p}',\vec{p}-\vec{s}/2} - \rho_{\vec{p}+\vec{s}/2,\vec{p}'}t_{\vec{p}',\vec{p}-\vec{s}/2}\right) \\ \dot{f}_w^{pot}(\vec{r},\vec{p}) &= \frac{1}{i\hbar}\frac{1}{(2\pi\hbar)^3}\int\int d^3s\, d^3r'\, e^{-i\vec{p}\cdot\vec{s}/\hbar} \\ &\times \left(u_{\vec{r}+\vec{s}/2,\vec{r}'}\rho_{\vec{r}',\vec{r}-\vec{s}/2} - \rho_{\vec{r}-\vec{s}/2,\vec{r}'}u_{\vec{r}',\vec{r}-\vec{s}/2}\right) \end{aligned} \tag{2.16}$$

The matrix element for the kinetic term is:

$$t_{\vec{p}+\vec{s}/2,\vec{p}'} = \frac{\vec{p}'^{\,2}}{2m}\delta(\vec{p}+\vec{s}/2-\vec{p}').$$

For the potential term, if we assume that $\hat{u}$ is local, that is, $\hat{u}$ is a function of position only[5,6], then we can write the matrix element for the potential term as:

$$u_{\vec{r}-\vec{s}/2,\vec{r}'} = u(\vec{r}')\delta(\vec{r}+\vec{s}/2-\vec{r}'). \tag{2.17}$$

From here, the kinetic and potential terms are relatively straightforward to calculate. However, for the potential term, we must go through a bit of algebra (see appendix A.3) and use the single-particle mean field potential introduced in equation (2.17) to obtain:

$$\begin{aligned} \dot{f}_w^{kin}(\vec{r},\vec{p}) &= -\left(\frac{\vec{p}}{m}\cdot\nabla_{\vec{r}}\right) f_w(\vec{r},\vec{p}) \\ \dot{f}_w^{pot}(\vec{r},\vec{p}) &= \frac{2}{\hbar}\sin\left(\frac{\hbar}{2}\overleftarrow{\nabla}_{\vec{p}}\cdot\overrightarrow{\nabla}_{\vec{r}}\right) u(\vec{r}) f_w(\vec{r},\vec{p}). \end{aligned} \tag{2.18}$$

Now, we will make a semi-classical approximation that $\hbar$ is small, so that only the first term in the sin function above survives[7]. This approximation also requires $u(\vec{r})$,

[5] Note that we have already done this in writing equation (2.16).

[6] $\hat{u}$ is said to be diagonal in the coordinate space basis used here. In principle, it can also depend on momentum. In this case, the momentum-independent part of $\hat{u}$ is evaluated for fixed $\vec{p}$ as given on the left hand side of equation (2.16) in $\dot{f}_w^{pot}(\vec{r},\vec{p})$.

[7] Note that in this semi-classical approximation, we have only kept terms linear in $\hbar$ in the operators, the Wigner function however still contains $\hbar$ to all orders.

to be a slowly varying function of $\vec{r}$ (i.e. so that the high order derivatives are negligible). We now arrive at the Vlasov equation for the Wigner function $f_w(\vec{r},\vec{p})$.

$$\frac{\partial f_w(\vec{r},\vec{p})}{\partial t} + \frac{\vec{p}}{m}\cdot\nabla_{\vec{r}} f_w(\vec{r},\vec{p}) - \nabla_{\vec{r}}\, u(\vec{r})\cdot\nabla_{\vec{p}} f_w(\vec{r},\vec{p}) = 0 \tag{2.19}$$

Recall that we have assumed a single-particle potential that depends only on position. To generalize this to a potential which includes some momentum dependence, the following steps are taken. Split the potential into terms containing no momentum-dependence and the other terms containing momentum-dependence. For the latter, we follow the same procedure in evaluating the time derivative of the Wigner transform as was done for the kinetic term . With this, the $\vec{p}/m$ in equation (2.19) is replaced with $\nabla_{\vec{p}} h$, the momentum space gradient of the single-particle Hamiltonian h. The latter is written as

$$h(\vec{r},\vec{p}) = \frac{\vec{p}^{\,2}}{2m} + u(\vec{r},\vec{p}), \tag{2.20}$$

which in general contains both position and momentum-dependent terms in the single-particle potential. As there is no dependence upon position in the kinetic energy term, we can also replace the $\nabla_{\vec{r}}\, u(\vec{r})$ in equation (2.19) with $\nabla_{\vec{r}} h$. Note that equation (2.20) is the continuous basis representation of equation (2.13).

The Vlasov equation is essentially the TDHF equation in a semi-classical truncation scheme. Both equations imply the same self-consistency requirement. The essential difference is in the generating "function": density matrix in TDHF and Wigner function in Vlasov. Both the TDHF and Vlasov equations are time-dependent solutions to the many-fermion problem. The reader is referred to [49, 50] for a discussion of the Vlasov equation, and to [50, 51, 52] for a discussion of the TDHF equation.

The question arises as to why we introduced the Vlasov equation at all when we already had the TDHF equation. To answer this, we turn back to the Wigner transforms already introduced. Consider the following properties of f_w integrated separately over momentum and configuration space:

$$\int d^3p\, f_w(\vec{r},\vec{p}) \;=\; \frac{1}{(2\pi\hbar)^3}\int\int d^3p\, d^3s\, e^{-i\vec{p}\cdot\vec{s}/\hbar}\rho_{\vec{r}+\vec{s}/2,\vec{r}-\vec{s}/2}$$

$$\begin{aligned} &= \rho(\vec{r}) \\ \int d^3r f_w(\vec{r},\vec{p}) &= \frac{1}{(2\pi\hbar)^3}\int\int d^3r\, d^3s\, e^{+i\vec{s}\cdot\vec{r}/\hbar}\rho_{\vec{p}+\vec{s}/2,\vec{p}-\vec{s}/2} \\ &= g(\vec{p}) \end{aligned} \tag{2.21}$$

In the above, notice that $\rho(\vec{r})$ is the ordinary configuration space density, while $g(\vec{p})$ is the ordinary momentum space density. So, it is evident that the Wigner transform of the one-body density matrix behaves in some respects like a classical phase space density[8]. In short, the Wigner transform acts as a transition from quantum to classical mechanics. See [53, 54, 55, 56] for a discussion. With this correspondence between the Wigner function and the classical phase space density, the Vlasov equation is then written as a transport equation for $f(\vec{r},\vec{p})$, the *classical* phase space density.

2.3 The BUU equation

In the previous section, we introduced the semi-classical Vlasov equation which describes the time evolution of the *continuous* classical phase space density[9]. The Vlasov equation (2.19) tells us how the latter will deform over time due to both particle[10] momenta (the second term in the Vlasov equation, also known as the *streaming* term) and a force term (third term in the Vlasov equation). In the analysis up to now, we have neglected an additional term that can alter $f(\vec{r},\vec{p})$. Specifically, this term arises from hard[11] collisions between the discrete particles, each

[8]It is understood that the Wigner transform is not positive definite, whereas the classical phase space density is. It is assumed that this will not be problematic (see the supplied references for a discussion).

[9]Strictly speaking, $f(\vec{r},\vec{p})$ is built up from a collection of many discrete particles each with a well defined position and momentum.

[10]Particle here means a point in the classical phase space density.

[11]By *hard* collisions, we mean collisions processes higher than one-body processes. The interaction of the nucleons with the mean field is an example of the latter. In contrast, hard collisions can be

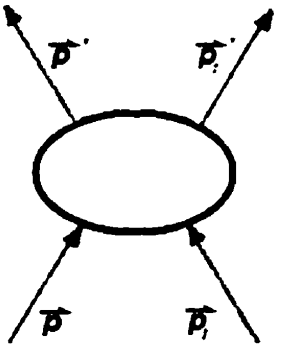

Figure 2.1: Two-particle scattering process taking the initial momentum states $\vec{p}$ and $\vec{p}_1$ to the final momentum states $\vec{p}'$ and $\vec{p}'_1$.

with well-defined phase space coordinates. We note that the adoption of the mean field (one-body term) has averaged out these interactions (two-body and higher processes). We consider our collisions to take place at the same point in configuration space (i.e. local collisions). In this work we are mainly concerned with low energy and density scenarios. For this reason, we consider only binary elastic collisions. In figure 2.1 we display such a scattering process. Consider a volume in phase space $\Omega = \delta^3 r \delta^3 p$, such that $\vec{p}$ resides inside this volume element. If these two particles scatter such that the final momenta of $\vec{p}$, namely $\vec{p}'$, lies outside Ω, then this represents a *loss term* to the phase space density $f(\vec{r}, \vec{p})$. The rate at which particles leak out of Ω will be proportional to the following quantities:

- the density of particles located at both $f(\vec{r}, \vec{p})$ and $f(\vec{r}, \vec{p}_1)$ that can undergo the scattering process in figure 2.1.
- the rate at which the scattering process in figure 2.1 takes place.
- the number of empty sites (phase space regions) in the final state, namely $(1 - \frac{h^3}{g} f(\vec{r}, \vec{p}'))$ and $(1 - \frac{h^3}{g} f(\vec{r}, \vec{p}'_1))$.

two (and-higher) nucleon scattering processes for example.

The last condition is a restatement of the Pauli exclusion principle which in this case states that the scattering process in figure 2.1 cannot take place if the final state phase space is already maximally populated. In the above, h^3 is the volume of a 6-dimensional phase space element and g is the nucleon spin/isospin degeneracy. Without providing here a formal derivation (c.f. [57, 58]), we show the loss term below:

$$\begin{aligned} \dot{f}^-(\vec{r},\vec{p}) &= \int d^3p_1\, d\Omega \left|\frac{\vec{p}}{m} - \frac{\vec{p}_1}{m}\right| \left(\frac{d\sigma(\vec{p}+\vec{p}_1 \to \vec{p}' + \vec{p}'_1)}{d\Omega}\right) \\ &\times f(\vec{r},\vec{p}) f(\vec{r},\vec{p}_1)(1 - \frac{h^3}{g} f(\vec{r},\vec{p}'))(1 - \frac{h^3}{g} f(\vec{r},\vec{p}'_1)). \end{aligned} \tag{2.22}$$

This result is easily understood: the first two terms in the integrand, the first two distribution functions and the last two terms in brackets are the scattering rate, the density of initial states and the number of empty final states respectively. There is also a corresponding *gain term*, which will account for the inverse of the collision depicted in figure 2.1. In this case, the scattering process scatters a particle that was originally outside Ω into this volume element. This gain term reads:

$$\begin{aligned} \dot{f}^-(\vec{r},\vec{p}) &= \int d^3p_1\, d\Omega \left|\frac{\vec{p}'}{m} - \frac{\vec{p}'_1}{m}\right| \left(\frac{d\sigma(\vec{p}'+\vec{p}'_1 \to \vec{p}+\vec{p}_1)}{d\Omega}\right) \\ &\times f(\vec{r},\vec{p}') f(\vec{r},\vec{p}'_1)(1 - \frac{h^3}{g} f(\vec{r},\vec{p}))(1 - \frac{h^3}{g} f(\vec{r},\vec{p}_1)). \end{aligned} \tag{2.23}$$

These loss and gain terms replace the zero on the right hand side of the Vlasov equation (2.19). This new equation then reads:

$$\begin{aligned} &\frac{\partial f(\vec{r},\vec{p})}{\partial t} + \nabla_{\vec{p}} h \cdot \nabla_{\vec{r}} f(\vec{r},\vec{p}) - \nabla_{\vec{r}} h \cdot \nabla_{\vec{p}} f(\vec{r},\vec{p}) \\ &= \int d^3p_1\, d\Omega \left(v_{rel} \times \frac{d\sigma}{d\Omega}\right) \left(f f'_1 \bar{f} \bar{f}_1 - f f_1 \bar{f}' \bar{f}'_1\right), \end{aligned} \tag{2.24}$$

where

$$\begin{aligned} f_i &\equiv f(\vec{r},\vec{p}_i) \\ f'_i &\equiv f(\vec{r},\vec{p}'_i) \\ \bar{f}_i &\equiv 1 - \frac{h^3}{g} f(\vec{r},\vec{p}_i), \end{aligned}$$

and we have assumed that the inverse collision takes on the same differential cross section as the original collision. In addition, since we are dealing with elastic collisions only, the relative velocity terms in equations (2.22) and (2.23) are equal and are written as v_{rel} in equation (2.24). The new transport equation is the Vlasov equation supplemented with a (binary) collision integral that respects the symmetry properties of the particles that make up the phase space distribution function. The study of this equation was first initiated by Nordheim[59] and implemented by Uehling and Uhlenbeck [60, 61] in the context of electron plasmas. Equation (2.24) is known as the BUU (Boltzmann-Uehling-Uhlenbeck) equation[12]. As we have written it, the BUU equation describes the rate of change of the phase space density due to both mean field and binary elastic collision effects. For further reference, we note that an attempt to include collision effects in the TDHF equation has been made by Wong[62, 63].

As it stands, the BUU equation now requires inputs via the single-particle potential (which includes the mean field) and the differential binary collision cross section. This is the subject of the following chapter.

[12]It is also known in the literature as the Boltzmann-Nordheim-Vlasov (BNV) equation and the Vlasov-Nordheim equation.

Chapter 3

BUU model inputs

This chapter serves to present us with the mean field potentials and binary differential scattering cross section that will be incorporated into our many-body nuclear system. In the previous chapter, we recall that the transport equation we have chosen is the BUU equation with its associated mean field (Hartree-Fock) single-particle potential. We have not however presented a detailed analysis that gives us the functional form of the latter. In this chapter, we will further investigate the Hartree-Fock approximation introduced thus far and present some mean fields suitable for a description of nuclear matter. Comparisons with recent microscopic calculations of the many-body nuclear potential and equations of state will be addressed. Finally, we will re-address the nucleon-nucleon cross section presented in section 2.3 as the former requires some modification dependent on the choice of nuclear mean field.

3.1 The Hartree-Fock Potential

Recall from section 2.2, we had introduced the Hartree-Fock potential so that we could write the single-particle Hamiltonian as a sum of two one-body operators (see equations (2.4) and (2.11)). Namely, the kinetic and potential terms. There are some consequences associated with this that have yet to be expanded upon. To see

this, we consider equation (2.14), and write the configuration space one-body density matrix as:

$$\begin{aligned}\rho(\vec{r},\vec{r}') &= <\Psi|a^{\dagger}(\vec{r}')a(\vec{r})|\Psi> \\ &= \sum_{ij} o_i^*(\vec{r}')o_j(\vec{r}) <\Psi|a_i^{\dagger}a_j|\Psi> \\ &= \sum_{i} o_i^*(\vec{r}')o_i(\vec{r}). \end{aligned} \tag{3.1}$$

where we have performed an expansion in the single-particle wave functions $o_i(\vec{r})$. Inserting this and its time derivative into the configuration space basis representation of the TDHF equation, we arrive at the TDHF equation for the single-particle wave function.

$$\begin{aligned} i\hbar\frac{\partial}{\partial t}o_i(\vec{r}) &= \left(-\frac{\hbar^2}{2m}\nabla_{\vec{r}}^2 + \int d^3r'\, v(\vec{r},\vec{r}')\rho(\vec{r}')\right) o_i(\vec{r}) \\ &- \int d^3r'\, v(\vec{r},\vec{r}')o_i(\vec{r}')\sum_j o_j^*(\vec{r}')o_j(\vec{r}). \end{aligned} \tag{3.2}$$

The above result is realized by considering the orthogonality of the single particle wave-functions after insertion of the continuous one-body density matrix in equation (3.1). In equation (3.2), v is the configuration space analogue of the potential energy operator in equation (2.5). The first term in brackets in equation (3.2) is the kinetic energy operator, the second term is known as the *direct* or Hartree term, and arises as a result of adopting the *mean field*. The third term is the *exchange* or Fock term. It represents a non-local contribution to the total potential energy operator and is a consequence of the fermion anti-commutation relations as well as the aforementioned mean field approximation. In general, the two-body potential energy operator v is non-trivial and contains many contributions to the nucleon-nucleon interaction. These contributions manifest themselves in terms of boson exchange forces and thus contain spin and isospin dependencies which have been absorbed into the i and j indices in equation (3.2). As a calculation of this magnitude is beyond the scope of this work, we adopt an illustrative picture and judge its merits *a posteriori*. Details regarding the nucleon-nucleon potential energy operator can be found in [64, 65].

In the foregoing analysis, we suppress any spin and isospin dependence and treat the v as a phenomenological potential. We will adopt the one-boson exchange model in which the two-body interaction potential arises from the exchange of a massive virtual boson. As the lifetime of this exchange particle is governed by the Heisenberg uncertainty principle, it necessarily has an effective range (the strong force is short range). Adoption of this picture thus leads to the Yukawa potential (see [64, 66] for example). The two-body interaction potential thus reads:

$$v(\vec{r},\vec{r}') = -V_0 \frac{e^{-\Lambda|\vec{r}-\vec{r}'|}}{\Lambda|\vec{r}-\vec{r}'|}. \tag{3.3}$$

where V_0 measures the strength of the two-body interaction potential and Λ is a measure of the interaction range. To evaluate the integral for the direct term in equation (3.2) with (3.3), we remind the reader that we are working in the nuclear matter approximation in which the density is constant over all space. We thus arrive at the following single-particle potential for the direct term:

$$u^{(D)}(\vec{r}) = \int d^3r'\, v(\vec{r},\vec{r}')\rho(\vec{r}') = A\frac{\rho(\vec{r})}{\rho_0}. \tag{3.4}$$

where the factor of $A = 4\pi V_0 \rho_0/\Lambda^3$ has absorbed all integration constants.

Before tackling the exchange potential, we first note that as we are attempting to reproduce bulk nuclear properties, the total energy (which is negative for a bound system such as the one we have here) in the system given by equations (2.13) and (2.20) must possess a minimum. For the *density-dependent* single-particle potential presented above, this saturation condition clearly cannot be satisfied, as the *total* potential energy corresponding to equation (3.4) is linear in ρ (c.f. equation (2.13)) and the total kinetic energy[1] goes as $\rho^{2/3}$ and is a positive quantity. As we show below however, we can meet this condition if we consider in addition to the two-body interaction potential[2], a three-body interaction potential. We adopt a purely

[1] This is proportional to the Fermi kinetic energy.

[2] Recall in section 2.1.2 that the choice of a two-body interaction potential only was chosen in the interest of simplicity.

phenomenological approach and use a three-body contact interaction. With this, we get an additional term to be added to the single-particle potential, namely,

$$\begin{aligned} u^{(D)}(\vec{r}) &= \int d^3r'\, d^3r''\, v(\vec{r}, \vec{r}', \vec{r}'')\rho(\vec{r}')\rho(\vec{r}'') \\ &= \int d^3r'\, d^3r''\, \frac{B'}{\rho_0^2}\delta(\vec{r}-\vec{r}')\delta(\vec{r}'-\vec{r}'')\rho(\vec{r}')\rho(\vec{r}'') \\ &= B'\left(\frac{\rho(\vec{r})}{\rho_0}\right)^2. \end{aligned}$$

We then write the total direct term as a sum of the two-body and three-body interaction terms to get a term linear in the density and a term quadratic in the density. Note that continuing in this manner we will have terms that are the n^{th} power of density for an $(n+1)$-body interaction. However, it is customary to generalize the two- and three-body result to an n-body result by setting the power of ρ in the three-body result to a variable parameter (which we will later fix to bulk nuclear properties). This generalization leads to

$$u^{(D)}(\vec{r}) = A\left(\frac{\rho(\vec{r})}{\rho_0}\right) + B\left(\frac{\rho(\vec{r})}{\rho_0}\right)^{\sigma}. \tag{3.5}$$

As the constants appearing in the above equation can differ in sign, we can then achieve a minimum in the total energy, that is, saturation. In fact this is a condition used to fix the value of one of the parameters introduced thus far. The density-dependent single-particle potential in equation (3.5) has been utilized extensively in the past and has been referred to as the Skyrme or Zamick interaction[21, 67, 68, 69]. In the past, it was derived by using a contact interaction for both the two-body term as well as the generalized three-body term. We will adopt this density-dependent single-particle potential from here-on.

Next we turn to the exchange term. It is instructive to consider the properties of the system which we seek to describe. As previously mentioned, we are working in the *nuclear matter* approximation. In this case, the system is uniform and of infinite extent (see footnote on page 1) with definite momenta ascribed to each nucleon. Thus, the single-particle wave functions are plane waves. Suppressing spin

and isospin dependence (the indices i and j below now label momentum states), the exchange term thus reads:

$$\begin{aligned} I_{exchange} &\propto -\sum_j \int d^3r'\, v(\vec{r},\vec{r}')e^{-i\vec{k}_j\cdot\vec{r}'}e^{+i\vec{k}_j\cdot\vec{r}}e^{+i\vec{k}_i\cdot\vec{r}'} \times \left(e^{-i\vec{k}_i\cdot\vec{r}}e^{+i\vec{k}_i\cdot\vec{r}}\right) \\ &= -\left(\sum_j \int d^3r'\, v(\vec{r},\vec{r}')e^{+i(\vec{k}_i-\vec{k}_j)\cdot(\vec{r}'-\vec{r})}\right)\phi_i(\vec{r}) \\ \Longrightarrow I_{exchange} &\propto u_i^{(E)}(\vec{r})\phi_i(\vec{r}). \end{aligned}$$

We note in this case, the single-particle potential for the exchange term is a Fourier transform of the two-body interaction potential and thus in general is momentum-dependent. That is, the non-local exchange term is reflected in a momentum-dependent single-particle potential. For the two-body interaction potential, we again use the Yukawa interaction from equation (3.3). With this, the single-particle potential for the exchange term reads:

$$\begin{aligned} u^{(E)}(\vec{r},\vec{k}) &= -\sum_j \int d^3r' \left(-V_0'\frac{e^{-\Lambda'|\vec{r}-\vec{r}'|}}{\Lambda'|\vec{r}-\vec{r}'|}\right)e^{+i(\vec{k}-\vec{k}_j)\cdot(\vec{r}'-\vec{r})} \\ &= \frac{4\pi V_0'}{\Lambda'^3}\sum_j \frac{1}{1+\left(\frac{\vec{k}-\vec{k}_j}{\Lambda'}\right)^2}. \end{aligned} \tag{3.6}$$

From section 2.2.1 outlining the transition to a continuous transport equation (i.e. the Vlasov equation for the continuous classical phase space density) and equations (3.5) and (3.6), we can then write the continuous total single-particle potential as

$$u(\vec{r},\vec{p}) = A\left(\frac{\rho(\vec{r})}{\rho_0}\right) + B\left(\frac{\rho(\vec{r})}{\rho_0}\right)^\sigma + \frac{2C}{\rho_0}\int d^3p' \frac{f(\vec{r},\vec{p}')}{1+\left(\frac{\vec{p}-\vec{p}'}{\Lambda}\right)^2}, \tag{3.7}$$

which contains both density and momentum-dependent terms. The constant C in the above has been chosen for convenience. Here, the $u(\vec{r},\vec{p})$ corresponds to that in equation (2.20). From the short discussion at the end of section 2.2, we mentioned that the total energy of the system must be obtained from the total Hamiltonian, and not the single-particle Hamiltonian. As we will need the total energy, we must be able to write down a potential energy (density) that corresponds to the above

single-particle potential. With the distribution function $f(\vec{r},\vec{p})$, we can relate the single-particle potential to the total potential energy density[3]:

$$u(\vec{r},\vec{p}) = \frac{\delta V(\vec{r})}{\delta f(\vec{r},\vec{p})}. \tag{3.8}$$

The corresponding potential energy density thus reads:

$$V(\vec{r}) = \frac{A}{2}\frac{\rho(\vec{r})^2}{\rho_0} + \frac{B}{\sigma-1}\frac{\rho(\vec{r})^{\sigma+1}}{\rho_0^{\sigma}} + \frac{C}{\rho_0}\int d^3p\, d^3p' \frac{f(\vec{r},\vec{p})f(\vec{r},\vec{p}')}{1+\left(\frac{\vec{p}-\vec{p}'}{\Lambda}\right)^2}. \tag{3.9}$$

The five coefficients A, B, σ, C and Λ in equations (3.7) and (3.9) are to be determined from observed properties of heavy nuclei (as an approximation to nuclear matter[70]). Equations (3.7) and (3.9) are known as the MDYI-potential (Momentum-Dependent Yukawa Interaction) and have been previously investigated in simulations of heavy ion collisions[71, 72, 73]. The use of the MDYI potential in numerical simulations of heavy ion collisions places heavy constraints on the assumed numerical algorithm as solving equation (3.7) can be very time-consuming. As such, Gale et al. [74] introduced an approximation to equation (3.7) by replacing the $\vec{p}'$ in the denominator of the integrand in the third term of equation (3.9) by it local average. This approximation reads:

$$\int d^3p' \frac{f(\vec{r},\vec{p}')}{1+\left(\frac{\vec{p}-\vec{p}'}{\Lambda}\right)^2} \cong \frac{1}{1+\left(\frac{\vec{p}-<\vec{p}(\vec{r})>}{\Lambda}\right)^2}\int d^3p'\, f(\vec{r},\vec{p}') = \frac{\rho(\vec{r})}{1+\left(\frac{\vec{p}-<\vec{p}(\vec{r})>}{\Lambda}\right)^2}$$

where

$$<\vec{p}(\vec{r})> = \frac{\int d^3p'\,\vec{p}'\, f(\vec{r},\vec{p}')}{\int d^3p'\, f(\vec{r},\vec{p}')}.$$

Substituting this into the MDYI potential energy density in equation (3.9), and using equation (3.8), we arrive at the following expressions for the potential energy density and single-particle potential at equilibrium:

$$V(\vec{r}) = \frac{A}{2}\frac{\rho(\vec{r})^2}{\rho_0} + \frac{B}{\sigma+1}\frac{\rho(\vec{r})^{\sigma+1}}{\rho_0^{\sigma}} + \frac{C\rho(\vec{r})}{\rho_0}\int d^3p' \frac{f(\vec{r},\vec{p}')}{1+\left(\frac{\vec{p}'-<\vec{p}>}{\Lambda}\right)^2}, \tag{3.10}$$

[3]The reader may wish to notice the connection with equation (2.13)

$$u(\vec{r},\vec{p}) = A\left(\frac{\rho(\vec{r})}{\rho_0}\right) + B\left(\frac{\rho(\vec{r})}{\rho_0}\right)^{\sigma} + \frac{C}{\rho_0}\int d^3p' \frac{f(\vec{r},\vec{p}')}{1+\left(\frac{\vec{p}'-<\vec{p}>}{\Lambda}\right)^2} + \frac{C\rho(\vec{r})}{\rho_0}\frac{1}{1+\left(\frac{\vec{p}-<\vec{p}>}{\Lambda}\right)^2}, \quad (3.11)$$

where it is understood that $<\vec{p}>=<\vec{p}(\vec{r})>$. Equations (3.10) and (3.11) are known as the GBD-potential (Gale-Bertsch-Das Gupta) and have also been investigated in the simulations of heavy ion collisions[74, 75, 76]. In this work, we will from here-on be concerned with the Skyrme (density-dependent) interaction given by equation (3.5) as well as both the MDYI-type and GBD-type realizations of the momentum-dependent mean field given by equations (3.7) and (3.11) respectively. These are the input single-particle potentials that are coupled to the kinetic energy to give the single particle Hamiltonian h given in equation (2.20). That is, we separately use these three parameterizations of the nuclear mean field potential in order to perform simulations of colliding heavy ions. We stress however, that the momentum-dependent potentials are far superior to the momentum-independent potentials as the former are more realistic. We address this point in the next section. Before leaving this section, note that other functional forms for momentum-dependence have been used in the past in [77] and [78].

3.1.1 Mean Field parameterizations

Thus far, we have shown from a phenomenological point of view some functional forms of the single-particle potential that arise from adopting the Hartree-Fock approximation. The momentum-dependent term arose naturally as a consequence of the exchange term. It is also known from nucleon-nucleus scattering experiments that the real part of the single-particle (optical) potential is strongly momentum-dependent[26, 79]. We can use this experimental information to help constrain the parameters introduced in the GBD and MDYI-type potentials. As the Skyrme interaction is not momentum-dependent, the coefficients can be constrained without knowledge of the momentum-dependence of the optical potential. To begin, we en-

sure that the potentials we adopt can reproduce bulk properties of nuclear matter[70]. Namely, we require that the total energy per nucleon E/A in cold nuclear matter at saturation density ρ_0 is -16 MeV. A second criterion is that nuclear matter attain equilibrium at saturation density. This is equivalent to demanding that the pressure[4] $\mathcal{P}$ vanish at ρ_0 and $T = 0$ MeV. The last condition (zero temperature) holds for all cases as we constrain our system to match the properties of cold nuclear matter. We will examine the properties of hot nuclear matter shortly. The compressibility,[5] K, of nuclear matter can also serve to characterize our system (c.f. monopole breathing modes[70, 80]). Thus far, we have three conditions to satisfy and have specified enough information to determine the momentum-independent mean field parameterization which contains three parameters. For a more detailed description of the procedure, the reader is referred to [22]. Before we present the parameterizations, we first mention that the dependence on momentum in our GBD and MDYI potentials implies that the nucleons will have an effective mass[70] that is in general different from the free nucleon mass. The effective mass m^* is defined so that:

$$\frac{\vec{p}}{m^*} = \frac{\vec{p}}{m} + \nabla_{\vec{p}} u(\rho, \vec{p}). \tag{3.12}$$

where we have written the single-particle potential as:

$$u(\vec{r}, \vec{p}) = u(\rho(\vec{r}), \vec{p}) = u(\rho, \vec{p}).$$

We will use this notation interchangeably.

To fix the momentum-dependent potentials, we need to specify two additional parameters: C and Λ. For example, we can choose to fix two of $\{C, \Lambda, m^*/m, U(\rho, \vec{p})\}$. Table 3.1 shows all the potentials we will use in this work and some of the coefficients that define the potential. In this table, we have shown in bold face, the imposed conditions. For all potentials listed, $E/A = -16$ MeV and $d(E/A)/d\rho = 0$ at $\rho = \rho_0$.

[4]The zero temperature pressure is formally defined as $\mathcal{P} = \rho^2 \partial(E/A)/\partial\rho$.

[5]The compressibility coefficient is a measure of the change in volume of a system with respect to changes in pressure and is formally defined as $K = 9\partial\mathcal{P}/\partial\rho$.

Potential	σ	$\Lambda/p_f^{(0)}$	m^*/m	$U(\rho_0, p=0)$	$U(\rho_0, p=p_f^{(0)})$	$U(\rho_0, \infty)$	K	Ref.
S	1.167	-	1.00	-53.0	-53.0	-53.0	**200**	[22]
H	2.000	-	1.00	-53.5	-53.5	-53.5	**380**	[22]
GBD	**1.167**	**1.50**	**0.70**	-76.3	-53.3	-1.34	215	[74]
NGBD	**1.091**	1.88	**0.67**	-73.5	-51.4	**+30.5**	210	[81]
MDYI	1.240	1.58	0.67	**-75.0**	**0.0** (see caption)	+30.5	**215**	[71]
NMDYI	**1.091**	1.58	**0.67**	-72.4	-51.4	**+30.5**	210	[81]
HMDYI	2.270	1.58	**0.67**	-72.4	-51.4	**+30.5**	**373**	[81]

Table 3.1: Coefficients and properties of the single-particle potentials. For all mean fields presented above, the conditions $E/A = -16$ MeV and $d(E/A)/d\rho = 0$ at $\rho = \rho_0$ are satisfied. For the momentum-independent parameterizations (S and H), this leaves only one more condition to completely specify the mean field. This condition is the compressibility and is shown in bold-face type. For the momentum-dependent parameterizations (all others), we require three additional conditions, these are also shown in bold face type. For the MDYI potential (sixth row), the constraint (shown in the sixth column) was for $U(\rho_0, p^2/2m = 300$ MeV) and not $U(\rho_0, p = p_f^{(0)})$ as listed for all other potentials.

All conditions were applied to cold nuclear matter at saturation density ρ_0. The potentials labelled S and H are the momentum-independent Skyrme potential. The S (H) is meant to represent a choice of the parametrization that gives a soft (stiff) equation of state. For the momentum-dependent potentials, there is only one which results in a stiff EOS, this is the HMDYI potential presented in table 3.1.

In table 3.1 we note that for some potentials, the compressibility (K) was fixed. For the soft potentials (S,MDYI), the value of K here was motivated by monopole breathing modes[80] already mentioned and prompt supernovæ explosion mechanisms[82, 83], both of which favour a soft equation of state (low value of the nuclear compressibility). The stiff parametrizations are chosen to facilitate comparisons be-

tween mean fields of different compressibilities. The bottom four potentials listed in table 3.1 have specified a value of the single-particle potential to constrain the parametrization. This was done by close examination of the real part of the nuclear optical potential extracted from nucleon-nucleus scattering experiments. The mean field was then fixed at points which match the observed value of the former. In figure 3.1, we present a compilation of various experimental extractions of the single-particle potential (or real part of the optical potential[6]) up to energies ~1000 MeV/A obtained from nucleon-nucleus scattering experiments. We also show in this plot four of the momentum-dependent mean fields used in this work. As indicated by the figure, with the exception of the GBD (K = 215 MeV) potential (continuous shaded line), we have quite remarkable agreement with the data over the whole energy range presented. We see that with a suitable choice of parameters for the momentum-dependent mean fields used here, that excellent agreement with the observed optical potential is obtained.

For the comparison of our momentum-dependent interaction with the optical analysis from nucleon-nucleus scattering experiments, the mean fields were calculated at saturation density ρ_0, as for these experiments, the density is not expected to differ too much from this value. One can imagine however, that in the course of a collision of *two* heavy ions for instance, densities other than that of saturation will most likely play a role. It is thus valuable to understand the behaviour of the GBD and MDYI-type potentials away from saturation density, as we ultimately intend to apply our model to a study of heavy ion collisions. Since we are somewhat censored from directly examining this quantity in the lab, we will have to turn to more descriptive calculations of the nuclear mean field, where the density dependence is clearly evident. We present in figures 3.2 and 3.3 the single-particle potential as a function of momentum for densities ranging from sub-saturation to ~2.5 times

[6]We note that the construction of the real part of the optical potential from scattering data is model dependent however. These dependencies are somewhat reflected in the dispersion among the data points shown.

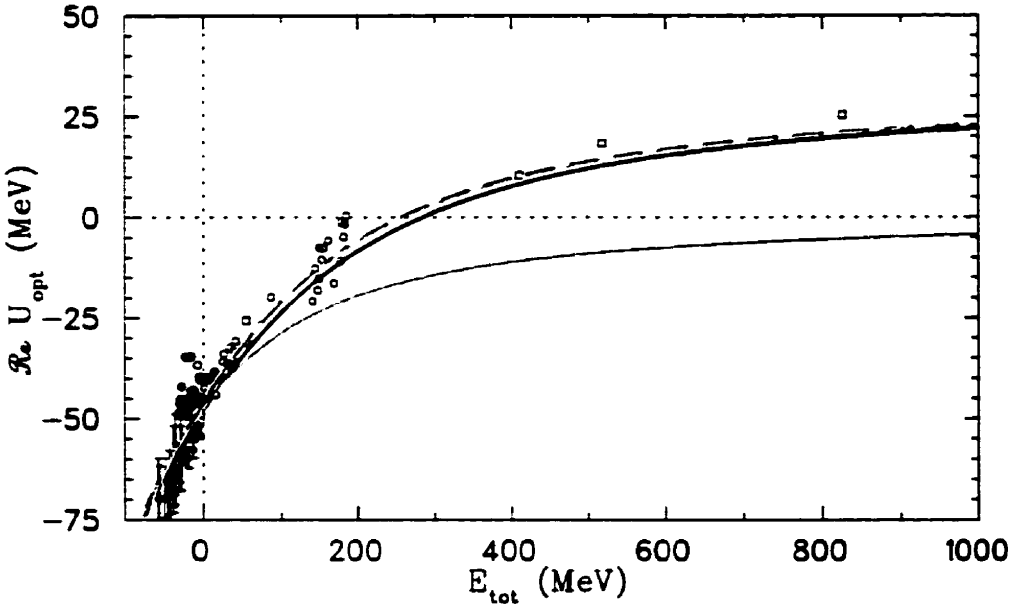

Figure 3.1: Extraction of the real part of the nuclear optical potential from nucleon-nucleus scattering data as a function of total energy. The open (solid) circles are for proton (neutron) beams incident on a variety of heavy nuclei (^{28}Si,^{40}Ca,^{48}Ca,^{58}Ni,^{90}Zr,^{208}Pb) taken from[84]. The solid diamonds are for proton on ^{40}Ca,^{48}Ca,^{58}Ni,^{90}Zr reactions taken from[85]. The open squares are for proton-^{40}Ca reactions taken from[86]. The dark (shaded) lines are for the MDYI (GBD)-type momentum-dependent parametrization of the mean field. The solid (dashed) lines are for a compressibility of $K = 215$ MeV (210 MeV), as shown in table 3.1. The mean fields calculated in this figure are for $T = 0$ MeV at saturation density ρ_0.

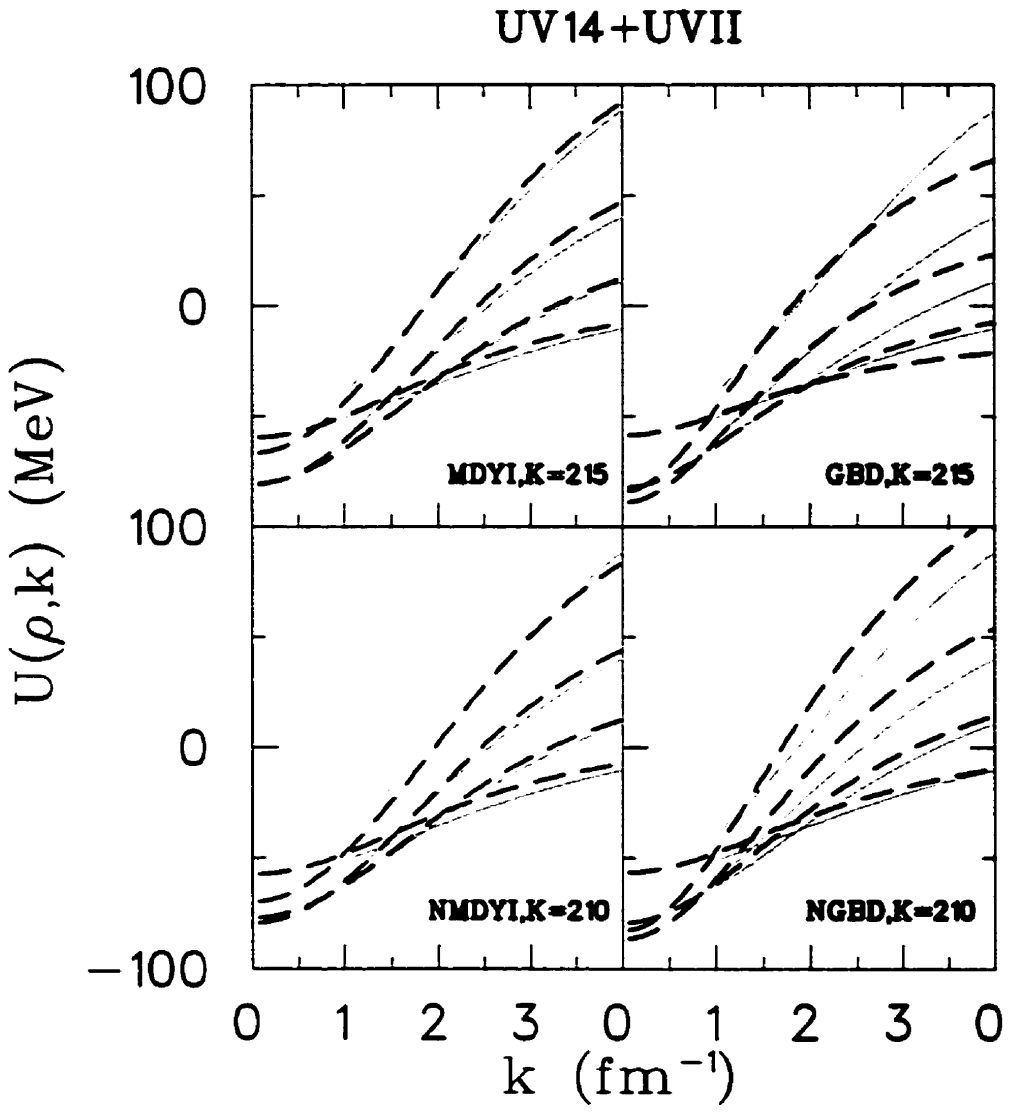

Figure 3.2: Nucleon single-particle potential as a function of momentum for different densities. We present the single-particle potential felt by a nucleon in cold nuclear matter for densities of $\rho = 0.1,0.2,0.3$ and 0.4 fm^{-1} starting from the lowest curve (at high momentum) to the highest curve in all panels. The GBD and MDYI-type potentials are computed using the coefficients given in table 3.1 and are given by the dashed lines. The thin shaded solid lines are the parameterizations from Wiringa[87] for the UV14+UVII potential.

saturation density for the four momentum-dependent mean fields used in this work. We note that for all nuclear collisions studied in this work (c.f. chapters 5 and 6) the maximum density attained never exceeds this limit. As a comparison, we show the parameterization[87], of the results of a microscopic calculation of the single-particle potential used in the calculation of neutron star masses[88]. These single-particle potentials were obtained with a variational procedure which uses a detailed nucleon-nucleon two-body interaction[89] and a phenomenological three nucleon interaction term[90, 91, 92]. Both of these interactions closely reproduce the nucleon optical potential presented in figure 3.1 as well as reproducing some neutron star data. However, the compressibility of $K = 224$ (269) MeV for the interaction labelled **UV14+UVII** in figure 3.2 (**UV14+TNI** in figure 3.3) of this parameterization is too stiff to allow for prompt supernova explosion mechanisms[88]. The two figures 3.2 and 3.3 differ in the phenomenological three-nucleon interaction term. From these figures, we see that our potentials agree quite nicely with the microscopic calculations at saturation density. As we move (above) this density region, the agreement is not as good. However, the trends are remarkably similar considering the simplifications used to obtain the MDYI and GBD potentials. We note that all potentials become more repulsive as both density is increased and as momentum is increased above the Fermi surface, which is $k_f \sim 1.33$ fm^{-1} at nuclear saturation density ρ_0. Note also that the microscopic calculations of the nuclear matter potentials become more uncertain at higher densities, as their parameters are fitted to measured nuclear properties.

More recent nuclear matter calculations have been perfomed in the context of the neutron star matter equation of state[93, 94]. In these model calculations, an improvement over the microscopic potentials displayed in figures 3.2 and 3.3 is obtained by considering a modern[7] two-nucleon interaction term[95] that closely matches

[7]Modern here means that fits to nucleon-nucleon scattering from the Nijmegan database yield χ^2 per degree of freedom less than 1.

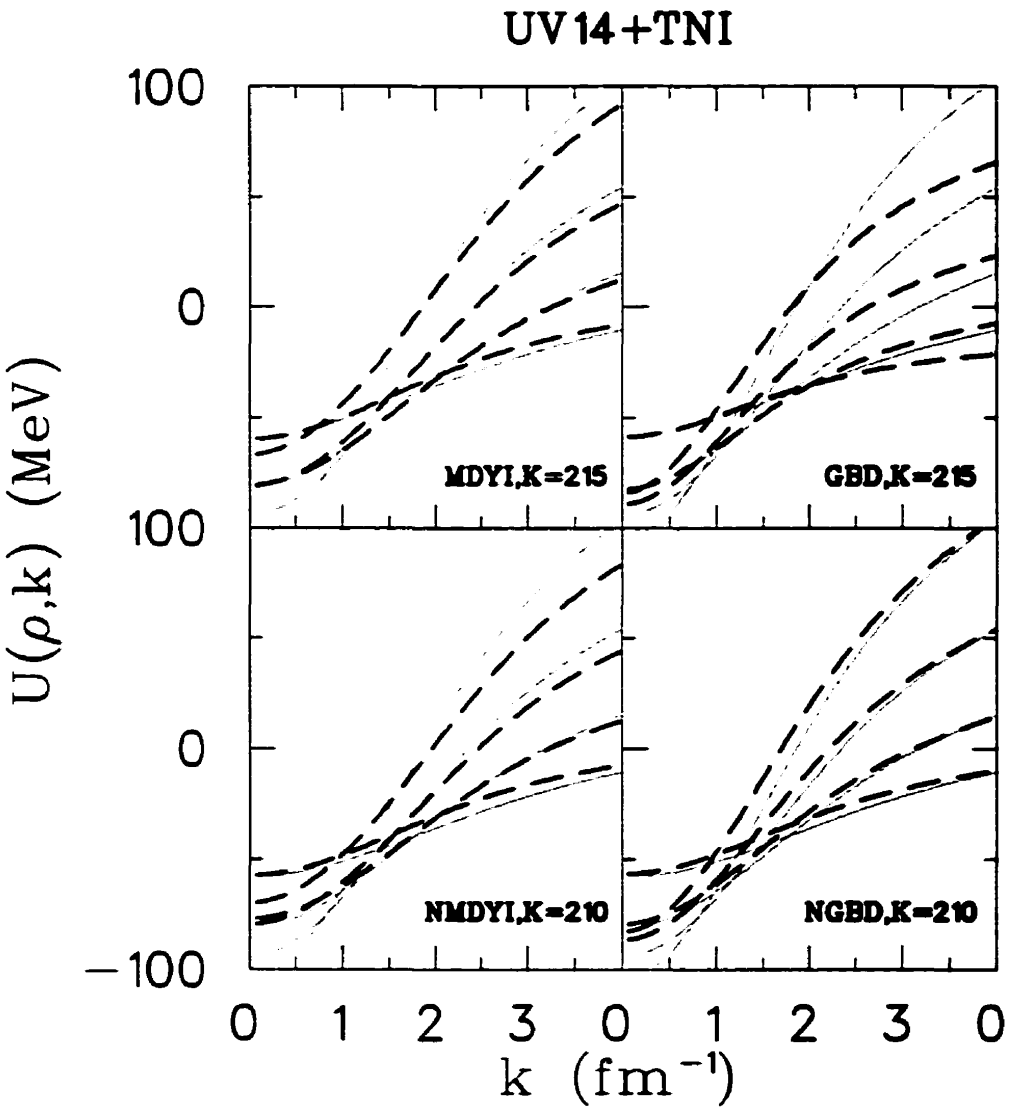

Figure 3.3: Same as figure 3.2 for the UV14+TNI potential of Wiringa[88, 87].

nucleon-nucleon scattering phase shift analysis from the Nijmegen database[96] as well as incorporating relativistic corrections to the two-nucleon interaction term[97]. The phenomenological three-nucleon interaction is taken from [98] where the calculated binding energies of light ($A \leq 6$) nuclei were accurately reproduced. For comparison with the momentum-dependent potentials used in this work, we show in figures 3.4 (for $K = 215$ MeV) and 3.5 (for $K = 210$ MeV) the nuclear matter equation of state obtained with our GBD and MDYI potentials as well as the improved microscopic treatment in [93, 94]. Note that the MDYI ($K = 215$ MeV) and NMDYI ($K = 210$ MeV) do not differ significantly in neither the single-particle potential nor in their equation of state. However, the GBD ($K = 215$ MeV) and NGBD ($K = 210$ MeV) differ significantly in the single-particle potential at high energy (momentum). For completeness, we present all these four potentials in figures 3.4 and 3.5. In addition to the zero temperature behaviour of the momentum-dependent potentials we have adopted, we also show the finite temperature behaviour of these potentials in terms of the equation of state. The equation of state for the microscopic study is shown for zero temperature and corresponds to a compressibility of $K = 260$ MeV. From the figures we see that excellent agreement between our phenomenological potentials and the microscopic treatment is obtained for zero temperature matter up to $\sim$2.5 times nuclear saturation density. We repeat that for all nuclear collisions studied in this work the maximum density attained never exceeds this limit. The MDYI, NMDYI and GBD potentials slightly underestimate the energy per nucleon above $\rho \sim 2\rho_0$. The NGBD potential slightly overestimates E/A above $\rho \sim \rho_0/2$. For the pressure, the MDYI, NMDYI and GBD potentials slightly underestimate the pressure at zero temperature for ρ greater that $\sim 2\rho_0$ as compared with the microscopic calculation. The NGBD potential agrees quite well with the microscopic calculation for the entire density range displayed in the figure.

Up to now, all cases presented are for symmetric nuclear matter. That is, matter with an equal number of neutrons and protons. As we will eventually be interested

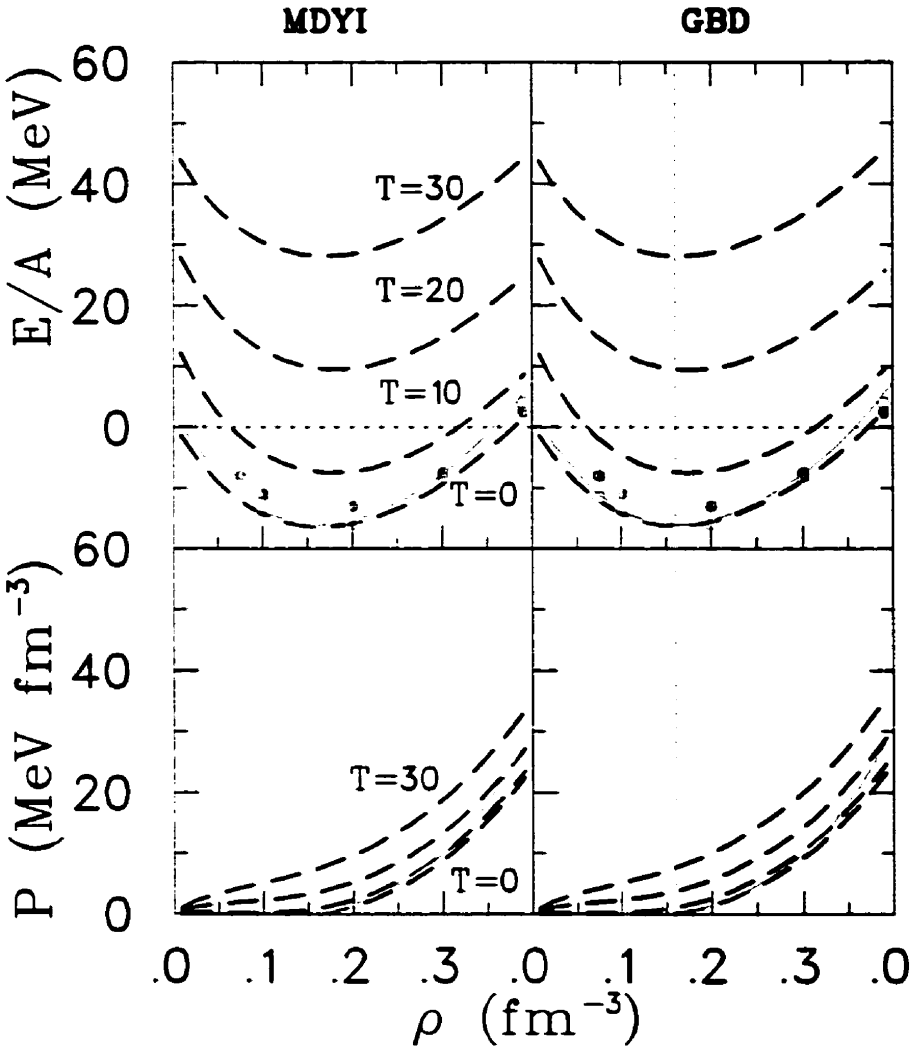

Figure 3.4: Nuclear matter equation of state for cold symmetric matter for the A18+δv+UIX* as calculated in [93, 94] (thin shaded solid line). From the bottom in each panel, we present the equation of state for symmetric nuclear matter with a GBD and MDYI-type potential for $T = 0,10,20$ and 30 MeV (dashed lines). Both of the latter potentials are for a compressibility of $K = 215$ MeV as shown in table 3.1. The microscopic calculation corresponds to a compressibility of $K = 260$ MeV. We also show the binding energy per nucleon obtained with the microscopic calculation of the mean fields from figures 3.2 and 3.3. The solid (open) circles are for the **UV14+UVII** (**UV14+TNI**) interaction.

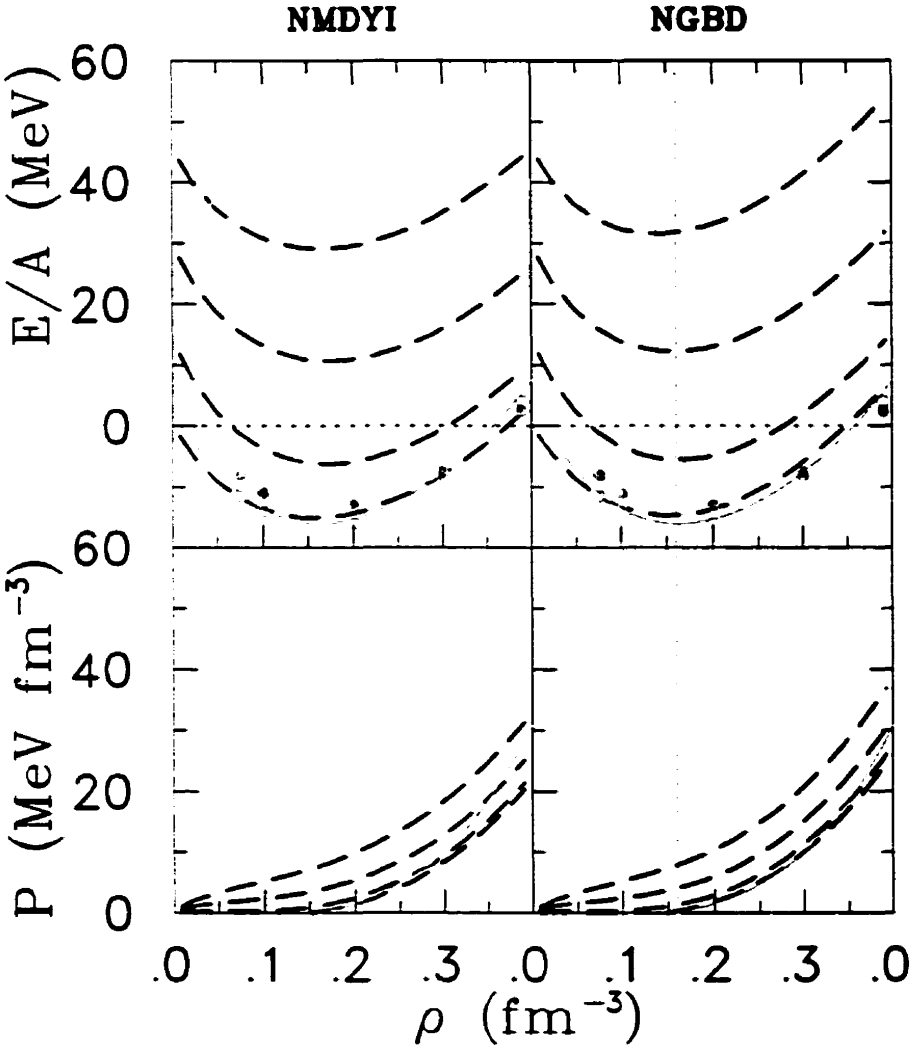

Figure 3.5: Same as figure 3.4 for GBD and MDYI potentials of compressibility $K = 210$ MeV as shown in table 3.1. The microscopic calculations are as in figure 3.4.

in the properties of nuclear matter far from the isospin zero case, we now introduce a new term in our single-particle potential to take into account this (isospin asymmetry) aspect. In reference[99], several phenomenological parametrizations for this isospin term were given. In reference[100] it was shown that a more detailed analysis of the parametrizations in [99] favours a linear dependence of the symmetry energy on density. We chose to adopt this functional form for the symmetry energy added to the single-particle energy presented in equation (2.20). Our symmetry term thus reads:

$$u^{iso}(\vec{r}, \tau_3) = -\tau_3 \frac{2D}{\rho_0} (\rho_n(\vec{r}) - \rho_p(\vec{r})) . \tag{3.13}$$

In the above, τ_3 is the third component of the nucleon isospin and is equal to $+1/2$ $(-1/2)$ for protons (neutrons). The ρ_n and ρ_p are local neutron and proton densities respectively. The strength of the isospin potential is given by D. Empirically, it is found that $D = 30 \pm 4$ MeV. furthermore, support for D ranging from $27 - 40$ MeV is found from various phenomenological calculations [100, and references therein]. We adopt the value of 32 MeV used by several authors[101, 102] in the context of simulations of colliding heavy ions. Equation (3.13) indicates that the attractive part of the single-particle potential for protons (neutrons) will be stronger (weaker) for matter with a neutron density in excess of a proton density, weaker (stronger) vice-versa. With this additional isospin term, we present the pure neutron matter equation of state in figure 3.6 both for the GBD and MDYI-type mean fields as well as the work in [93, 94]. It is evident from this figure that our isospin-modified mean field potentials are able to reproduce quite well the recent microscopic calculation. We note that introducing the above isospin term in effect restores this dependence of the nucleon-nucleon potential energy interaction term that was omitted in section 3.1, albeit in a phenomenological manner. For the above comparison, cold nuclear matter is assumed. Note that the pure neutron matter equation of state is much stiffer than the corresponding nuclear matter equation of state.

From the analysis presented in this section, we conclude that the momentum-

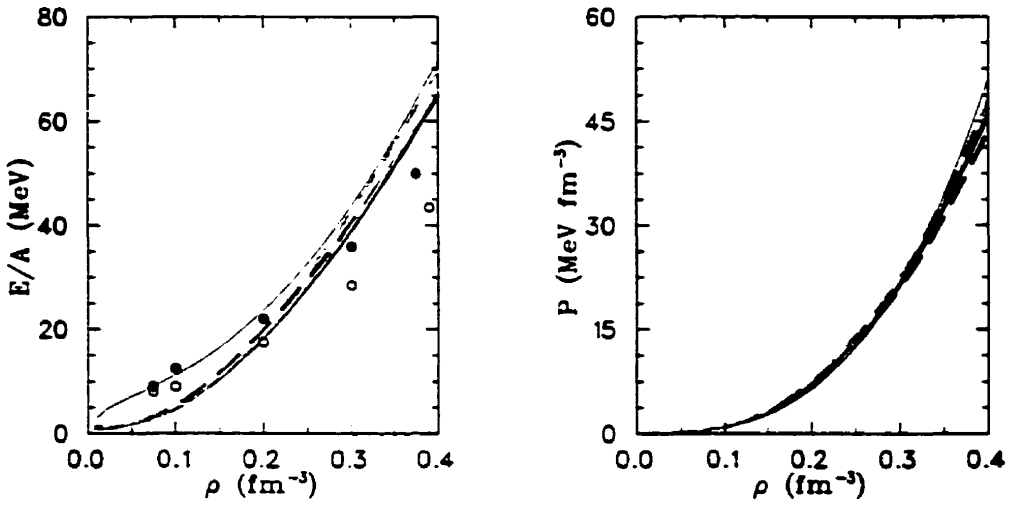

Figure 3.6: Pure neutron matter equation of state at $T = 0$ MeV as calculated in [93. 94] (thin solid line). The thick lines show the pure neutron matter equation of state at $T = 0$ MeV for the GBD and MDYI-type potentials used in this work. The thick dark lines are for the MDYI (solid) and NMDYI (dashed) mean field. The thick shaded lines are for the GBD (solid) and NGBD (dashed) mean field. We also show the binding energy per neutron for pure neutron matter obtained with the microscopic calculation of the mean fields from figures 3.2 and 3.3. The solid (open) circles are for the **UV14+UVII** (**UV14+TNI**) interaction.

dependent parameterizations of the mean field for both the MDYI and GBD type potentials display excellent agreement with detailed microscopic calculations of the many-body nucleon interaction. These are shown both for the equation of state calculated with modern nucleon-nucleon interactions as well as the optical potential (single-particle potential). We note that the density-dependent (momentum-independent) mean field potentials (not shown) also closely reproduce the equation of state as calculated microscopically. However, the momentum-independent mean field cannot correctly reproduce the optical potential and as such presents serious drawbacks. In addition, we note that all comparisons performed here are done for equilibrium nuclear matter. In forthcoming chapters, we will investigate non-equilibrium behaviour of the mean fields presented here by considering dynamical simulations of colliding heavy ions.

3.2 Nucleon-Nucleon Cross Sections

We next turn to the other input required for the BUU equation. As we have already seen in section 2.3, the BUU equation is the Vlasov equation extended to include (two-body) nucleon-nucleon scattering processes. In that section, the nucleon-nucleon cross section which serves as an input for calculating the effects due to these scattering processes, has yet to have been discussed. Traditionally, the *free-space* nucleon-nucleon total cross section has been used, however, there are some modifications that are necessary due to the (momentum-dependent) mean field that we introduced in section 3.1. To see this explicitly let us consider the expression for the nucleon-nucleon cross section, which is given by:

$$\sigma = \frac{transition\ \ rate}{incident\ \ flux}.$$

Using Fermi's golden rule for a transition from an initial state "i" to a group of final states "f", the transition rate is:

$$W_{fi} = \frac{2\pi}{\hbar} D_f \, t_{fi}|^2.$$

where D_f is the density of final states and t_{fi} is the transition matrix element between initial and final states. Identifying the incident flux as the initial state density times the relative velocity of the colliding partners, we then obtain an expression for the total cross section:

$$\sigma = \frac{2\pi V}{\hbar} \frac{D_f}{v_{rel}} \, t_{fi}|^2.$$

where v_{rel} is the initial relative velocity of the colliding partners. The above cross section is for two particles colliding in vacuum. In our case however, collisions occur not in vacuum, but in the nuclear medium. Thus we must replace the above cross section with the following:

$$\sigma^* = \frac{2\pi V}{\hbar} \frac{D_f^*}{v_{rel}^*} |t_{fi}^*|^2.$$

where the starred quantities represent in-medium values. Many-body investigations support the fact that $t_{fi}^* \sim t_{fi}$[27, and refs. therein]. We will follow this line of thought here. In [27], the in-medium cross-section is calculated as is here, however a simplified momentum-dependence in the mean field potential was used. We rewrite the in-medium elastic scattering cross section as:

$$\sigma^* = \frac{v_{rel}^{(0)}}{v_{rel}^*} \frac{D_f^*}{D_f^{(0)}} \sigma. \tag{3.14}$$

Thus, we obtain an expression for the in-medium cross section in terms of the ratios of the free space and in-medium values of D_f and v_{rel} and the free space cross section. To evaluate equation (3.14), will work in the nucleon-nucleon centre of mass frame. Thus, the momenta depicted in figure 2.1 are relabeled to the following:

$$\vec{p} \rightarrow +\vec{p}_i$$

$$\begin{aligned}\vec{p}_1 &\rightarrow -\vec{p}_i \\ \vec{p}' &\rightarrow +\vec{p}_f \\ \vec{p}'_1 &\rightarrow -\vec{p}_f.\end{aligned}$$

The relative velocities can be obtained immediately from equation (3.12), they read:

$$\begin{aligned}v_{rel}^{(0)} &= \frac{2p_i}{m}, \\ v_{rel}^{*} &= \left|\frac{\vec{p}_i}{m^*(\vec{p}_i)} + \left(\frac{\vec{p}_i}{m^*(-\vec{p}_i)} + \nabla_{\vec{p}_i} u(\rho_1, -\vec{p}_i)\right)\right|. \end{aligned} \tag{3.15}$$

The density of final states will be proportional to the number of momentum states $\vec{p}_f$ satisfying energy and momentum conservation laws for the two-particle scattering process. Symbolically, we write the following, where C is some proportionality constant.

$$D_f = C \int d^3p' \, d^3p'_1 \, \delta(\vec{p}' - \vec{p}'_1)\delta(\epsilon - (\epsilon' + \epsilon'_1)) \tag{3.16}$$

In the above equation, ϵ is a fixed number that gives the total single-particle energies in the initial state. That is,

$$\epsilon = \frac{\vec{p}_i^{\,2}}{2m} + u(\rho_1, \vec{p}_i) + \frac{(-\vec{p}_i)^2}{2m} + u(\rho_2, -\vec{p}_i).$$

In order to proceed any further, we note that a closed form solution for equations (3.15) and (3.16) can be obtained if we assume an equilibrium nuclear matter distribution. In this case, $u(\rho, \vec{p}) = u(\rho_0, |\vec{p}|)$ and we then arrive at

$$D_f = C\frac{(p'')\; m^*(\vec{p}'')}{2} \int d\Omega \delta(\theta - \theta'')\delta(\phi - \phi'') \tag{3.17}$$

where the p'' is chosen to satisfy the energy conserving delta function in equation (3.16). For the elastic collisions we consider in this work, $p'' = p_i$. Using equations (3.14), (3.15) and (3.17), an expression for the in-medium cross section in equilibrium nuclear matter is thus obtained. We get:

$$\sigma^* = \left(\frac{m^*}{m}\right)^2 \times \sigma. \tag{3.18}$$

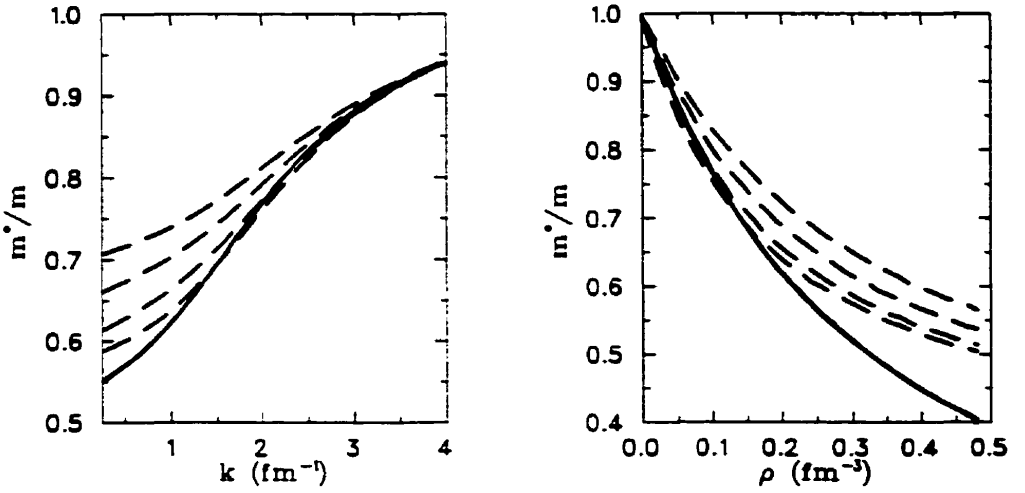

Figure 3.7: Nucleon effective mass as a function of momentum and density in nuclear matter at temperatures of $T = 0.10.20$ and 30 MeV from the lower to the upper curves respectively. The dashed (solid) lines are for the MDYI (GBD)-type momentum-dependent mean field of compressibility $K = 210$ MeV. Note that for the GBD potential, all temperature curves are indistinguishable.

We thus find that the modification to the in-medium cross section involves only the nucleon effective mass and since the nucleon effective mass is equal to the real mass for momentum-independent potentials, there is no modification of this type to the free-space cross section with momentum-independent potentials.

The effective mass will, in general, be a function of density and momentum. This is a reflection of the single-particle potential which is also a function of the said variables. We show these functional relationships for both the GBD and MDYI-type mean fields for zero and finite temperature equilibrium nuclear matter in figure 3.7. This figure indicates that for both potentials, the effective mass approaches the free space value in the high momentum and low density limit. In addition, the MDYI-type mean field produces an effective mass which approaches the free space value as the temperature is increased. Note that this behaviour is absent for the GBD-type mean field. This can be seen by inspection of equation (3.11). Here we see that the

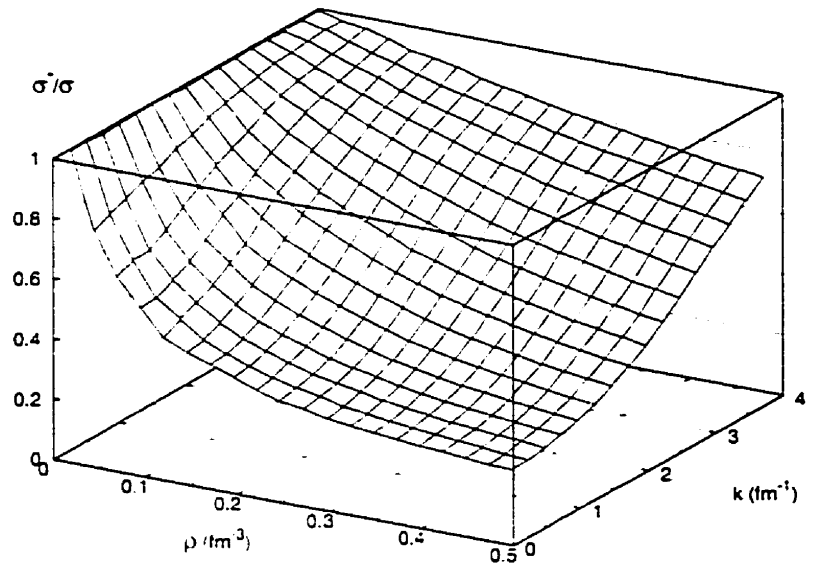

Figure 3.8: Ratio of the in-medium to that of the free space elastic cross section in cold equilibrium nuclear matter obtained with the MDYI-type mean field potential as a function of both density and momentum.

temperature dependence enters via the third term in that expression, and in that term, any $\vec{p}$ dependence is integrated out. Hence, there is no temperature dependence of the effective mass with this potential. In figure 3.8 we show the ratio of the in-medium to that of the free space elastic cross section for cold equilibrium nuclear matter obtained with the MDYI-type mean field parameterization as a function of both density and momentum. We note that the right panel of figure 3.7 indicates that the nucleon effective mass decreases with increasing density. One would thus expect the equation of state to permit superluminal behaviour at high density. We find that this is indeed the case for densities above $\sim 5\rho_0$, and thus carries no consequences for our work.

So far, we have neglected to mention the actual value of the free space nucleon-nucleon elastic cross section[8] . Cugnon[103] has presented a parameterization of

[8]From here-on, we will refer to the entrance channels in which $|\tau_3|$=1 as the isospin symmetric

the latter for both the isospin symmetric channel ($pp \rightarrow pp$ and $nn \rightarrow nn$) and the isospin antisymmetric channel ($np \rightarrow np$) based on world data compilations. We present this parameterization in the left panel of figure 3.9. Below $k_{CM} \sim 0.5$ fm^{-1}, the cross sections increase approximately as k_{CM}^{-2}. As collisions at these low energies are well below the Fermi surface, most of them are Pauli blocked (c.f. section 4.3.2, where Pauli blocking efficiency for cold nuclei is ~96%). We thus introduce an artificial truncation of the cross section at 150 mb (1 mb = 10^{-31} m^2) as shown in the figure. This corresponds to k_{CM} ~0.263 fm^{-1} (0.348 fm^{-1}) for the isospin symmetric (anti-symmetric) elastic scattering channel. The cross section presented in the left panel is the free space value. In the right panel, we re-plot the parameterization for the isospin antisymmetric channel along with the in-medium value for cold equilibrium nuclear matter obtained from the $\rho = \rho_0$ slice in figure 3.8. As previously mentioned, the momentum-independent parameterization of the mean field does not give a value for the in-medium cross section different to that of the free space value as we have calculated it. However, in order to account for a decrease in the former, some authors have used a constant scaling factor[104, 105] and others have included a phenomenological density-dependent reduction based on the first term in a Taylor expansion of the cross section in terms of density[106, 107]. This parameterization takes the form:

$$\sigma^* = (1 - \alpha\rho/\rho_0)\sigma. \tag{3.19}$$

We have also shown in figure 3.9, the in-medium cross section for this parameterization for a value of $\alpha = 0.20$. In view of the momentum-dependent self-consistent calculation of the in-medium nucleon-nucleon cross-section presented in this work, the parameterization presented in equation (3.19) is clearly oversimplified. However, as this in-medium cross section has been used extensively throughout the literature, we will also examine the above parameterization in this work. In section 4.3.2 we

channel ($pp \rightarrow pp$ or $nn \rightarrow nn$), and entrance channels with $|\tau_3|$=0 as the isospin anti-symmetric channel ($np \rightarrow np$), where τ_3 is the third component of isospin of the nucleon-nucleon system.

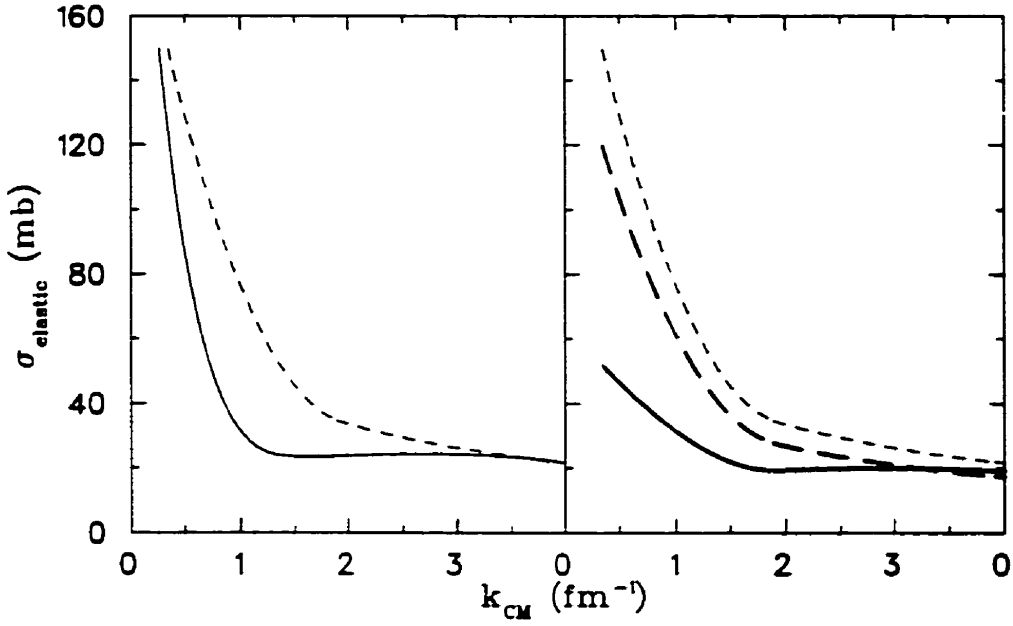

Figure 3.9: Parameterization of the elastic nucleon-nucleon cross section as presented by Cugnon[103], left panel. The solid line corresponds to $pp \rightarrow pp$ and $nn \rightarrow nn$ collisions and the dashed line corresponds to $np \rightarrow np$ collisions. The abscissa is the momenta of one of the colliding pairs in the collision centre of mass frame. In the right panel, we re-plot the $np \rightarrow np$ parameterization (thin dashed line) along with the momentum-dependent modification for zero temperature equilibrium nuclear matter (thick solid line) and a modification obtained with a density-dependent phenomenological reduction of coefficient $\alpha = 0.20$ (thick dashed line) as described in the text.

will return to a detailed comparison of the two in-medium cross-sections presented here.

Chapter 4

Vlasov/BUU Solution for Finite Nuclei

The previous chapters have presented the problem we wish to address, namely a solution of the BUU equation, along with the necessary inputs. In this chapter we address the numerical techniques used to solve (2.19), the Vlasov equation as a first approximation to the BUU equation (2.24). Furthermore, we address the limitations (in terms of numerical accuracy) that we are presented with in attaining such a solution. We then show how we introduce nucleon-nucleon collisions and the self-consistent modification to the free space cross section, thus giving the BUU solution. As our ultimate goal is a simulation of colliding heavy ions, we must provide a description of how we use the nuclear matter many-body techniques presented so far to describe finite nuclei. We thus begin this chapter by showing how we make this connection.

4.1 Finite Nuclei

The methods we have developed so far, in particular, the solution of the nuclear matter many-body problem, have made no mention of finite nuclei. In this section,

we make a connection between the two.

The nuclear matter description presented so far has neglected the Coulomb potential. We remind the reader that in the nuclear matter approximation, one attempts to obtain an expression for the energy density of the system due to the short range nuclear force. As a nucleus contains charged nucleons, it will then be necessary to include the Coulomb term into our description of finite nuclei. Having said this, we then rewrite the potential energy density to include for this effect:

$$V_\alpha = V_\alpha^{nuc} + V_\alpha^{iso} + V_\alpha^{Coul}, \tag{4.1}$$

where V_α^{nuc} can be the Skyrme, MDYI or GBD potential energy density from section 3.1, V_α^{iso} is the isospin potential energy density derived from equation (3.13), and V_α^{Coul} is the new Coulomb potential energy density contribution to the total energy density. The index α labels a configuration space point. Calculation of the Coulomb potential field is accomplished by numerically solving the Poisson equation on a three-dimensional grid[108]. We stress that the addition of these terms is introduced in order to better approximate finite nuclei. The V_α^{nuc} that we use in equation (4.1) is taken from the nuclear matter approximation which neither takes into account Coulomb interactions nor any dependence upon isospin. By introducing these terms, we have effectively given the protons and neutron separate identities. We note that in general, the nuclear part of the mean field is about 6 times greater than the Coulomb term and about 50 times greater than the isospin term. However, depending on the mass and atomic numbers of the nuclei and also on the collision dynamics between nuclei, these ratios may vary.

In order to generate a nucleus, we must specify a phase space initialization of the nucleons. That is, we must assign positions and momenta to each nucleon within the nucleus. We use the observed properties of nuclei to aid us here. In particular, nucleon-nucleus scattering experiments (c.f. Rutherford scattering, nuclear α decay, pion atomic transitions [109]) provides us with a mass-radius relationship for nuclei.

Specifically,

$$R_A = R_0 A^{\frac{1}{3}}, \tag{4.2}$$

where R_A is the matter radius for a nucleus containing A nucleons, and R_0 is a parameter determined from the aforementioned scattering experiments. We use the experimentally determined value of $R_0 = 1.14$ fm. Initialization of the nuclei is then accomplished in the following manner. Each nucleon in the A nucleon nucleus, is randomly assigned a position in a sphere of radius R_A. Note that A hard-packed spheres in a spherical volume of radius $R = R_0 A^{\frac{1}{3}}$ implies a nucleon hard-sphere radius of $0.80 R_0$. We reject the assigned position of a nucleon if its centre falls within $2d_0$ of the centre of another nucleon, where $d_0 = 0.80 R_0$. This process gives the nucleus an initially smooth density profile.

Once the configuration space distribution of the nucleons is determined, the local density is determined for each. From this density, the (local) Fermi momenta (c.f. [109]) is then determined via

$$p_f = \left(\frac{6\pi^2 \rho}{g} \right)^{\frac{1}{3}} \tag{4.3}$$

Where g is the degeneracy of a nucleon ($g = 4$ accounts for the two spin and isospin states of the nucleon). Assigning of momenta for the nucleons is then carried out in the same manner as for positions, replacing the R_A with the local p_f for each nucleon. No minimum separation distance in momentum space is enforced for this initialization. This is the procedure carried out by many authors and it known as the *local* Thomas-Fermi procedure. See [22] for example.

It should be mentioned that an initial state could also be chosen as a stationary point of the Vlasov equation. That is, the initial phase space density should satisfy the time-independent Vlasov equation. The latter is obtained by setting the time derivative of the phase space density to zero in equation (2.19). This is known as the Thomas-Fermi solution[1]. For the momentum-dependent potentials chosen in this

[1] As opposed to the *local* TF procedure mentioned above.

work, this initialization procedure is somewhat time-consuming and we have chosen the much simpler initialization procedure outlined above.

4.1.1 Matter and Charge Radii for Isospin Asymmetric Nuclei

Nuclei with low mass numbers typically have neutron and proton numbers that do not stray too far from one-another. For heavier nuclei however, the ratio of neutron number to proton number for stable nuclei can be as large as ~ 1.5 for Au, and even higher for radioactive nuclei. We thus define the isospin asymmetry of a nucleus to be $(N - Z)/A$, where N, Z and A are the neutron, proton and mass numbers of a nucleus respectively. It is a well known experimental fact, that nuclei with a non-zero isospin asymmetry have different neutron and proton radii. In general, the neutron radii exceeds that of the proton radii. A recent relativistic mean field theory calculation by Warda[110], gives parameterization of the two latter radii for nuclei with mass numbers in excess of $A = 60$. In figure 4.1 we show the skin thickness, $\Delta t = R_n - R_p$, where R_n and R_p are respectively the neutron and proton radii obtained from [110]. As we will later be concerned with nuclei with mass numbers smaller than 60 in addition to heavier nuclei, we have used an extrapolation of the parameterization in [110] for mass numbers smaller than 60 that is linear in mass and expanded in powers of the isospin asymmetry term up to third order. This extrapolation matches the results from [110] at mass number 60 and vanishes for zero mass number and zero asymmetry parameter.

To account for the finite skin thickness present in heavy nuclei, the initialization procedure described in section 4.1 is modified. We define the new (neutron and proton) radii for a mass A nucleus as:

$$R_n = R_A + \frac{\Delta t}{2} \qquad R_p = R_A - \frac{\Delta t}{2}.$$

The configuration space distribution of the neutrons (protons) is then carried in the

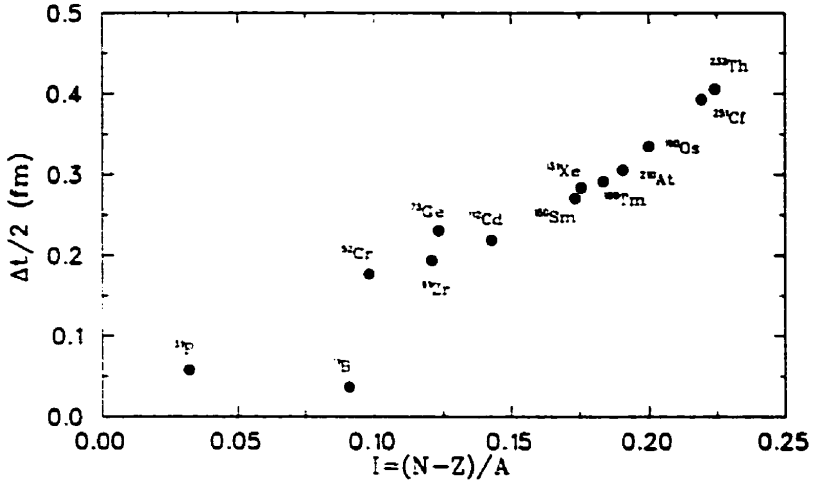

Figure 4.1: Neutron skin thickness for several nuclei as a function of the isospin asymmetry. The skin thickness here is as defined in [110].

same manner as in section 4.1, except we now use R_n (R_p) in place of R_A. In addition, the momentum initialization is carried out separately for neutrons and protons using equation (4.3), with a value of $g=2$ to account for the spin degeneracy of the neutron and proton. In figure 4.2, we show the average neutron and proton radii from 10 separate initializations for both a ^{208}Pb and a ^{32}S nuclei. The figure indicates that the initialization procedure just mentioned gives the Pb nucleus a neutron skin thickness of ~ 0.6 fm (about 25% of the total Pb volume)[2], and no neutron skin thickness for the isospin symmetric S nucleus. The density in this figure was calculated by counting the number of nucleons (neutron and protons separately) in a thin spherical shell at a given distance from the centre of the nucleus and dividing by the volume of this shell. We note that we do not see a sharp edge in the radii since we are sampling a finite number of particles[3]. This isospin-dependent initialization procedure is carried out only when we include an isospin term in our potential. Without this term, the nuclei are initialized as discussed in the previous section. Also in figure 4.2 we show the experimentally determined charged radius for the Pb and S nuclei. We find a small

[2]This value assumes a hard-sphere cut-off.

[3]See section 4.2.1 for more explanation of this point.

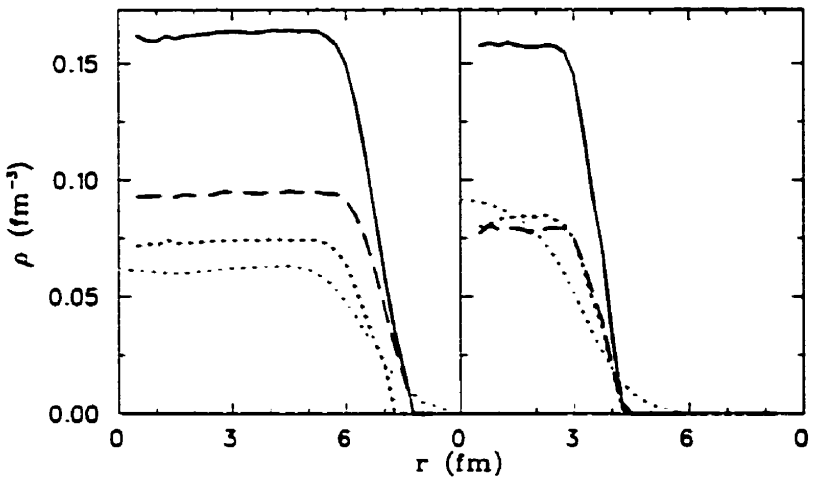

Figure 4.2: Nuclear profiles for heavy (^{208}Pb, left panel) and light (^{32}S, right panel) nuclei. The solid curve is for total nucleon density and the dashed (dotted) curve is for neutron (proton) density. The curves shown are the average values obtained after 10 independent initializations as described in the text. The neutron skin thickness for the larger nuclei is $\sim$ 0.6 fm. The shaded dotted line is the experimentally measured charge density[114].

discrepancy between the (charge) density obtained in this work and the measured charge density.

We generate our nuclei with finite neutron skins. It has been shown that the inclusion of the neutron skin for heavy nuclei in simulations of low energy ($\sim \epsilon_f$) heavy ion collisions is essential for explaining some observed experimental signals. In particular, the study of low energy directed flow[111, 112, 113] at high impact parameter is difficult to explain without the initial isospin-dependent nuclear profiles. Finally, in order to remain consistent with our choice of including isospin effects in the nuclear mean field as well as in the nucleon-nucleon collision cross section, we choose to adopt the isospin-dependent initialization for the nuclear profiles.

4.2 Solutions of the Vlasov equation

4.2.1 Test Particle Solution

We recall in section 2.2.1. we presented the Vlasov equation (2.19) as a semi-classical solution to the nuclear many-body problem. From this equation, we wish to find solutions which describe the trajectory of points in classical phase space. As an analytical solution of the Vlasov equation is prohibitive, we seek a numerical one. An often used solution is the "test-particle" solution[21, 28, 115]. This method consists of projecting the (continuous) semi-classical phase space density onto a collection of test particles, each with a well defined position and momentum as outlined in the previous section. The test particles do not necessarily have to have a one-to-one correspondence with nucleons. In fact, to give a better representation of phase space, it can be advantageous to use a very large number of test particles. In addition, energy conservation considerations demand that the number of test particles (per nucleon) to be large ($\sim 100 \rightarrow 1000$). We define this number to be $N = A \times N_{ens}$, where A is the actual number of real nucleons in our system, and N_{ens} is some positive integer that represents the number of *ensembles* in our system.

To begin our analysis, we first note that for a collision-less system (such as the one governed by Vlasov dynamics), Liouville's theorem tells us that the total time derivative of the phase space density is zero:

$$\frac{df(\vec{r},\vec{p})}{dt} = \frac{\partial f(\vec{r},\vec{p})}{\partial t} + \frac{\partial \vec{r}}{\partial t}\cdot\nabla_{\vec{r}} f(\vec{r},\vec{p}) + \frac{\partial \vec{p}}{\partial t}\cdot\nabla_{\vec{p}} f(\vec{r},\vec{p}) = 0. \tag{4.4}$$

Direct comparison of this with the Vlasov equation leads to the following set of conditions:

$$\frac{\partial \vec{r}}{\partial t} = \nabla_{\vec{p}} h(\vec{r},\vec{p}) \qquad \frac{\partial \vec{p}}{\partial t} = -\nabla_{\vec{r}} h(\vec{r},\vec{p}). \tag{4.5}$$

These are Hamilton's equations of motion for a particle at $\vec{r}$ with momentum $\vec{p}$, where $h(\vec{r},\vec{p})$ is the single-particle Hamiltonian. Thus, if we evolve our test particles respecting these equations, we will have a (test particle) solution of the Vlasov

equation. Due to the finite sampling of phase space, the test particle method does suffer from fluctuations. This can be clearly understood if we examine the density for example. The discretized version of equation (2.21) for the test particle distribution reads:

$$\rho(\vec{r}) = \frac{1}{N_{ens}} \sum_{i}^{A \times N_{ens}} \delta(\vec{r} - \vec{r}_i).$$

Clearly for finite N_{ens}, the density will fluctuate. Since the (momentum-independent for example) single-particle potential depends solely on the density, one can then expect (unwanted large) fluctuations in the former. This problem can be somewhat circumvented by using a large N_{ens} and introducing an *artificial* smoothing via a configuration space lattice. In this case, on a lattice of spacing δx, where x_α is the centre of cell α, in one dimension, the density then reads:

$$\rho(x) = \rho_\alpha = \frac{1}{N_{ens} \times \delta x} \sum_{\alpha j}^{j=A \times N_{ens}} \Theta(\frac{\delta x}{2} - |x_\alpha - x|)\Theta(\frac{\delta x}{2} - |x_\alpha - x_j|). \qquad (4.6)$$

where the first step function picks out the cell α where position x is located, and the second step function selects all particles in this cell. Thus, a given (test) particle contributes to configuration space with a finite width. It (test particle) is in fact spread out evenly over the entire configuration space cell. This prescription reduces fluctuations, but is an somewhat ad-hoc prescription. Note that with this method, a particle contributes to its local cell irrespective of its position relative to the centre of the cell. We will instead turn to a more formal grid-based method, in the next section.

4.2.2 Lattice Hamiltonian Solution

The last section introduced the test particle method as a solution to the Vlasov equation. Although quite useful, it suffers somewhat from fluctuations arising from finite statistics. A more general grid-based method is the *Lattice Hamiltonian* method[30]

which assumes from the beginning a phase space density projected onto a finite configuration space grid of spacing δx. In this method, the contribution to the phase space distribution function at a cell α due to a collection of test particles is:

$$f(\vec{r},\vec{p}) \rightarrow f(\vec{r}_\alpha,\vec{p}) \rightarrow f_\alpha(\vec{p}) = \sum_i^{A\times N_{ens}} R(\vec{r}_\alpha - \vec{r}_i)\delta(\vec{p}-\vec{p}_i). \tag{4.7}$$

That is, for a given $\vec{p}$, phase space is defined up to a configuration space lattice site α. In the above equation, R is a configuration space form factor and the delta function is the momentum space form factor. In addition, $f_\alpha(\vec{p})$ is defined such that particle number is conserved. That is,

$$A = (\delta x)^3 \sum_\alpha \int d^3p\, f_\alpha(\vec{p}). \tag{4.8}$$

With this, the (Lattice Hamiltonian) method asserts that the equations of motion of the test particles "i" are obtained through

$$\frac{\partial \vec{r}_i}{\partial t} = \nabla_{\vec{p}_i} H \qquad \frac{\partial \vec{p}_i}{\partial t} = -\nabla_{\vec{r}_i} H. \tag{4.9}$$

where H is now the *total* N particle Hamiltonian derived from the discrete phase space density $f_\alpha(\vec{p})$. H reads:

$$H = \sum_j^{A\times N_{ens}} \frac{\vec{p}_j^{\,2}}{2m} + N_{ens}(\delta x)^3 \sum_\alpha V_\alpha, \tag{4.10}$$

where V_α is the *potential energy density* at site α for the A-body system as given in equation (4.1). For the MDYI[4] potential introduced in section 3.1, the corresponding discretized version of the single-particle potential and potential energy density read:

$$\begin{aligned} u_\alpha(\vec{p}_i) &= A\frac{\rho_\alpha}{\rho_0} - B\left(\frac{\rho_\alpha}{\rho_0}\right)^\sigma + \frac{2C}{\rho_0}\sum_j \frac{R(\vec{r}_\alpha - \vec{r}_j)}{1+\left(\frac{\vec{p}_i-\vec{p}_j}{\Lambda}\right)^2}. \\ V_\alpha &= \frac{A}{2}\frac{\rho_\alpha^2}{\rho_0} + \frac{B}{\sigma+1}\frac{\rho_\alpha^{\sigma-1}}{\rho_0^\sigma} + \frac{C}{\rho_0}\sum_{jk}\frac{R(\vec{r}_\alpha-\vec{r}_j)R(\vec{r}_\alpha-\vec{r}_k)}{1+\left(\frac{\vec{p}_j-\vec{p}_k}{\Lambda}\right)^2}. \end{aligned} \tag{4.11}$$

[4]See appendix B for the GBD potential.

With this, the Lattice Hamiltonian equations of motion then read:

$$\begin{aligned} \frac{\partial \vec{r}_i}{\partial t} &= \frac{\vec{p}_i}{m} + \mathcal{N}_{ens}(\delta x)^3 \sum_\alpha R(\vec{r}_\alpha - \vec{r}_i) \nabla_{\vec{p}_i} u_\alpha(\vec{p}_i) \\ \frac{\partial \vec{p}_i}{\partial t} &= -\mathcal{N}_{ens}(\delta x)^3 \sum_\alpha u_\alpha(\vec{p}_i) \nabla_{\vec{r}_i} R(\vec{r}_\alpha - \vec{r}_i) \end{aligned} \tag{4.12}$$

As we initially desired a solution to the Vlasov equation, we need to establish a correspondence of these equations with the test particle equations of motion, which are a solution of the former. We note that the test-particle equations of motion are a solution to the Vlasov equation that assumes an infinitesimal grid spacing. In this infinitesimal grid spacing limit, the configuration space form factor in the Lattice Hamiltonian method is $R(\vec{r}_\alpha - \vec{r}_i) = \mathcal{N}_{ens}^{-1}\delta(\vec{r}_\alpha - \vec{r}_i)$. Equations (4.12) then reduce to the test particle equations of motion (4.5). Thus, the Lattice Hamiltonian method can be seen as a grid-based generalization of the test particle solution. The lattice Hamiltonian method considerably reduces fluctuations which plague the test particle method and in general gives much better energy conservation for both the momentum-independent[29, 30] as well as the momentum-dependent[29] mean field potentials. From here-on, we adopt this method. We note that this is this first implementation of the lattice Hamiltonian method for momentum-dependent nuclear mean field potentials[116, 117] which has been developed in parallel with [31, 118]. In that reference, however, a different functional dependence of the mean field on momenta was used. Greco[119] has also recently implemented the momentum-dependent Lattice Hamiltonian with the GBD-type potential discussed in this work. However, the mean field used in that work (c.f. the GBD-type potential in table 3.1 and figure 3.1) does not exhibit the observed saturation of the optical potential at high momenta.

4.2.3 Interpolating Functions

Up to now, we have introduced the Lattice Hamiltonian method via the finite form factor R. However, we have avoided any specific functional form to be used. Simple parameterizations have been used in the past. However, as will be shown, the degree

to which energy and linear momentum are conserved is in general sensitive to this choice. As a starting point, we turn to reference [120]. In this work, a family of *central B splines*[121][5] were studied in the context of smooth particle methods for hydrodynamic simulations[122, 123]. We borrow from that work in an attempt to make a satisfactory selection for our smoothing function.

The central B splines provide for an interpolation from the continuous test particle positions x_i to the grid points whose centres are located at discrete x_α. For a configuration space lattice of spacing δx, the general formula for the n^{th} order central B spline is:

$$(n-1)!M_n(x,\delta x) = \begin{cases} 0. & x \le -\frac{n\delta x}{2} \\ \binom{n}{0}\left(x+\frac{n}{2}\delta x\right)^{n-1}. & -\frac{n\delta x}{2} \le x \le \left(-\frac{n}{2}+1\right)\delta x \\ \binom{n}{0}\left(x+\frac{n}{2}\delta x\right)^{n-1} - \binom{n}{1}\left(x+\left(\frac{n}{2}-1\right)\delta x\right)^{n-1}. & \left(-\frac{n}{2}+1\right)\delta x \le x \le \left(-\frac{n}{2}+2\right)\delta x \\ \vdots & \end{cases}$$

Taking a normalized (c.f. equation (4.8)) M_n for positive x gives us the following one dimensional configuration space form factors which we rename as $\tilde{R}_n$ to emphasize their connection to configuration space:

$$\tilde{R}_2(x_l) = \frac{1}{\delta x^2}\frac{1}{4}(2\delta x - x_l) \qquad 0 \le x_l \le 2\delta x$$

$$\tilde{R}_3(x_l) = \frac{1}{\delta x^3}\begin{cases} \frac{3}{4}\delta x^2 - x_l^2 & 0 \le x_l \le \frac{\delta x}{2} \\ \frac{1}{2}\left(\frac{3}{2}\delta x - x_l\right)^2 & \frac{\delta x}{2} \le x_l \le \frac{3\delta x}{2} \end{cases}$$

$$\tilde{R}_4(x_l) = \frac{1}{\delta x^4}\begin{cases} \frac{2}{3}\delta x^3 - \delta x\, x_l^2 + \frac{x_l^3}{2} & 0 \le x_l \le \delta x \\ \frac{1}{6}(2\delta x - x_l)^3 & \delta x \le x_l \le 2\delta x \end{cases}$$

[5]These are also referred to as the Bernstein Polynomials or Basis splines.

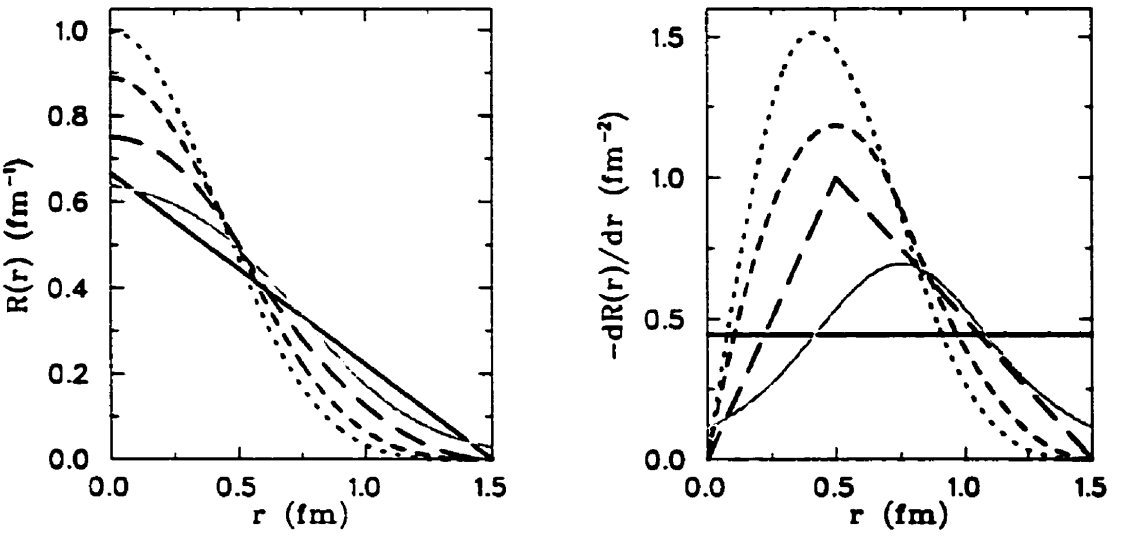

Figure 4.3: Nucleon form factors for several spline forms taken from [120] (dark lines in left panel) and the first derivative of the former (dark lines in right panel). The solid, long-dashed, short-dashed and dotted lines are for R_2, R_3, R_4 and R_5 respectively. Also shown in the two figures is a Woods-Saxon parameterization (shaded lines in both figures) as discussed in the text.

$$\tilde{R}_5(x_l) = \frac{1}{\delta x^5}\begin{cases} \frac{x_l^4}{4} - \frac{5\delta x^2}{8}x_l^2 + \frac{115\delta x^4}{192} & 0 \le x_l \le \frac{\delta x}{2} \\ \frac{55\delta x^4}{96} + \frac{5\delta x^3}{24}x_l - \frac{5\delta x^2}{4}x_l^2 + \frac{5\delta}{6}x_l^3 - \frac{1}{6}x_l^4 & \frac{\delta x}{2} \le x_l \le \frac{3\delta x}{2} \\ \frac{1}{24}\left(\frac{5\delta x}{2} - x_l\right)^4 & \frac{3\delta x}{2} \le x_l \le \frac{5\delta x}{2} \end{cases},$$

where the configuration space form factor in equation (4.7) is given by $R = \tilde{R}_n/N_{ens}$, where the $\tilde{R}_n$ is one of the profiles given above and $x_l = |x_\alpha - x_i|$. We show in the left panel of figure 4.3 the above form factors. For each, the value of δx is adjusted such that all the (spline) form factors have the same range, that is, for x_l >1.5 fm the form factor is zero[6]. In [124], in the context of test-particle BUU simulations for colliding ions, it was shown (using Gaussian form factors) that for a grid spacing

[6]Note that this is slightly larger than the nucleon hard-sphere cutoff of $0.80R_0$ fm used to determine the nuclear radius (c.f. equation (4.2)). This in effect provides for a smooth *nucleon* surface of ~ 0.36 fm.

δx larger than the form factor width, the directed flow depended unphysically on the latter. For grid spacings smaller than the form factor width, this dependence vanished. We thus choose our spline form factors to extend over at least two grid sites in the radial direction. With this constraint, for R_2, R_3, R_4 and R_5, δx is 0.75, 1.00, 0.75 and 0.60 fm respectively. In the same figure, the right panel shows the first derivative for all of the above form factors. Note that this derivative enters directly into the Lattice Hamiltonian equations of motion as seen in equation (4.12). Also in that figure, we show for comparison a Woods-Saxon parameterization for the configuration space form factor. This functional form reads:

$$\tilde{R}_{WS}(x_i) = \frac{\mathcal{N}}{e^{\frac{x_i - x_0}{\Lambda}} + 1}. \tag{4.13}$$

where $\mathcal{N}$, x_0 and Λ are 2/3, 0.75 and 0.25 respectively. Figure 4.3 indicates that the spline form factors drop to zero at $r = 1.5$ fm (as already mentioned, this has been adjusted by hand). In addition, R3, R4 and R5 have a continuous first derivative in that interval. In general, the spline of order n has a continuous derivative of order $n - 2$. We also note for future reference that as the order of the spline increases, so does the area under the first derivative curve. In contrast to the splines, the Wood-Saxon parameterization does not smoothly drop to zero at $r = 1.5$ fm, it does however have a continuous derivative inside the interval $0 < r < 1.5$ fm to all orders. Note that the area under the first derivative curve for this form factor is lower than all of the splines presented here. We will come back to an analysis of these form factors in section 4.4. Before this, however, we will discuss the implementation of the numerical procedure used to solve the Vlasov and BUU equation.

4.3 Numerical Implementation

4.3.1 Mean Field

The last few sections have presented us with all the ingredients necessary to embark on a numerical solution. The procedure we use here is accomplished by introducing a discrete time step δt and solving the lattice Hamiltonian equations using the *Verlet-Velocity* algorithm. This is a variant of the leap-frog method which is often used, however, the former gives us access to the particle positions *and* momenta at equal time intervals[7]. The Verlet-Velocity algorithm in general gives slightly better accuracy than the corresponding leap-frog algorithm. For a full discussion on these methods, the reader is referred to [125]. The discretized equations of motion are calculated as follows:

$$\begin{aligned} \vec{r}(t-\delta t) &= \vec{r}(t) + \delta t\, \vec{v}(t) + \frac{1}{2}\delta t^2 \vec{a}(t) \\ \vec{v}(t+\delta t) &= \vec{v}(t) + \frac{\delta t}{2}\left(\vec{a}(t) + \vec{a}(t+\delta t)\right), \end{aligned}$$

where the forces and velocities are calculated from equation (4.12), the lattice Hamiltonian equations of motion. We note that a fourth order Runge-Kutta integration scheme which involves four velocity (acceleration) terms in the first (second) of the above equations, increases the computation time by at least a factor of 3. For all numerical investigations in this work, we have used $N_{ens} = 100$ and a time step of $\delta t = 0.33$ fm/c, which implies that a given test particle remains within a given lattice site for at least two time steps for all the grid sizes previously given.

4.3.2 Binary nucleon-nucleon collisions

So far, our solution has ignored the Uehling-Uhlenbeck collision term presented in section 2.3. We now re-introduce this term into our numerical procedure. We follow

[7] In general, the leap-frog method allows access to configuration space values at integer time steps ($n\delta t$) and momentum space values at half integer time steps $(n + 1/2)\delta t$.

the work of [21] for elastic collisions only as we are mainly concerned with intermediate energy collisions where elastic scattering dominates over inelastic scattering. In this procedure, only collisions between test-particles that belong to the same ensemble are allowed. This is known as the *ensemble method.* Between time steps, all test particles belonging to a given ensemble are compared. The distance of closest approach[8] is calculated, and if this distance is greater than $\sqrt{\sigma/\pi}$, where σ is the total elastic energy-dependent cross section, then the two test particles cannot scatter. For closest approach distances less than this value, the particles are allowed to scatter elastically. New momenta are then assigned to these particles. Next, the phase space density around both scattered particles is calculated. If this is greater than some prescribed value, then scattering is forbidden and the momenta are reset to pre-collision values. This procedure in effect calculates the Pauli blocking factors that appear in the Uehling-Uhlenbeck collision integral in equation (2.24). This is a known procedure and full details can be found in the reference provided and also in reference [22]. We find that for isolated cold nuclei, collisions are Pauli blocked with an efficiency of ~96%. In addition, for collisions of nuclei at lab kinetic energies of $E_k/A = 50$ MeV/A, collisions with k_{CM} <0.70 fm^{-1} are blocked with an efficiency of 96%. This justifies the 150 mb truncation of the elastic cross section as presented in figure 3.9. Furthermore, we note that we also prevent binary collisions between test particles from the same nucleus unless one of them has already undergone an unblocked collision.

Previously we mentioned that the elastic cross-section requires modification due to the presence of a momentum-dependent term in the nuclear mean field potential. The method we have adopted in this work does differ from those in the literature in that we perform a direct calculation of this modification (presented in section 3.2). In that section, we provided a closed form solution to this modification for equilibrium nuclear matter. In the case of colliding heavy ions, however, we do

[8]Note that knowledge of the position and momentum at time t and $t + \delta t$ are thus required.

expect non-equilibrium[9] processes to be at work. We thus cannot take advantage of the closed form solution for the in-medium modification to the elastic cross section obtained in the aforementioned section. We alternatively have to explicitly calculate the density of final states (and relative velocity) numerically for each test-particle collision process. This involves a *direct calculation* of equation (3.14), where $u(\rho, \vec{p}) = u(\rho_0, |\vec{p}|)$ is in general no longer true. As this is calculated using the nucleon form factors introduced for the lattice Hamiltonian method, it is a considerable numerical task. Careful consideration of storage issues can have drastic improvements in code performance. With our implementation of the self-consistent in-medium cross section run times are typically increased by a modest 15%. Once D_f and v_{rel} have been computed, the new, modified cross section is then calculated and compared with the pre-collision closest approach value. If this value is now larger than what the new cross section allows, then the collision is forbidden and the test particles are reset to their pre-collision momenta. We restate that since the equilibrium configuration is in general no longer present, the in-medium cross section presented in figure 3.8 is no longer valid. However, it is useful for illustrative purposes.

Before moving on, we will summarize the model presented so far. We have implemented a momentum-dependent lattice Hamiltonian solution of the BUU equation for modeling the collision of heavy ions. In particular, the lattice Hamiltonian method is applied to the evolution of the mean fields and as such solves the Vlasov part of the BUU equation. To supplement this, we have introduced a cascade algorithm that takes into account two-body nucleon-nucleon collisions. In-between collisions, the nucleons move on curved trajectories as calculated by the Vlasov part of the BUU equation. In addition, we have implemented a correction to the nucleon-nucleon scattering cross section (used in the BUU implementation) that consistently takes into account the nuclear medium in which the nucleon-nucleon collisions take

[9]With non-equilibrium processes, the momentum distribution of the nucleons will not exhibit spherical symmetry. This is the symmetry that allowed us to write down a closed form solution for the self-consistent in-medium modification to the nucleon-nucleon cross section.

place. This correction is particular to momentum-dependent nuclear mean fields. We now move on to investigate qualitative features of the model presented thus far.

4.3.3 Dynamical Features

We now provide a qualitative examination of our numerical solution by consideration of the configuration space evolution of two colliding ^{197}Au nuclei. We remind the reader that more detailed quantitative investigations with the model we have developed here are to be made in chapters 5 and 6.

In figure 4.4 we show the evolution of the test-particle distribution for three different BUU propagation schemes with the MDYI-type momentum-dependent mean field potential. Isospin and Coulomb effects were included in all simulations. Note that all calculations were performed in the nucleon-nucleon centre of mass frame. For all cases, the incident laboratory bombarding energy[10] (beam direction is the $\hat{z}$ direction) was $E_k/A = 50$ MeV for a normalized impact parameter ($\hat{x}$ direction) of $b/b_{max} = 0.20$. The left, middle and right column is for a collision-less Vlasov propagation, BUU propagation and BUU propagation coupled with the self-consistent in-medium cross section, respectively. Each panel from the top to the bottom is a snapshot of the test-particle distribution projected onto the reaction plane at $\Delta t = 100$ fm/c intervals. The main qualitative differences are seen when we move from the Vlasov to BUU picture. In the former, the two nuclei exhibit large transparency and for the most part pass through each other. Note that for this case, the two nuclei partially orbit each other in an attractive manner. That is, the projectile (initial negative z and positive x in the figure) is deflected to negative x values. When we turn on the nucleon-nucleon collisions in the second column, we see that the transparency present in the Vlasov picture is now lost. In fact, the nucleons from the two nuclei pile up and the large compound quasi-nucleus then emits particles in

[10]This quantity is traditionally defined as the lab frame kinetic energy per projectile nucleon incident on a fixed target.

a more or less isotropic manner. We do note that the projectile in this case is *slightly* deflected to *positive* x values, in contrast to the former case. Finally, for the BUU simulation with the additional self-consistent in-medium effect, we see a compromise between the previous two pictures. That is, the test-particle distribution is more (less) elongated in the $\hat{z}$ direction then that of the BUU (Vlasov) simulation. In addition, we note that the presence of nucleon-nucleon collisions tends to reduce the size of the final state fragments.

We can gain deeper insights into the dynamical differences in the above collisions by examining the evolution of the nucleon *density*. In figure 4.5, we show the reaction plane density corresponding to the test-particle distributions shown in figure 4.4. In this figure, we only consider test-particles within a 1.5 fm thick slice about the reaction plane. First of all we note that at $t = 0$ fm/c, there are some density fluctuations in the nuclei. This effect is due to the finite sampling of phase space. For all simulations, we see that at $t = 100$ fm/c, the compound system is at sub-saturation density levels. As the system expands (predominantly along the beam line direction for the Vlasov simulation), small pockets of low density collect and build up to produce small regions of nucleons at saturation density levels ($t \sim 200$ fm/c). We note that without nucleon-nucleon collisions, these regions are considerably larger. When we turn on the collisions (middle panel), we see (from the test-particle distribution in figure 4.4), that the approximately isotropic emission of nucleons from the centre of mass of the system does not lend itself to produce small clusters. We do note however, the density slices about the reaction plane presented in this figure ignores many free nucleons and clusters that have been emitted out of the reaction plane. Although at this bombarding energy the fraction of these nucleons is small, they are nonetheless present as is easily seen from the clusters present in the test-particle distribution presented in figure 4.4.

To gain a qualitative picture of the *early* reaction dynamics in a nucleus-nucleus collision, we show in figure 4.6 the in-plane density distribution for Au+Au collisions

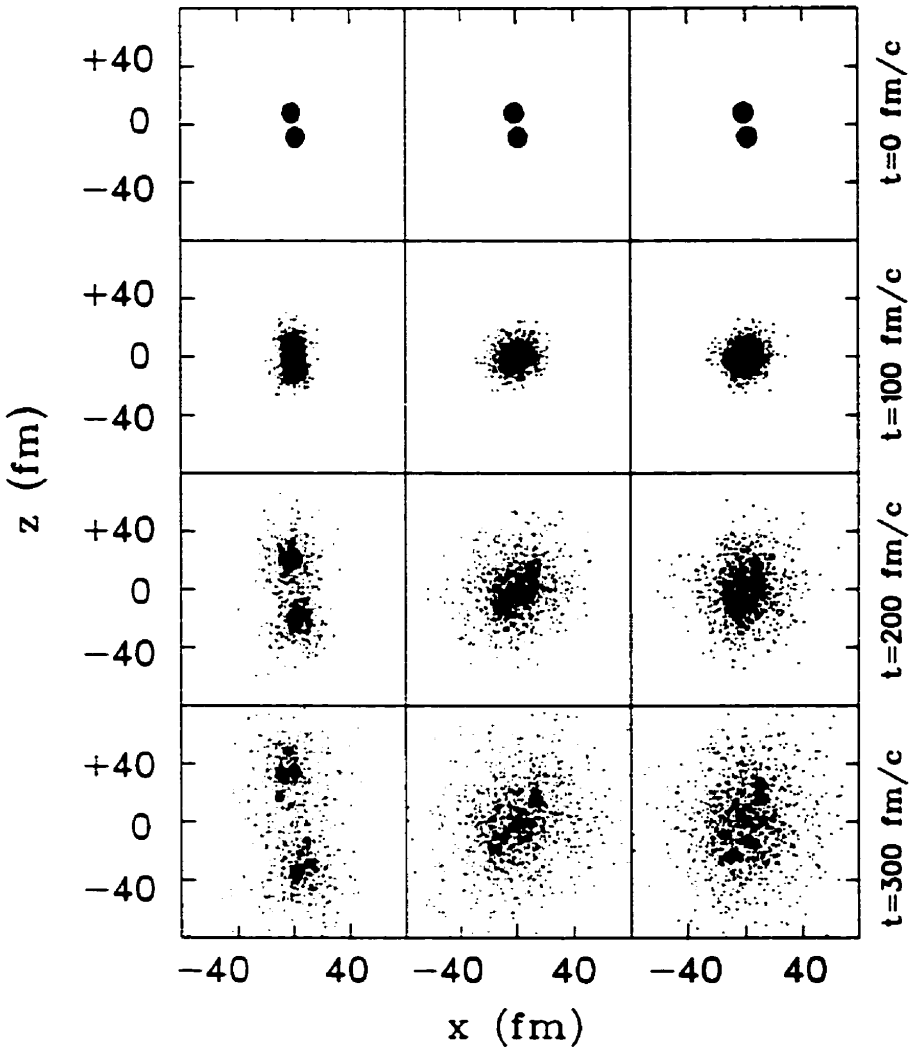

Figure 4.4: Test particle distribution for a simulated Au+Au collision at 50 MeV/A for an impact parameter of $b/b_{max} = 0.20$. The rows represent $\Delta t = 100$ fm/c time slices at 0. 100. 200 and 300 fm/c from top to bottom. The left panels are for a collision-less Vlasov (mean field only) propagation, the middle is for a BUU (mean field plus free space nucleon-nucleon cross section) simulation and the right is for a BUU simulation with the self-consistent in-medium cross section modification. For all cases the MDYI-type momentum-dependent mean field supplemented with Coulomb and Isospin effects was used. We show a representative sample of 5 ensembles.

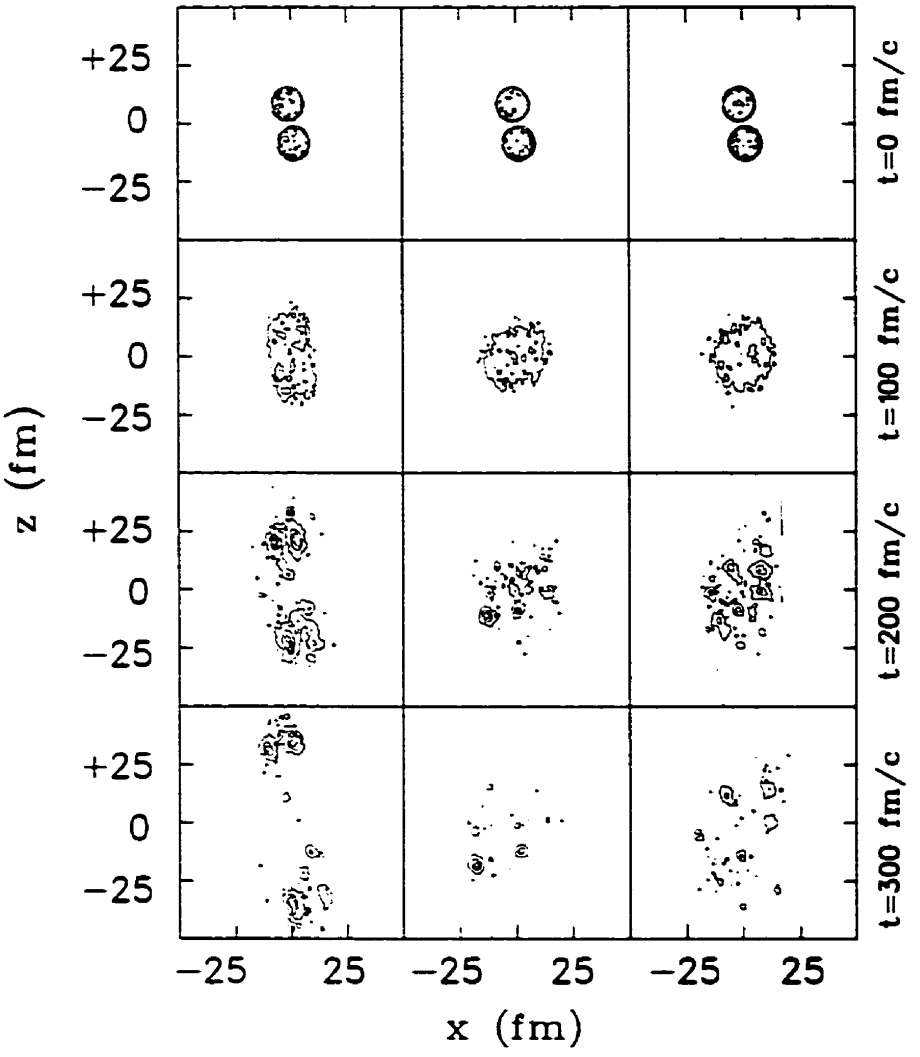

Figure 4.5: In-plane density distribution from Au+Au collisions at 50 MeV/A corresponding to the test particle distribution from figure 4.4. The contours levels are at 0.05. 0.5. 1.0 and 1.5 times the nuclear saturation density ρ_0. Starting from the top. the time slices are 0. 100 ,200 and 300 fm/c.

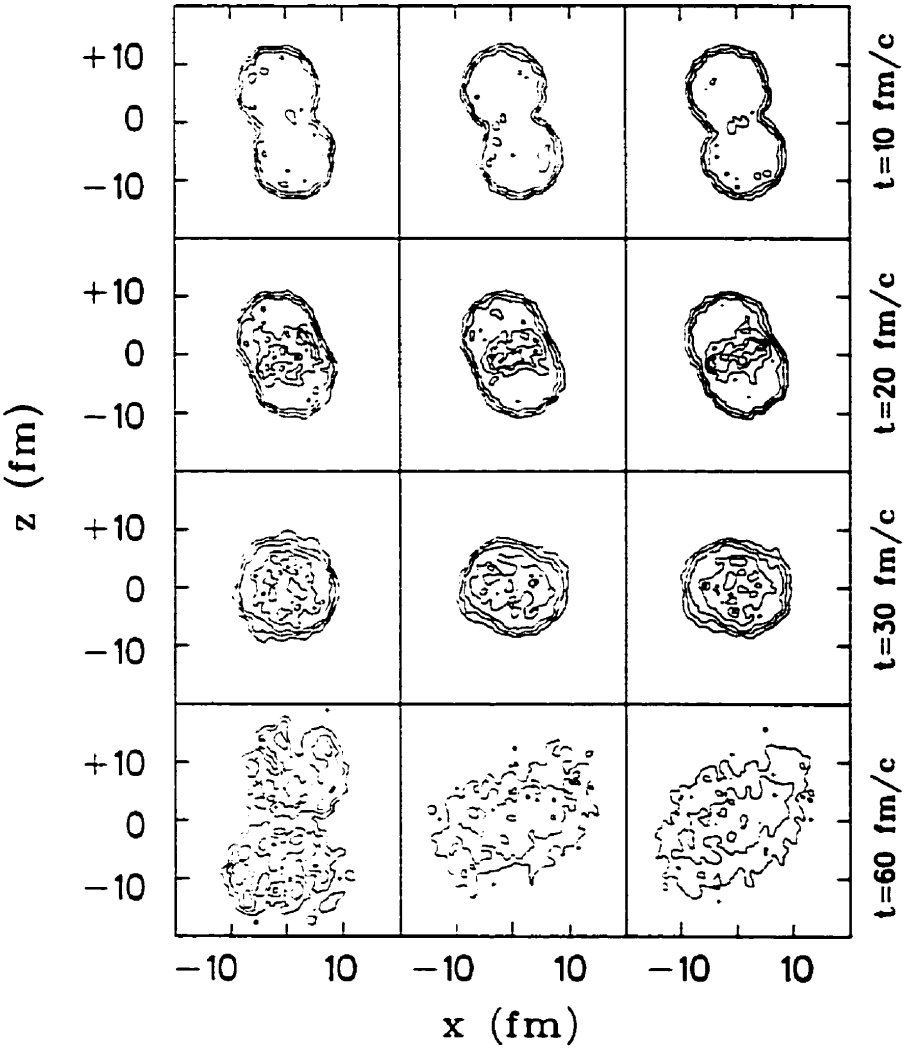

Figure 4.6: In-plane density distribution from Au+Au collisions at 150 MeV/A for time slices of t = 10, 20, 30 and 60 fm/c. For all cases, the contours levels are for 0.1, 0.3, 0.6, 1.1, 1.4 and 1.6 times the nuclear saturation density ρ_0. The columns are as in figure 4.4.

at an incident lab bombarding energy of 150 MeV per nucleon. As this is a higher energy than the last example, the dynamical features we examine here take place on smaller time scales. In this figure, the time slices are now for Δt=10, 20, 30 and 60 fm/c. The columns are as in figure 4.4. The Vlasov propagation scheme (left panels) indicates that the nuclei exhibit large transparency. In fact, at 60 fm/c, the slightly inflated nuclei have almost passed completely through each other. Comparison with the BUU propagation scheme (middle panels) shows that the nuclei are stopped in the centre of mass at early stages and an expansion transverse to the beam direction follows. Furthermore from the figure it is evident that turning on the nucleon-nucleon collisions results in a density overlap region that is higher and more compressed than in the Vlasov case. This is due to early stage nucleon-nucleon collisions which pile up in the overlap region. Again, when we turn on the in-medium cross section (right panels), a compromise between these two scenarios (Vlasov and BUU) is reached.

The dynamical picture presented here has served as a qualitative tool to aid in understanding the gross features of heavy ion collisions with our model. The BUU propagation scheme is more realistic than the Vlasov scheme as evidenced by the effect that nucleon-nucleon collisions have on the dynamics. That is to say, nucleon-nucleon collisions play a sizeable role. Having said this, we then expect the BUU scheme supplemented with the in-medium cross section an even more realistic picture, as it consistently takes into account the momentum-dependent modification to the latter. We will make definite quantitative conclusions on these statements in chapters 5 and 6.

4.3.4 In-medium effects

As seen in the previous section, the in-medium nucleon-nucleon cross section does influence the dynamics of the heavy ion collision. The qualitative pictures presented in that section show that this effect manifests itself in terms of enhanced transparency. This is primarily due to the reduced number of collisions resulting from

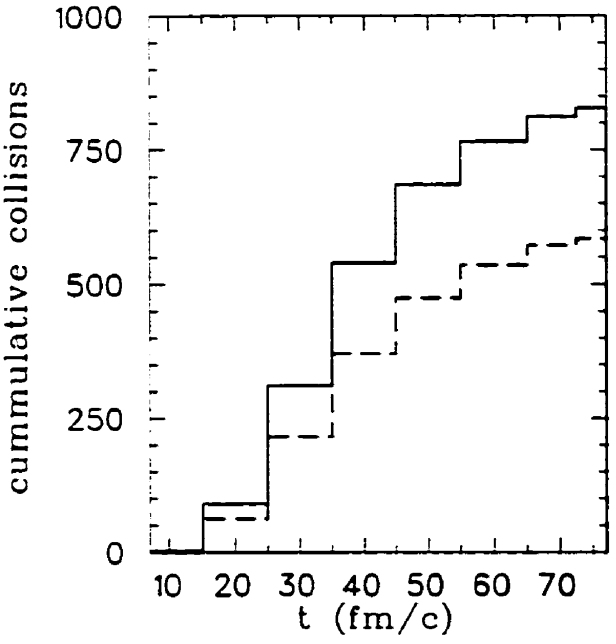

Figure 4.7: Total number of unblocked nucleon-nucleons collisions from simulated Au+Au collisions at 150 MeV/A corresponding to figure 4.6. The solid (dashed) line is for the free-space (self-consistent in-medium) nucleon-nucleon scattering cross section.

the reduced in-medium cross section. In figure 4.7, we show the total number of unblocked collisions from the Au+Au collision presented in figure 4.6. As the figure indicates, the effect of the in-medium cross section does indeed reduce the number of nucleon-nucleon collisions. This effect is most dramatic when the nuclear overlap region is largest ($t \sim 30 \rightarrow 40$ fm/c). Also, as we shall see shortly the effect of the self-consistent modification is strongly momentum-dependent and is largest for low energy (momentum) collisions.

As an example of the dynamical behaviour of this new modified cross section, we show in figure 4.8 the average value of the ratio of the in-medium to free-space cross section for zero impact parameter ^{209}Bi+Bi collisions at laboratory incident bombarding energies of E_k/A = 25, 150, 500 and 1000 MeV. As a comparison, we also show this ratio for the density-dependent in-medium cross section discussed in

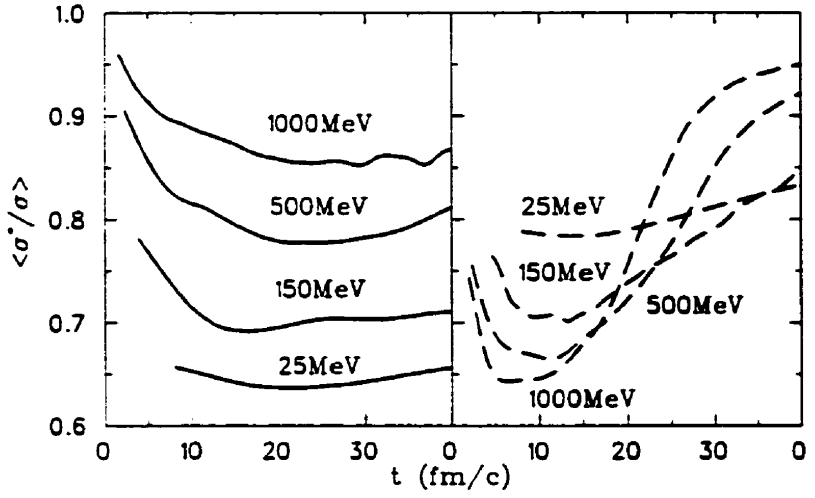

Figure 4.8: Ratio of the in-medium elastic cross section to that of the free space cross section for simulations of collisions of ^{209}Bi+Bi at zero impact parameter for various initial bombarding energies as a function of time. The left panel show the results obtained with the self-consistent method for obtaining the in-medium cross section and the right panel is for a phenomenological density-dependent parameterization of coefficient $\alpha = 0.20$ as described in section 3.2. All simulations were done with the MDYI-type momentum-dependent mean field. Coulomb and isospin effects were not included.

section 3.2. All collisions contributing to this figure are unblocked collisions. There are several characteristics to note from this figure. We first discuss the momentum-dependent self-consistent in-medium modification results in the left panel. For higher bombarding energies, we see that the in-medium cross section is closer to the free space cross section than compared to that at lower energy collisions. This aspect is also reflected early on in the collision process. In this case, thermalization[11] has yet to take place and thus we expect that binary nucleon-nucleon collisions take place at large relative momenta. As the two nuclei coalesce, the initially large separation of the momentum space spheres reduces. The relative momenta and the in-medium cross section will thus lower. This is reflected in the surface plot of figure 3.8 which indicates that we expect a smaller value of the in-medium cross section at low relative momenta. Figure 3.8 also indicates however, that we should expect a lower in-medium cross section for large densities. As we expect a larger density to develop for a higher energy collision, this should manifest itself as a reduction in the in-medium cross section. As figure 4.8 is contrary to this scenario, we conclude that the momentum dependence in the in-medium cross section dominates over the density dependence. The quantitative picture we get from this analysis is that early on in nucleus-nucleus collisions, the in-medium nucleon-nucleon cross section behaves like a free-space cross section, in that the reduction in the former is small. As the nuclei begin to inter-penetrate, the in-medium cross section drops. Thus, initially, the surfaces of the two nuclei are met with resistance from a large nucleon-nucleon collision cross section. This initial resistance drops as the nuclear surfaces begin to inter-penetrate.

Also shown in the right panel of figure 4.8 is the ratio of the in-medium to that of the free space cross section obtained with a density-dependent parameterization of the in-medium cross section given by equation (3.19). This figure shows behaviour

[11] By this we mean that the momentum distribution of the nucleons has not achieved spherical symmetry as not enough nucleon-nucleon collision have taken place yet.

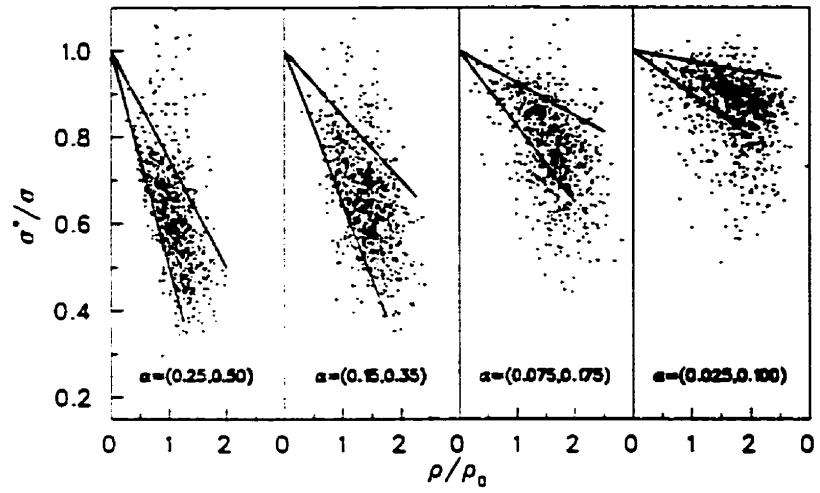

Figure 4.9: Momentum-dependent in-medium elastic cross section coefficient for the time slice $t : 10 \rightarrow 20$. taken from figure 4.8. From left to right. the four panels are for incident bombarding energies of $E_k/A = 25$, 150. 500 and 1000 MeV. The simulations were performed with the MDYI-type mean field potential. and the in-medium nucleon-nucleon elastic cross section calculated as described in the text. In addition. in each panel we show a density-dependent parameterization of equation (3.19) for two values of α as shown in each panel. The abscissa values represent the local density at the collision site.

that is in general opposite to the self-consistent method of calculating the in-medium cross section. That is. at early stages in the nucleus-nucleus collision process. the initially large density buildup results in a low value of the in-medium cross section. Since the higher energy collision produces a larger density. the resulting in-medium cross section is further decreased. These two modifications to the free-space elastic cross section thus show very dissimilar behaviour for a given incident bombarding energy. We investigate the consequences of these differences on linear momentum transfer and elliptic flow in heavy ion reactions in chapters 5 and 6 respectively.

In addition to figure 4.8. we next consider the unblocked collisions in the time slice of $t : 10 \rightarrow 20$ fm/c from figure 4.8. In figure 4.9, we present a scatter plot of the ratio

of the in-medium to the free space nucleon-nucleon cross section for the MDYI mean field potential as a function of density for several incident bombarding energies. The in-medium cross section in this case is calculated self-consistently and the density presented in that figure is the local density at the collision site. This figure indicates that for a given density, the in-medium cross section can take on different values. This is due to the additional momentum-dependence on the latter. Furthermore, in figure 4.9, we also show the value of the in-medium cross section that would be obtained with the density-dependent prescription already mentioned, but for two different values of the coefficient α in equation (3.19). We note that as the values for the in-medium cross section presented in this figure are for a given time slice, that the values of α that bracket these points (for the density-dependent parameterization) are valid only for this time slice. In addition, α must be adjusted for a particular incident bombarding energy. That is, the density-dependent parameterization requires that α vary with both the incident energy and the elapsed time during the nucleus-nucleus collision. In figure 4.8, the value of α for the density-dependent parameterization is fixed at 0.20 for the entire nucleus-nucleus collision, as one cannot know a priori how it should vary during the course of a heavy ion collision. We thus find that the linear dependence on density in equation (3.19) to be a very rough approximation.

We will return to an analysis of these two in-medium cross sections in chapters 5 and 6 where we perform systematic comparisons with experimentally measured signals.

4.4 Energy and Momentum Conservation

We now return to the configuration space form factors introduced in section 4.2.3, and examine their energy and momentum conservation properties. In general, grid-based simulations do not exactly conserve energy and momentum. Instead, one tries to minimize the effects of violating conservation laws, and one selects a solution that

will not too heavily bias results. To this end, we investigate our numerical scheme to test its sensitivity to the configuration space form factor already introduced. First, we examine linear momentum conservation for a single non-interacting nucleus. For this test, we considered a ^{40}Ca nucleus, and neglected Coulomb, isospin and collisional effects. We are thus concerned with only the behaviour of the nuclear part of the potential. As this is by far the largest contribution to the potential energy, our results should be generally reflective of the case with full Coulomb and isospin terms included. All the form factors presented in section 4.2.3 are considered here. The nucleus was initialized as described in section 4.1 and placed on a grid of lattice spacing δx as described in section 4.2.3. An initial kinetic energy boost (in the $\hat{z}$ direction) was then given to the nucleus and it was allowed to traverse a grid of length $\Delta x = 25$ fm. Upon completion of this travel, the final linear momentum $(\vec{p}\cdot\hat{z})_{final}$ of the nucleus was measured and compared to the initial boost momentum $(\vec{p}\cdot\hat{z})_{initial}$. We define the *lattice friction* as the momentum loss per transit time Δt over the distance Δx, that is, $((\vec{p}\cdot\hat{z})_{final} - (\vec{p}\cdot\hat{z})_{initial})/\Delta t$. For a discussion of lattice friction in grid-based simulations, see [125]. Figure 4.10 shows the results thus obtained for initial bombarding energies ranging from $E_k/A : 20 \rightarrow 200$ MeV for both momentum-independent and momentum-dependent mean field potentials. The figure indicates that for all energies, form factors and potentials, lattice friction is present. That is, in all cases, the nuclei have lost linear momentum. The situation is the worst at low energies. The momentum-independent simulation is also more sensitive to lattice friction than is the momentum-dependent simulation[12]. The figure indicates that friction is decreased as we go to higher orders in the spline form factor. As the latter have smoother higher order derivatives *and* differ in the magnitude of the first derivative, there are two possibilities for the decreasing of lattice friction with an increasing order in the (spline) form factor. However, the Woods-Saxon form

[12]Note that due to the effective mass $m^*/m < 1$ for the momentum-dependent potential, nucleons in this mean field will have a larger velocity for a given momentum than those in the momentum-independent mean field.

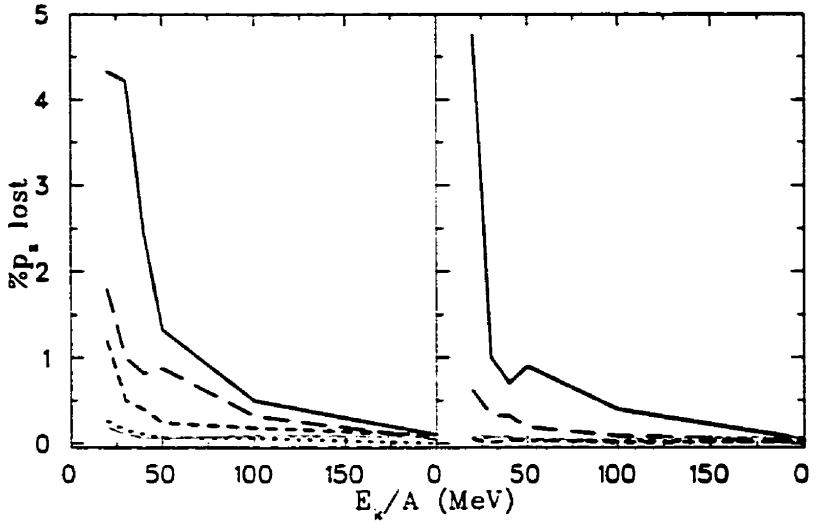

Figure 4.10: Percentage of initial linear momentum lost for a ^{40}Ca nucleus traversing a grid over a distance of $\Delta x = 25$ fm as a function of initial bombarding energy for the form factors used in this work. All curves correspond to those presented in figure 4.3. The solid, long-dashed, short-dashed and dotted lines are for the spline form factors, R_2, R_3, R_4 and R_5 respectively. The shaded curve is the Woods-Saxon form factor. The left panel is for a momentum-independent mean field and the right is for a MDYI-type momentum-dependent mean field.

factor results in momentum-conservation that rivals the best of the splines presented here. Common to these (Woods-Saxon and higher order splines) is smoothness in the high order derivatives. We thus conclude that lattice friction can be reduced with form factors that have high order non-zero smooth derivatives. In reference [120, 122], it was also found that higher order central B splines gave better accuracy in smooth particle hydrodynamics simulations.

Next we turn to energy conservation. For the Ca nuclei examined in the momentum conservation scenario, we now calculate the change in total energy. The lattice friction effect is not present in this analysis, as the total energy is calculated in the rest frame of the nucleus. We show in figure 4.11, the change in total energy

per Δt = 100 fm/c time intervals[13] for the momentum-dependent mean field only. The figure indicates that that as we go to higher order splines, the nucleus gains energy at an increasingly faster rate and is only weakly dependent on the initial kinetic energy. We also note that energy conservation is better for larger nuclei. The Woods-Saxon form factor gives the best energy conservation and the highest order spline gives the worst. Comparison of figure 4.11 with the right panel of figure 4.3, we find that the energy gain increases as the area under the first derivative of the form factor increases. In fact, there is approximately a one-to-one correspondence between the two. Thus, good energy conservation for a momentum-dependent simulation requires that the form factor must be slowly varying over its range. That is, as the maximum slope of a spline increases with its order (c.f. right panel of figure 4.3), so does the energy non-conservation. The Woods-Saxon form factor which has, on average, the most gradual slope provides for the best energy conservation. We note that the energy conservation for momentum-independent potentials was better that 0.200 MeV/A for the Ca nucleus at all energies and for all form factors. For M4 and M5, the energy gain in this case was as low as 0.025 MeV/A at 100 fm/c time intervals. Compared to earlier test-particle realizations of the density-dependent and momentum-dependent mean fields, the energy and momentum conservation we observe here is a substantial improvement[29].

So far, we have investigated linear momentum and energy conservation for single, non-interacting nuclei. However, we are in fact interested in *collisions* of heavy ions. In this scenario, we find that utilization of the Woods-Saxon form factor no longer conserves energy to the accuracy we observe with single non-interacting nuclei. We illustrate this for both the Woods-Saxon and the spline form factors used thus far. Figure 4.12 shows the change in energy as a function of time for an ^{40}Ar+ ^{108}Ag collision at E_k/A = 100 MeV/A. The nuclear potential in this case is momentum-independent. The figure indicates that for colliding nuclei, the splines

[13]The energy increase that we have observed here is approximately linear in time.

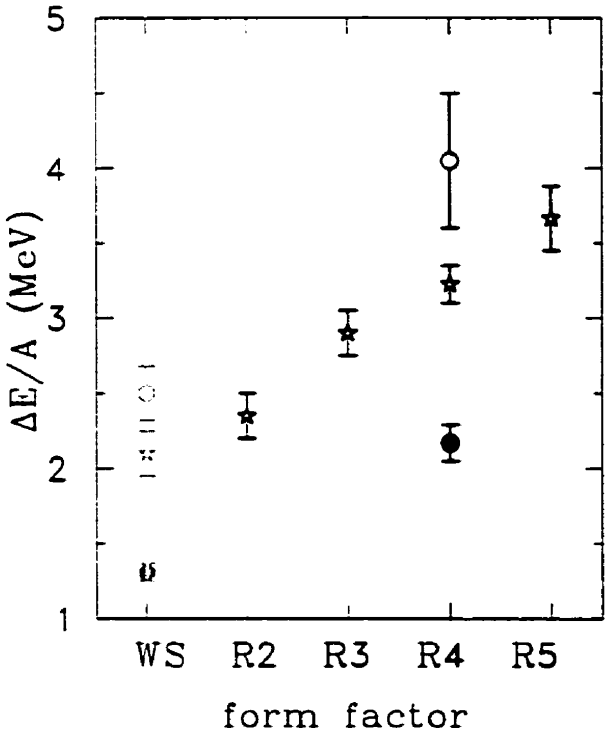

Figure 4.11: Energy gain per $\Delta t = 100$ fm/c intervals for a single nucleus traversing a grid over a distance of $\Delta x = 25$ fm obtained with a MDYI-type momentum-dependent mean field for the form factors presented in figure 4.3. The stars, open and solid circles and are for a ^{40}Ca, ^{20}Ne and ^{208}Pb nucleus respectively. The lower (upper) edge of the error bars is the energy gain obtained for a nucleus with a kinetic energy of 200(20) MeV/A.

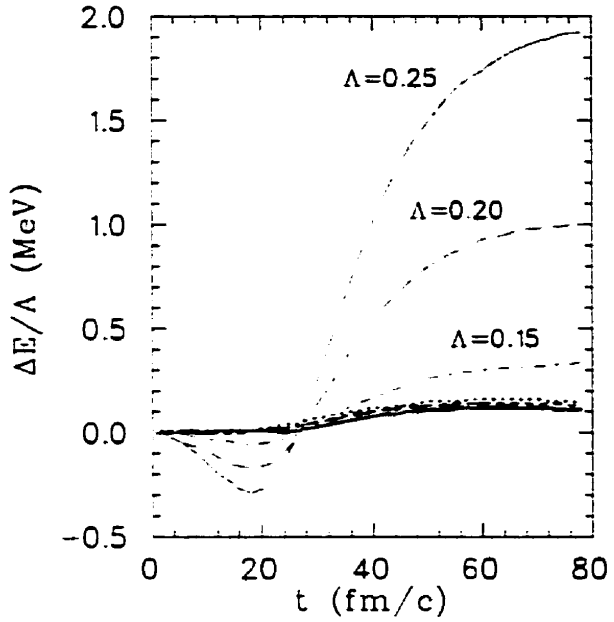

Figure 4.12: Energy change for simulations of collisions of Ar+Ag at $E_k/A = 100$ MeV as a function of time. All dark curves correspond to the splines presented in figure 4.3. The shaded curves correspond to the Woods-Saxon parameterization for various values of Λ as displayed on the plot. The value of $\Lambda = 0.25$ (0.15) has the largest (smallest) discontinuity at its edge.

result in energy conservation far better than the Woods-Saxon parameterization used thus far. In an attempt to understand this behaviour, two other Woods-Saxon parameterizations are used. For these, the parameter Λ has been adjusted to reduce the size of the discontinuity at the form factor edge. We also note that adjusting Λ also changes the maximum slope of the form factor. For all the Woods-Saxon parameterizations used here, the total area under this slope curve is less than that for all spline parameterizations (c.f. figure 4.3). We conclude from this figure, that a form factor which smoothly goes to zero at its edge is crucial for conserving energy in *simulations* of colliding ions.

To summarize, we find that lattice friction can be substantially reduced with a form factor that has continuous derivatives to high orders. This applies to both

momentum-independent and momentum-dependent mean field potentials as presented in figure 4.10. For non-interacting nuclei with the momentum-dependent mean field potential, we find energy is conserved better with a form factor that does not change too rapidly over its range. See for example, the momentum-dependent results displayed in figure 4.11. We repeat that for momentum-independent simulations, energy conservation is better than 0.200 MeV/A for all form factors. Finally, for interacting nuclei, energy conservation improves with a form factor that smoothly drops to zero in a continuous manner at its edge as displayed in figure 4.12 for Ar+Ag collisions. From this analysis, we find that the ideal form factor must be slowly varying with high-orders of continuous derivatives and must also smoothly drop to zero at its boundary.

Chapter 5

Observables and Model Comparisons I

In this chapter we will present the results of our model predictions with several recent experimental observables in the energy regime of $E_k/A \sim \epsilon_f \rightarrow 200$MeV. For the first comparison, we investigate the so-called "flow inversion" for a N+Sm system. This first comparison is used as a test bed for examining qualitative features of our model. For a second comparison we will examine nuclear stopping phenomena in an Ar+Ag system. This observable is closely related to linear momentum transfer and serves to characterize the opacity of nuclei as a function of incident bombarding energy. These two investigations are complementary: the first examines ejecta with projectile-like rapidity produced in low energy peripheral collisions and the second examines large fragments at target-like rapidity for relatively semi-central impact parameters, also at low energies. For the calculations performed in the following chapters we have used nucleon form factors appropriate to the physical problem at hand, including run-time considerations.

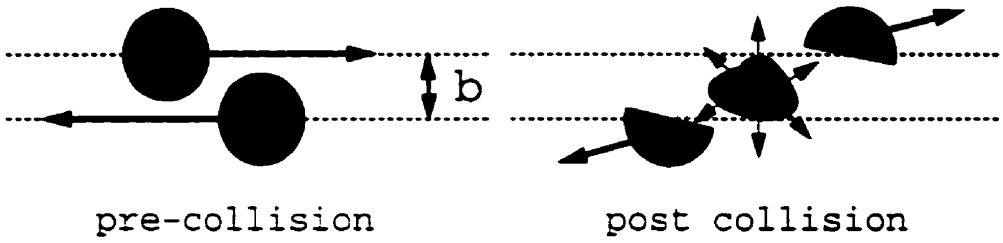

Figure 5.1: Schematic diagram illustrating directed flow in a heavy ion collision. In the initial stage, before the collision on the left hand side, the projectile (entering from the left) approaches the target with a non-zero impact parameter "b". After the collision we are left with a mixed and expanding participant region and two separated pseudo-spectator regions. In this case, the spectators (projectile-like moving toward the right and target-like moving towards the left) are slightly deflected away from the interaction region. In the figure, the $\hat{z}$ axis points to the right and the $\hat{x}$ axis points up: the reaction plane is the plane of the figure.

5.1 Flow Inversion in N+Sm Collisions

As a first comparison, we examine directed flow. This observable gives us insight into large scale collective motion. For example, one can determine in the course of a reaction whether nucleons are (on average) deflected away from, or attracted to the directed overlap region. For a head-on (peripheral) collision, the overlap region is maximal (minimal). Figure 5.1. shows an example where the target and projectile "caps" are slightly deflected *away* from the collision region. In this picture, the directed flow is positive. For attractive scattering, the directed flow is negative. The transition from attractive to repulsive scattering (or vice-versa) in known as "flow inversion".

Recent flow inversion data has been taken at MSU-NSCL [37]. The system

studied there was $^{14}N+^{154}Sm$ at bombarding energies of $E_k/A = 35 \rightarrow 155$ MeV. Traditional flow measurements determine only the magnitude and not the sign of the flow and the inversion is inferred from a local minimum in the flow magnitude [126, 127, 128, 129, 130, 131, 132]. The measurement made in this experiment was of the γ polarization from the electromagnetic decay of the residual Sm target in coincidence with light charged particles. The sign of the polarization measured in conjunction with light charged particles tells us the nature of the nuclear interaction, that is, repulsive or attractive. The mechanism at work here can be easily pictured by considering the schematic diagram shown in figure 5.1. For the system under investigation, the projectile on the left side of the picture is much smaller than the target (beam direction is to the right). After the collision, there is essentially no target spectator cap as the energies employed here are to low for shearing effects[1]. The grazing action of the projectile sets the target spinning, and is thus excited with some angular momentum $\vec{L}$. The excited target residue can then decay electromagnetically. The direction of the angular momentum vector will be a function of the initial geometry, which is not known *a priori* in the experimental set-up. For the diagram presented here however, the angular momentum of the residual excited target nucleus points into the page. For more details, the reader is referred to [37].

The model that we have developed in this work does not permit electromagnetic transitions as this feature has not been incorporated. We can however, observe a flow inversion signal by analysis of the transverse momenta (transverse to the beam) of the final state products. Comparisons between theory and experiment can be made if we note that positive (negative) γ polarization corresponds to negative (positive) transverse momenta for forward moving final state products (this is the sign convention adopted in reference [37]). Note however, that as these two signals (experimental and theoretical) are not the same quantity, the best we can hope for

[1]Such a situation is encountered at high energy where the projectile/target overlap region (participant region) is suddenly disconnected from the original nuclei. The slight rotation of the spectators in figure 5.1 implies that these are really pseudo-spectators.

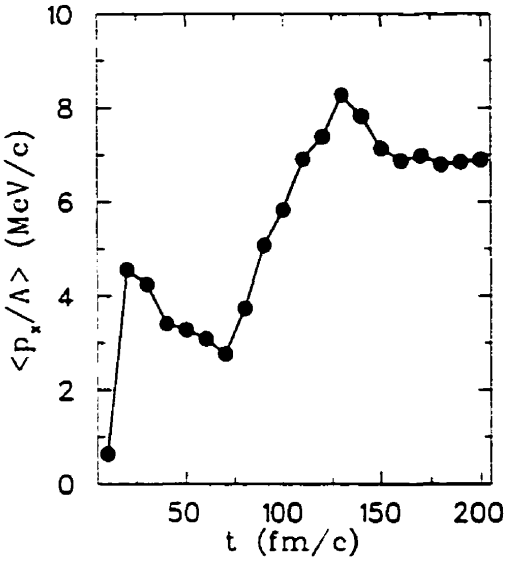

Figure 5.2: Temporal evolution of transverse momentum as a function of time for simulated collisions of N+Sm at $E_k/A = 110$ MeV and $\hat{b} = 0.45$. $< p_x/A >$ is calculated for all nucleons with positive centre of mass rapidity. This result is for the MDYI potential of compressibility 215 MeV.

is a qualitative level of agreement. In order to make a comparison with our model, we required the simulation to run until transverse momenta saturates. Figure 5.2 shows the growth of transverse momentum per nucleon in the forward hemisphere (positive centre of mass rapidity[2]) at $E_k/A = 110$ MeV and $\hat{b} \equiv b/b_{max} = 0.45$. In this figure, saturation is attained at $\sim$ 175 fm/c. In general, this value varies with both incident energy and impact parameter. We made several runs at energies of $E_k/A = 40, 75, 110$ and 150 MeV at impact parameters of $\hat{b} = 0.45$ and 0.90. Our choice of input potential was the MDYI-type momentum-dependent potential of compressibility 215 MeV. Average transverse momenta per nucleon was computed for free and bound protons (excluding the residual target protons) within an angular gate of $25° < \Theta_{lab} < 35°$ in the lab frame as dictated by the experimental acceptances. The results are displayed in the left panel of figure 5.3. The experimentally measured

[2]Rapidity is defined as $y = \frac{1}{2} ln((E + p_z)/(E - p_z))$ and is a measure of the longitudinal velocity.

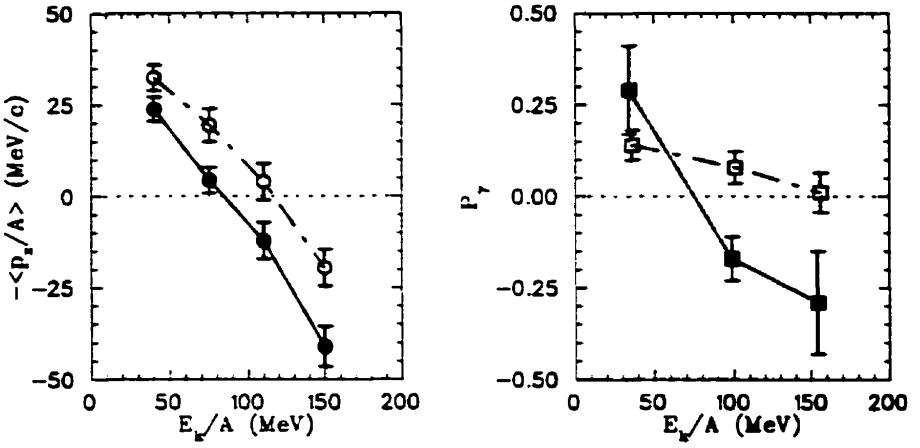

Figure 5.3: Average (negative) transverse momenta per proton for collisions of N+Sm as a function of lab bombarding energy from simulations[116] (left panel) and measured[37] γ polarization in coincidence with ejected α particles (right panel). Open (solid) points are for peripheral (semi-central) impact parameters.

γ polarization for mid-central ($0.2 \leq \hat{b} \leq 0.6$) and peripheral ($\hat{b} > 0.6$) events is displayed in the right panel of the same figure. Experimental impact parameter selection was achieved via measured charged particle multiplicity.

Both the theoretical and experimental results indicate that there is a sign change from negative transverse momenta (positive polarization) to positive transverse momenta (negative polarization) for both impact parameters as the incident energy is increased. This is an indication that the system experiences an attractive mean field at low energies which becomes repulsive as we increase the bombarding energy. In other words, there is a flow inversion. The energy at which the flow changes sign has traditionally been called the "balance energy". Furthermore the results indicate that the balance energy increases with impact parameter. That the balance energy increases with impact parameter has been observed throughout the literature on both experimental and theoretical fronts [111, 133, 134, 135, 136, 137].

For an explanation of the numerical results, we will first consider the mid-central impact parameter and then the peripheral impact parameter. Let us now focus on

the former. The balance energy here is $E_b \sim 85$ MeV. The simulations indicate that that the final state for all energies studied in this work consisted of one heavy excited (target) residue and a spray of isolated nucleons. Below (above) E_b the protons had an average negative (positive) transverse momenta. If we make some consideration of the dynamics involved in the collision process, an understanding of processes at work will surface. As the two nuclei begin to inter-penetrate, there is a density build-up in the overlap region. In the complete absence of collisions (nucleon-nucleon) and mean field effects, this density will be twice the nuclear saturation density. Dynamical effects arising from the inclusion of the mean field typically reduce this value to approximately $1.2 - 1.6$ times the saturation density. The presence of collisions can also alter the density. If we allow the nucleons to scatter off one another during the inter-penetration stage, the (approximately) straight line trajectories of the nucleons will be lost as the nucleons bounce around off one another. This creates a density build-up that will be larger than in the absence of collisions as late coming nucleons run into this stochastic region and pile up[3] (see the $t = 20$ fm/c time slice in figure 4.6 for example). In addition, depending on the initial projectile energy, the number of collisions will vary. At low energy, the Pauli exclusion principle suppresses many nucleon-nucleon collisions as phase space is relatively dense. However, as the energy is increased, scattering above the Fermi surface is more abundant. This in effect produces gaps in phase space which in turn permit more collisions to occur. This will cause the density in the overlap region to build up even more. We find that increasing the energy from 40 to 75 MeV increases the net number of collisions by a factor of about 2 early on in the collision. Partially owing to the increased frequency of collisions, we then expect the overlap density to also be increased. We find that there is about a 5% increase in the maximum density when the bombarding energy is increased from 40 to 75 MeV.

[3]For a collision-less region of nuclear matter, the nucleons move such that they satisfy the Liouville equation, i.e. the density of phase space is kept constant. As mentioned in chapter 2, the inclusion of collisions can modify the latter.

With these two mechanisms at work, let's consider collisions below the balance energy. Here, nucleon-nucleon collisions are limited. The density build-up in the overlap region effectively raises the potential well (the potential well becomes shallower) the nucleons experience and they slowly evacuate this region in favour of the regions near saturation density. The spatially growing overlap region exits the far side of the target as a slow moving, weakly bound dilute blob that is slightly attracted to the potential well of the target upon exit and is thus scattered to negative angles. Slow disassembly of the blob then takes place and we are left with a mist of nucleons that has an average negative transverse momenta. In addition, a substantial fraction of the slowly moving projectile nucleons become trapped in the potential well of the target.

The situation above the balance energy is different. In this case, the increased frequency of nucleon-nucleon collisions effectively creates an overlap density in excess of that which occurs below the balance energy. This causes the nucleons to evacuate this region attaining larger momenta than in the low energy case[4]. We find that this extra momentum is sufficient to cause nucleons to exit at the top of the system (top as in figure 5.1. in the reaction plane), carrying with them a fraction of their initial forward momentum that has not yet been absorbed by the target. These nucleons escape as free particles to positive scattering angles. Nucleons that exit the overlap region into the target are re-scattered and eventually meld with residual target. Thus, the transverse momentum changes from negative to positive values as the bombarding energy is increased. In addition, the larger incident projectile energy allows for a fraction of the energetic projectile nucleons to punch through the target.

The dynamics of the peripheral collision are different. Nucleon-nucleon collisions do not play a large role here. We find that for the peripheral impact parameter at 75 MeV, the number of nucleon-nucleon collisions drops by a factor of about 5 as

[4]The potential gradient is steeper than in the low energy case.

compared to the mid-central collision. For this collision, the impact parameter is near maximal and the overlap region is that of two nuclear skins, both of which are at sub-saturation levels (c.f. figure 4.2). Thus, the overlap produces a density that is not far removed from that of saturation density. This results in the formation of a bridge through which the nuclei can exchange nucleons and feel a net attractive force towards one another[5]. As the projectile moves past the target, the system partially orbits and the projectile is eventually released and scatters to small angles. As the projectile releases from the target, a few nucleons are kicked up as they try to decide which nucleus to join and are left behind, streaming into vacuum. For higher energies, the region that these nucleons are kicked up in is shifted up and to the left (see right hand side of figure 5.1) and are thus scattered into transverse momenta states that are more positive than in the low energy case.[6] The scenario presented here implies that the final state consists of *two* excited remnants: the target and projectile residue. This is in contrast to the mid-central collision. In fact, we find that for all energies studied here at large impact parameter, there is a projectile remnant which is scattered to small angles.

Finally, we note that the measurement we have made here is an *inclusive* one. That is to say, except for the angular acceptance imposed by the experimental setup, all other variables such as rapidity and azimuthal angle have been integrated over. We have thus potentially hid information that may provide us with deeper insights into the dynamics of the collision. We present figure 5.4, as an example of this. Here we see that the transverse momenta as a function of rapidity is non-trivial, and there are effects that are washed out if we sum over all rapidity as we have done in figure 5.3. In particular for the peripheral collision, we note that $< p_x/A >$

[5]At energies of $\sim 5 \rightarrow 10$ MeV/A above the Coulomb barrier this bridge can exist for long times (> 5000 fm/c) as the quasi-compound nucleus goes through several rotations.

[6]The larger angular momentum present in this system causes the orbit to be less tightly bound than in the lower energy case, thus the projectile releases itself from the target at an earlier stage in its trajectory.

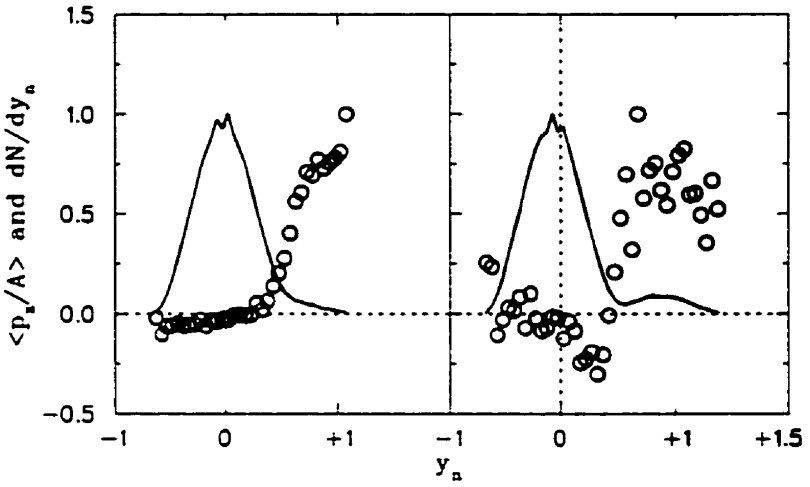

Figure 5.4: N+Sm differential flow for $\hat{b} = 0.45$ (left panel) and $\hat{b} = 0.90$ (right panel) at a lab bombarding energy of $E_k/A = 110$ MeV. $< p_x/A >$ (points) is shown for all nucleons. The solid curves in both figures give the number of nucleons per unity rapidity. Rapidity is shown in the lab frame and is normalized to the beam rapidity. The scale on the y-axis for the rapidity curve only is arbitrary. The difference in scatter in the two plots is due to statistics.

changes sign, going from negative at mid-rapidity to positive at near projectile-rapidity. In fact, the traditional method of extracting the flow signal is to plot transverse momenta as a function of rapidity as is done in figure 5.4 and take the slope at mid-rapidity[138, 139, 140]. However, our analysis has shown, at least on a qualitative level, that our model reproduces so far the observed flow inversion as well as the impact parameter dependence of the balance energy. In chapter 6 we address an observable that has a non-trivial dependence on the azimuthal angle ϕ. The investigation in that chapter is thus a differential flow analysis and provides for a finer level of resolution into the nuclear dynamics.

5.2 Nuclear Stopping in Ar+Ag Collisions

For out next comparison, we turn towards some splintering results taken at the MSU-NSCL cyclotron[141]. Here, beams of ^{40}Ar impinging on a ^{108}Ag target at laboratory bombarding energies ranging from $E_k/A = 8 \rightarrow 115$ MeV were produced.

Before we begin, it will be instructive to first consider the dynamics involved in such processes. As the energy region probed in this analysis is similar to that investigated in section 5.1, we can borrow from the ideas presented there to get an overall picture of the physics involved in this situation. Since we are concerned with mid-central impact parameters, we encounter a scenario similar to that encountered in the N+Sm system at an impact parameter of $\hat{b} = 0.45$. However, as the system asymmetry is smaller here, subtle differences will arise. In fact, for the N+Sm system (mid-central impact parameter) the ratio of the volume overlap to that of the target volume was about 0.1. For the Ar+Ag system studied in this section, this ratio is about 3.7 times greater. Thus, as the nuclei have inter-penetrated one another, the region in which the nuclear potential well depth is reduced is a sizeable fraction of the total target volume. As previously explained, the super-saturated density in this region causes nucleons to evacuate to regions where the density is near saturation.

As in the N+Sm case, at low energy, this evacuation is slow and the overlap region gradually inflates, spilling particles and their associated projectile-like momenta both into vacuum as well as into the lower portion of the target. This results in a relatively large target residue and a large loosely bound nuclear matter blob released from the target. The decay channel for the emitted blob consists of a few light clusters and many light particles. As the energy is increased, these decay channels shift towards lower masses and thus produce more light particles and more light clusters with smaller masses. That is, more nucleons are liberated from the mean field. The residual target in the case of higher energy collisions becomes populated with higher energy refugees from the overlap region and is thus excited to higher energy states. This results in decay channels similar to that in the participant. However, the shift to lower mass channels occurs at higher incident energy as the majority of the initial projectile energy is deposited into the target outside of this (target residue) region[7]. So the overall picture is that of a large excited target residue with a few clusters and many light particles at low energy, to a smaller excited target residue, smaller and more numerous light clusters and more light particles at higher energies. For lower energies, the small number of ejected nucleons and clusters carry with them only a small portion of the initial momenta, thus the target inherits a large portion of the initial projectile momentum. For higher energies, a large fraction of the initial projectile momentum is carried off by the more numerous light particles ejected from the interaction region as the potential well there is no longer deep enough to keep particles inside. Note that the larger kinetic energy of the target implies that nucleons in the overlap region will on average have a larger kinetic energy. Thus, the heaviest remnant in this case inherits less momentum from the initial projectile.

To illustrate this process, we show in the left panel of figure 5.5 the total mass number bound in the residual target, other clusters and free nucleons from simula-

[7]The *residual* target is, in general, in a lower energy excitation state than that of the overlap region.

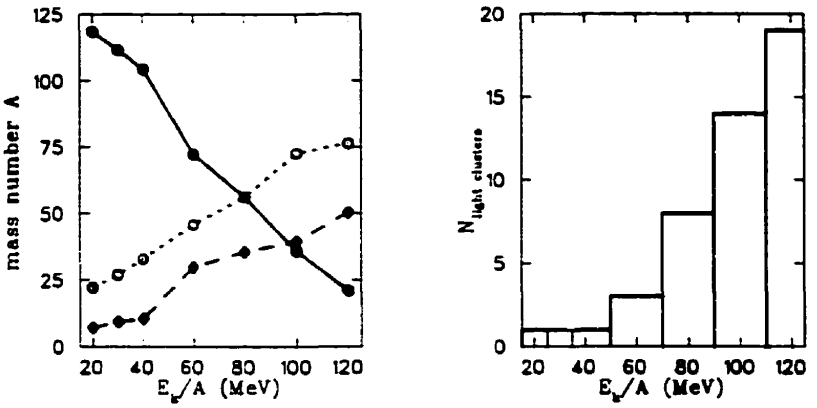

Figure 5.5: Distribution of masses from Ar+Ag collisions at incident lab energies ranging from $E_k/A = 30 \rightarrow 120$ MeV. In the left panel we show the number of nucleons present in the largest final state residue (solid circles), the total number of nucleons bound in clusters smaller than the largest final state residue (solid diamonds) and the total number of free nucleons (open circles). In the right panel, we show the total number of clusters smaller than the largest remnant.

tions of Ar+Ag collisions with a momentum-independent mean field of compressibility 380 MeV at an impact parameter of $\hat{b} = 0.20$. We define our clusters at the end of the simulation. For each test particle, we transformed to the centre of momentum of its local configuration space cell. The total energy (single particle potential plus kinetic) of the particle is calculated in this frame. In this way, we define a particle to be free if its total energy in this frame is positive. Otherwise, it is considered to be a bound particle. Next, we need to isolate the fragments. In order to do this, we performed a search on the three-dimensional configuration space grid to locate the density centroid of groups of test particles that were clustered together. Once this centroid was located, we selected concentric spherical shells about this point and calculated the shell density, where only bound test particles contribute. Once this shell density drops below a critical value (we used $\rho/\rho_0 = 0.05$, however, we found little sensitivity to this value for $\rho/\rho_0 < 0.15$) we stop counting particles. Any bound

test particles inside this sphere are considered to be part of the cluster.

From figure 5.5, it is evident that the largest (smallest) mass for the large residue is obtained for the lowest (highest) energy as described in the previous paragraph. In addition, the number of free nucleons increases with energy. For all others (these are nucleons bound in clusters where the cluster mass is smaller than the heaviest residue), it appears as though the cluster mass increases as a function of energy. Presented this way, the figure is a bit misleading as it does not account for the *number* of small clusters in the final state. For this reason, we show in the right panel of figure 5.5 the number of small clusters produced as a function of energy. We see that as the total mass bound in clusters increases, so does the number of clusters. For $E_k/A = 20$, 30 and 40 MeV, we find one small cluster of approximately 7.5, 9.5 and 10.5 mass number respectively. For higher energies, we see more clusters. It would be incorrect to divide the total mass of nucleons bound in clusters by the number of clusters here, since they are not all of equal mass. However, on average, we see that as the number of small clusters increases, the mass per cluster decreases. This is just what we have described in the previous paragraph. We note that the qualitative features presented in figure 5.5 do not change appreciably when we use a soft and/or momentum-dependent mean field. For a discussion of the mechanisms encountered here, the reader is directed to the references[34, 35, 36], which describe splintering behaviour from an experimental point of view.

We now turn towards some recent experimental MSU-NSCL results from the Ar+Ag system[141]. We will concern ourselves with the semi-central impact parameters examined in that work. The measurement made was of the longitudinal velocity of the heaviest final state remnant. In order to compare with our simulations, we required run times to extend until this observable saturated. In figure 5.6 we show the evolution of the final longitudinal velocity of the heaviest remnant as a function of time for a momentum-independent and a momentum-dependent mean field potential. In that figure, the initial laboratory energy was $E_k/A = 60$ MeV

and the impact parameter was $\hat{b} = 0.33$. We see that saturation is obtained at $t \sim 275$ fm/c. In general, this number varies with both incident energy and impact parameter. To test the sensitivity to the mean field and in-medium cross section of the observables investigated in this work, we also made several runs for both soft (K =200 MeV and K =215 MeV for momentum-independent and momentum-dependent mean fields respectively) and stiff (K =380 MeV and K =373 MeV for momentum-independent and momentum-dependent mean fields respectively) mean field potentials as well as free space and in-medium cross sections. For the latter, we employed the self-consistent method for the momentum-dependent mean field and a density-dependent reduction in equation (3.19) with scaling factor $\alpha = 0.33$ as described in chapter 3. For the experimental data, impact parameter selection was achieved through event classification according to measured charged particle multiplicity (a relatively large (small) multiplicity implies a relatively small (large) impact parameter). This selection criterion produced an impact parameter of $\hat{b} = 0.25$. In an attempt to bracket the data, we ran the simulations at impact parameters of $\hat{b} = 0.20$ and $\hat{b} = 0.33$. In figure 5.7, we show the value of the mass of the heaviest remnant that we obtained from or simulations compared to the experimentally measured values. We find satisfactory agreement with the data. The stopping results from both the data and the calculations are shown in figures 5.8 and 5.9. Note that the larger error bars obtained with the GBD-type potential for the more central impact parameter (see middle panels in figure 5.8) are due to poor mass resolution for the heaviest remnant. This aspect was not present with the MDYI-type potential. The large error bars present in the MDYI calculation are statistical in origin.

The results presented here indicate that the final longitudinal velocity of the heaviest remnant is sensitive to the nuclear matter compressibility only for the momentum-independent mean field (c.f. figures 5.8 *and* 5.9). There is only a very weak sensitivity to the compressibility for the MDYI-type momentum-dependent

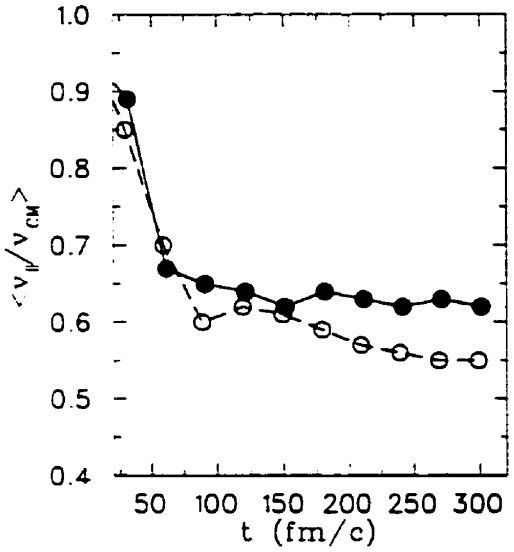

Figure 5.6: Temporal evolution of the largest remnant longitudinal velocity for simulated Ar+Ag at an energy of $E_k/A = 60$ MeV and impact parameter of $\hat{b} = 0.33$. The open (solid) points are for a soft momentum-independent (dependent) simulation. In this case, $t_{lim} \sim 275$ fm/c.

mean field.[8] Furthermore, we note that the inclusion of the (reduced) in-medium cross section results in a reduced value of the final longitudinal velocity. That is to say, the nuclei exhibit enhanced transparency with a reduced cross section (i.e. the coupling between the projectile and target is weaker). This effect is more pronounced for the momentum-dependent in-medium cross section than for that of the momentum-independent one as well as for the more central impact parameter.

On the quantitative side, the stiff parameterization of the momentum-independent mean field indicates that the simulations provide too much stopping for the free space cross sections and just bracket the data at high energy for the in-medium cross section. The soft momentum-independent mean field result brackets the data at higher energies and just overshoots the data at low energies. For the GBD momentum-

[8] A simple explanation for this behaviour is that the momentum-independent mean field depends only on density, whereas the momentum-dependent mean field delegates the potential field to both the density and the local momenta.

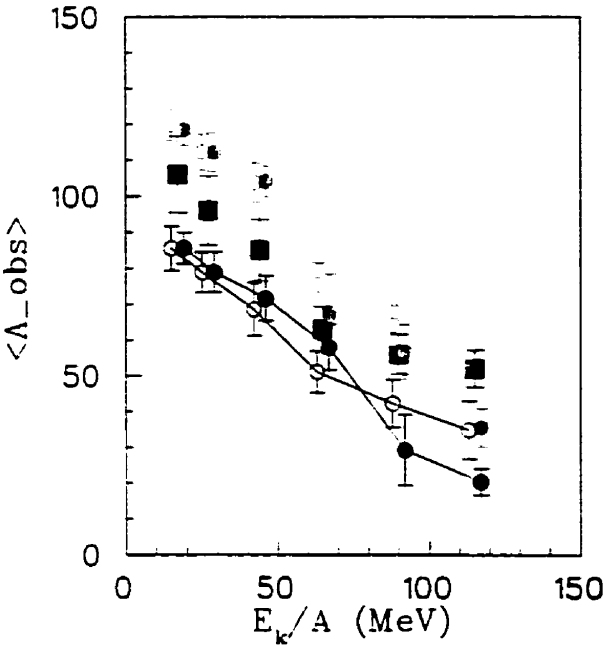

Figure 5.7: Mass of the heaviest remnant from experiment and simulations as a function of incident laboratory energy for Ar+Ag collisions. The squares are the experimental measurements[141]. and all circles are the results obtained from the simulations[117]. Fragment selection is as described in the text. The solid circles are for an impact parameter of $\hat{b} = 0.20$ and the open circles are for an impact parameter of $\hat{b} = 0.33$. The dark circles are for the MDYI momentum-dependent mean field of compressibility $K = 215$MeV and the shaded points are for a momentum-independent mean field of compressibility $K = 380$MeV.

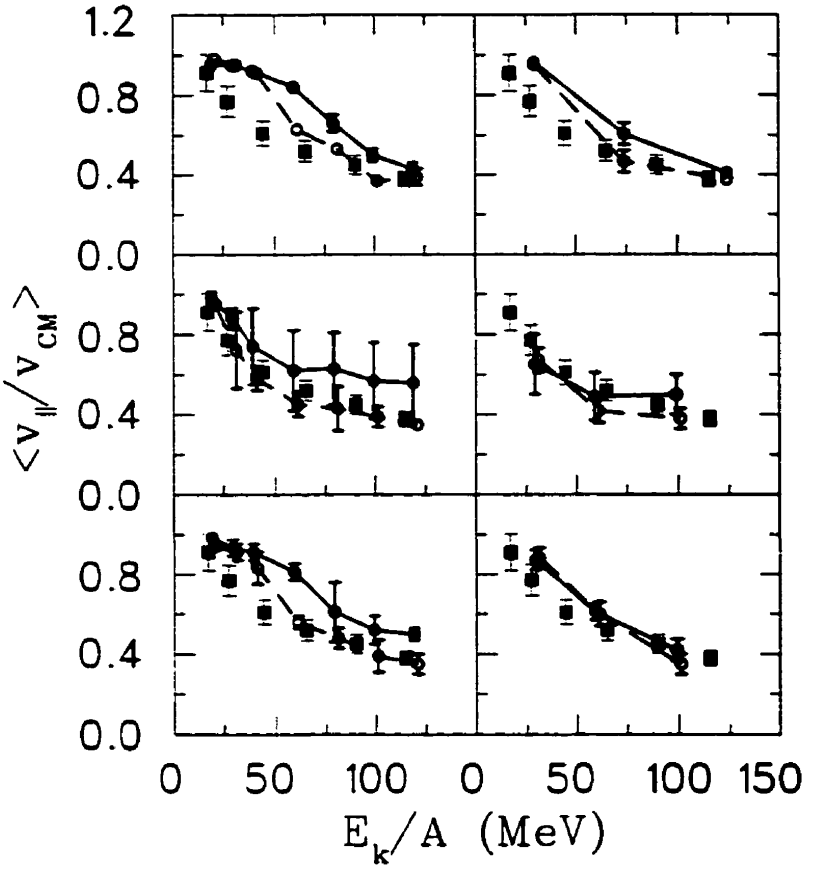

Figure 5.8: Fractional longitudinal laboratory frame velocity of the heaviest post-collision remnant as a function of laboratory bombarding energy. The experimental[141] results are shown by solid squares and are the same in every panel. The simulation results[117] are shown with open (solid) circles for an impact parameter of $\hat{b} = 0.33$ ($\hat{b} = 0.20$). The top two panels are for a stiff momentum-independent Skyrme interaction of compressibility $K = 380$ MeV. The middle (bottom) panels are for a soft GBD (MDYI)-type momentum-dependent mean field of compressibility $K = 215$ MeV. All left panels are for free space nucleon-nucleon cross sections and all right panels are for an in-medium cross section. The in-medium cross section for the momentum-independent mean field is obtained through a phenomenological density-dependent reduction with a scaling factor of $\alpha = 0.33$. The momentum-dependent in-medium cross sections are calculated self-consistently as described in chapter 3.

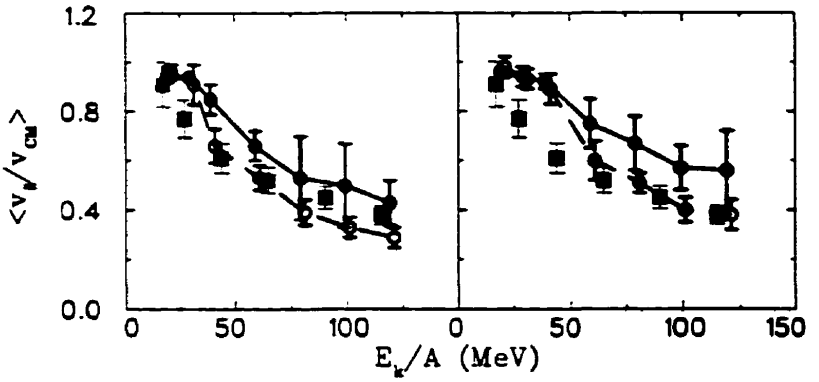

Figure 5.9: Same as figure 5.8 but for a soft momentum-independent mean field of compressibility $K = 200$ MeV (left panel) and a stiff ($K = 373$ MeV) momentum-dependent mean field of the MDYI-type. All results are shown for a free space nucleon-nucleon cross section.

dependent mean field. we note the the data are just bracketed from above (below) for a free-space (in-medium) nucleon-nucleon cross section. The MDYI-type potential overshoots the data at low energy. The larger impact parameter matches the data at high energy. Inclusion of the in-medium cross section in this case produces results that agree fairly well with the data. We find that the soft MDYI momentum-dependent mean field gives slightly better agreement with the data than the stiff one. In general. we find fairly good agreement with the data for a soft equation of state (compressibility of $K = 200$ MeV for momentum-independent and $K = 215$ MeV for momentum-dependent parameterizations of the mean field). with only subtle differences between the momentum-independent and momentum-dependent mean fields. For both momentum-dependent parameterizations however, we have slightly better agreement with the data when we incorporate the in-medium cross section. Inclusion of the in-medium cross section for the momentum-independent mean field produces only subtle changes in the results.

These results favour a soft equation of state as well as an in-medium cross section as calculated self-consistently for the momentum-dependent mean fields. In passing. we note that a calculation similar to the one presented here has been done

in reference[142]. In that work, the momentum-dependent mean field was introduced by means of the Gogny-type force[78] which uses a sum of two Gaussians for the momentum-dependent term. A free-space nucleon-nucleon cross section was used in that work and thus effects due to the in-medium cross section are lacking. We find similar behaviour for the momentum-independent mean field as far as compressibility is concerned. For the momentum-dependent mean field however, we find less sensitivity to the nuclear matter compressibility.

Chapter 6

Observables and Model Comparisons II

In this chapter we will present the results of our model comparisons with several recent experimental observables at energies higher than those examined in the previous chapter. The analysis presented here is more detailed than that of the previous chapter in that it is a differential analysis. We consider collisions of Bi+Bi and probe the high energy ($E_{kin}/A \sim 200 \rightarrow 1000$ MeV) region to investigate the validity of our model.

6.1 Elliptic Flow in Bi+Bi Collisions

Recall in section 5.1 we investigated flow inversion in the N+Sm system. This was actually an example of what is known as *in-plane* flow. In that case, for the larger impact parameter, the projectile was deflected around the target to negative (positive) scattering angles below (above) the balance energy. In addition, the motion of the projectile was predominantly in-plane. That is to say, the projectile remained for the most part in the reaction plane. The dynamics studied at those energies do not in fact translate directly to higher energies. In this case, the situation is

changed as larger forces (due to compressional energies for example) can produce out of plane emission in addition to in-plane emission[33, 143]. The term adopted in the literature for out-of plane emission is "squeeze-out", as the name suggests. The azimuthal distribution (about the reaction plane) of emitted nucleons serves to illustrate this phenomena[144, 145, 146, 147]. Typically, the quantity that is discussed is the ratio of out-of-plane to that of in-plane emission. From here-on, we will refer to this ratio as the anisotropy ratio. Studies on its behaviour indicate that it is greater than unity for beam energies above $\sim$ 100 MeV/A, and peaks at $\sim$ 400 MeV/A. It remains larger than one until beam energies of $\sim$ 5 GeV/A are reached[148]. Numerical simulations have shown that this turnover back to in-plane-flow is largely a function of the geometry of the participant region[146, 149]. For a study of the behaviour of flow phenomena in this energy range, the reader is directed to the paper by Ollitrault[150]. As an aside, we note that since higher energies (compared to that studied in sections 5.1 and 5.2) are required to probe out-of-plane flow, this observable provides a good testing bed for our momentum-dependent in-medium cross section as the latter approaches the free-space cross section as energy is increased. Furthermore, as the self-consistent and density-dependent parameterizations differ substantially at higher energies (c.f. figure 4.8), this energy regime is well suited to study the dynamical differences between the two parameterizations.

A schematic diagram will be helpful in gaining a qualitative understanding of the anisotropy we are concerned with here. Figure 6.1 presents us with a picture of (one of) the mechanisms at work in producing squeeze-out. Recall in section 5.2, we alluded to the density build up in the nucleus-nucleus interaction zone. In that picture, the density buildup was responsible for eventual particle emission. The same idea holds here, except we are dealing with higher energies (200$\rightarrow$1000 MeV/A). As this excited (overlap) region expands it encounters spectator matter which is predominantly located in the reaction plane. Thus the in-plane expansion (*at mid-*

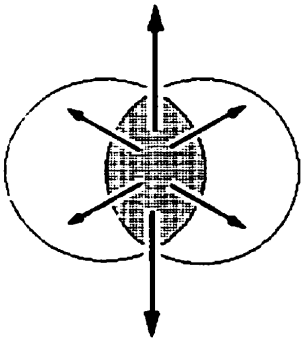

Figure 6.1: Schematic diagram illustrating squeeze-out for the collision of two mass symmetric nuclei. The plane of the figure is the $\hat{x}\hat{y}$ plane. The beam axis points into or out of the page. The shaded region is the nuclear overlap region with a density greater than that of saturation. The arrows indicate the direction of expansion of the excited matter.

rapidity) is suppressed due to "shadowing"[1]. Expansion out of plane however is not hampered by the presence of matter. The net effect is a preferred squeeze out of matter out of the reaction plane. As time passes during the collision, the spectators eventually pass by one another and the participant matter (partially de-excited overlap region) is then free to expand in all directions. Thus, the preferred out of plane emission is favoured *early* on in the collision, and is thus sensitive to non-equilibrium effects which we present early on in the collision. In addition, nucleons which are emitted at earlier stages in the collision should contain pre-equilibrium signatures. The latter can manifest themselves in terms of high momenta nucleons which have yet to be significantly slowed by the mean field and intra-nuclear nucleon-nucleon collisions. This results in a preferred emission of *high energy* nucleons early on in the collision[2]. Thus, we expect that the squeeze-out preferably manifests

[1]For a reduced in-medium cross section, we expect shadowing to be less effective as in this case, the nuclear matter exhibits increased transparency as discussed in section 5.2.

[2]In contrast, for late emission times, equilibrium distributions will result in fewer nucleons with large momentum.

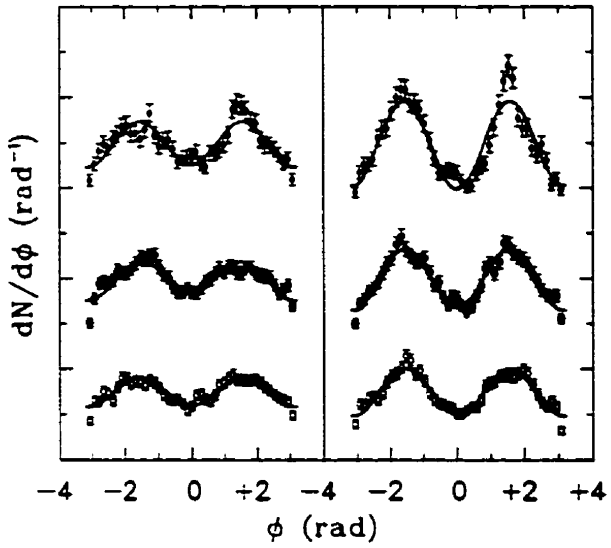

Figure 6.2: Mid-rapidity free proton azimuthal distribution obtained from simulated Bi+Bi events at E_k = 400 MeV. The left panel is for a momentum-independent mean field and the right is for a MDYI-type momentum-dependent mean field. Both are for soft equations of state. The distributions are plotted in transverse momenta bins. The lower, middle and upper curves are for 300 MeV/c< $p_\perp$ <400 MeV/c, 400 MeV/c< $p_\perp$ <500 MeV/c and 500 MeV/c< $p_\perp$ <600 MeV/c respectively. The solid lines are fits obtained by minimizing χ^2 per degree of freedom with respect to the fitting function in equation (6.1).

itself with high energy nucleons at the early stages in the collision over that of low or intermediate energy nucleons in the later stages of the collision. We can visualize this squeeze-out phenomena further by examining the azimuthal anisotropy of emitted nucleons. We show in figure 6.2 this quantity for collisions of ^{209}Bi+Bi at 400 MeV/A and $\hat{b} = 0.64$ for three regions of transverse momentum. From this figure, it is evident that the anisotropy peaks for values of $o = \pm 90°$ and is minimum for $o = 0°, 180°$. This is a case in which out-of-plane emission is preferred to that of in-plane emission. Note that o is the azimuthal angle out of the reaction plane.

For a quantitative picture of the anisotropy ratio, one typically fits the mid-

rapidity azimuthal distribution with a Fourier series [151, 152] of the form

$$\frac{dN}{d\phi} = A\,(1 + p_1 cos(\phi) + p_2 cos(2\phi) + \cdots)\,. \tag{6.1}$$

The coefficient p_1 characterizes the strength of the in-plane flow and the coefficient p_2 characterizes the strength of the anisotropy ratio. For preferred in (out) plane emission $p_2 > 0$ ($p_2 < 0$) as can be inferred from figure 6.2 and equation (6.1). With this definition of p_2, the anisotropy ratio is defined as $R = (1-p_2)/(1+p_2)$. As a by-product of figure 6.2, we note that higher transverse momenta bins produce a larger anisotropy ratio. This seems to concur with the qualitative picture we presented in the previous paragraph. It has been suggested [76] that this increasing anisotropy ratio with $p_\perp$ could be used to differentiate between momentum-independent and momentum-dependent mean fields. This hints at a differential analysis which we alluded to earlier in section 5.1. We will return to this shortly.

In section 5.1, recall that we examined momentum-dependent mean fields only. Section 5.2 examined the behaviour of both momentum-dependent as well as momentum-independent mean fields. In that case we found that the two parameterizations of the mean field did not give drastically different results. It turns out that the elliptic flow however, provides an excellent test bed to exploit the differences which arise from the two parameterizations of the mean field. For this, we show in figure 6.3 the ellipticity coefficient p_2 as a function of impact parameter for collisions of ^{56}Fe+Fe at $E_k/A = 400$ MeV for both momentum-independent as well as momentum-dependent mean fields. This figure indicates that while the two mean fields show similar behaviour at low impact parameter the high impact parameter behaviour is drastically different. In particular, p_2 for the momentum-independent mean field is only weakly dependent on the impact parameter as compared to the momentum-dependent mean field, the latter decreasing with impact parameter. This result agrees with the work in [31] for all impact parameters. Another systematic comparison[153] with data from Au+Au events[154] agrees with our result except for very high impact parameters. In that work p_2 showed a decrease for both momentum-independent and

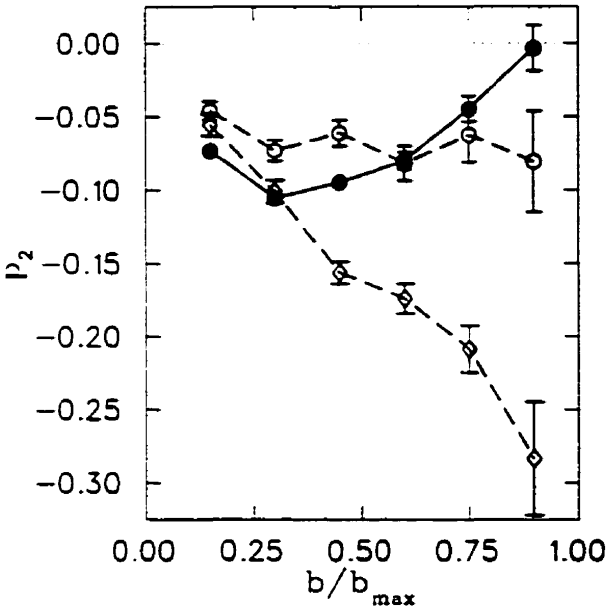

Figure 6.3: p_2 values extracted from equation (6.1) for simulated Fe+Fe events at $E_k/A = 400$ MeV as a function of impact parameter. The circles (diamonds) are for a momentum-independent (dependent) mean field. For the latter, we used a MDYI-type parameterization. For the momentum-independent mean field, the solid (open) points are for a stiff (soft) equation of state. The MDYI stiff mean field potential gives slightly larger (negative) value of p_2 than that of the soft equation of state at high impact parameter only.

momentum-dependent mean fields at $\hat{b} \geq 0.60$ and higher. The observed behaviour of p_2 as a function of transverse momenta at high impact parameter will serve to discriminate the two mean fields under investigation in this work.

For a systematic comparison with a measured elliptic flow signal, we now turn to a KAOS measurement of the proton anisotropy ratios[38]. This data set consisted of observations of Bi+Bi collisions at $E_k/A = 400, 700$ and 1000 MeV and impact parameters ranging from $b \sim 1.6 \rightarrow 11$ fm. In that work, a differential analysis was done, as the investigation presents the anisotropy ratio as a function of transverse momenta for several impact parameter bins. As we are interested in peripheral collisions, we selected measurements for the impact parameters $b = 8.7, 8.6, 9.0$ at incident energies of $E_k/A = 400, 700, 1000$ MeV respectively. The estimated impact parameters have an associated uncertainty of ± 0.3 fm. The values of p_2 extracted from our simulations have been calculated by fitting[3] the mid-rapidity proton distributions as shown in figure 6.2. The results for 400 MeV are displayed in figure 6.4. Here we show, as a function of transverse momenta, the anisotropy ratios obtained for both momentum-independent and momentum-dependent mean fields for both soft and stiff equations of state. We also show the results obtained when using an in-medium cross-section (density-dependent reduction of coefficient $\alpha = 0.20$ for momentum-independent mean fields and self-consistent for momentum-dependent mean fields). The experimental data indicate that the anisotropy ratio steadily increases with p_t.

Let us first consider the results obtained with the free-space cross section (top panel). We find that both the momentum-independent and the momentum-dependent mean fields produce anisotropy ratios that also increase with p_t, with the momentum-dependent result increasing faster compared to that of the momentum-independent result. The momentum-independent results show no sensitivity to the equation of state while the momentum-dependent results show a weak sensitivity, producing a

[3]For all fits presented in this figure, the χ^2 per degree of freedom varied from $\sim 0.5 \rightarrow 2.5$.

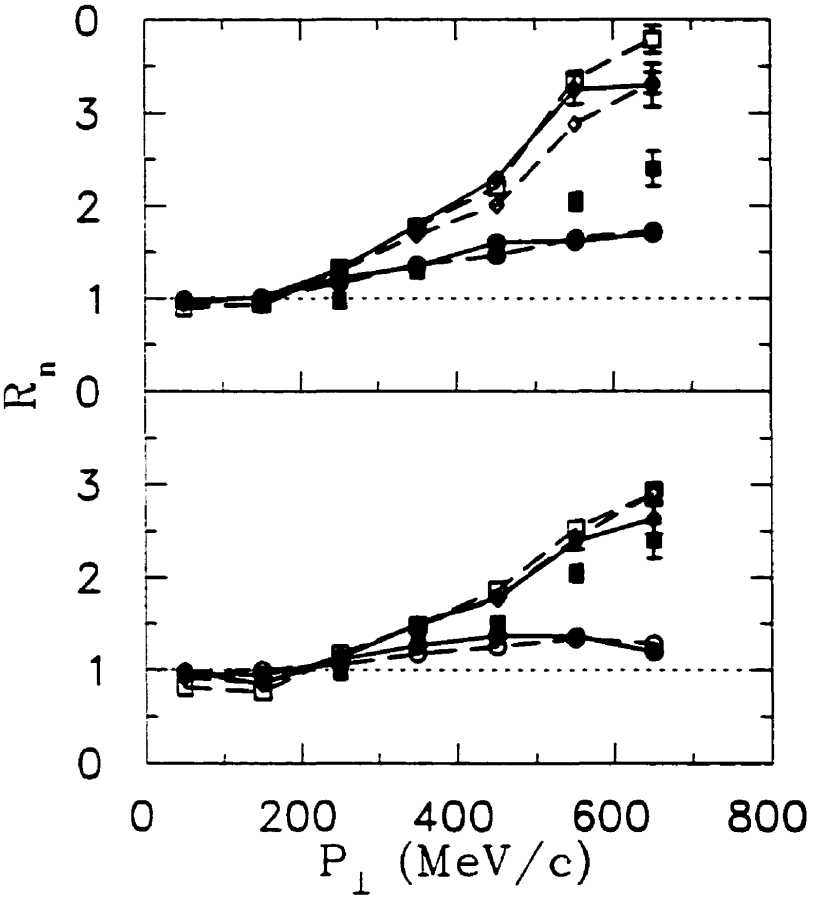

Figure 6.4: Experimental and simulated mid-rapidity free proton anisotropy ratios for Bi+Bi collisions at 400 MeV. The top (bottom) panel is for free-space (in-medium) nucleon-nucleon cross sections as described in the text. The circles are for momentum-independent mean fields. The diamonds are for MDYI-type momentum-dependent potentials and the open boxes are for GBD-type potentials. Open (solid) points are for soft (stiff) parameterizations of the mean field. The filled squares are the experimental results[38]. Note that a value of $R_n < 1$ implies preferred in-plane emission.

slightly higher anisotropy ratio for large transverse momenta with the stiff equation of state. This trend is in qualitative agreement with [153]. In addition, the GBD-type mean field also results in a larger anisotropy ratio than that of the MDYI-type mean field[4]. The figure indicates that the momentum-independent mean fields fit the observed anisotropy ratio for $p_\perp \leq 450$ MeV/c and underestimates it for $p_\perp > 450$ MeV/c. All momentum-dependent mean fields produce anisotropy ratios that overshoot the data.

We now turn to the results obtained with the in-medium cross section, we find that inclusion of the latter leads to dropping anisotropy ratios for all mean fields. Thus, the agreement with the momentum-independent mean field is worse and the agreement with the momentum-dependent mean field is better than without the in-medium cross section. Also, note that differences in the equation of state for the momentum-dependent interaction are smaller with an in-medium cross section than without (in fact, there is only an indistinguishable statistical difference at the highest transverse momenta of $p_t = 650$ MeV/c). The GBD-type momentum-dependent mean field still gives a larger anisotropy ratio than the MDYI-type mean field. Note that the GBD-type potential is more repulsive than the MDYI-type potential at high momenta as evidenced in figures 3.2 and 3.3. All momentum-dependent mean field results produce the same trends as seen in the data for all transverse momenta. Qualitatively, the simulations slightly over-predict the anisotropy ratio for all transverse momenta. For the momentum-independent mean field however neither the trend nor the magnitude of the data is reproduced when medium effects are included into the nucleon-nucleon cross section. From this figure, we find that the best agreement with the data is provided by the MDYI-type mean field (either stiff or soft) with an in-medium cross section. This analysis of Bi+Bi elliptic flow data was also analyzed with a transport model by Danielewicz[31]. In that work a different parameterization of the momentum-dependent mean field was used. The mean field used there also

[4]See figures regarding the optical potential for MDYI and (N)GBD.

reproduces the measured nuclear optical potential as displayed in figure 3.1. Our results agree with the results presented in that analysis for the momentum-independent mean field and for the momentum-dependent mean field with an effective mass of $m^*/m = 0.65$ at the Fermi surface.

The picture we have presented so far has accounted for the increasing mid-rapidity anisotropy ratio with transverse momenta. However, an explanation of the enhanced squeeze-out observed for momentum-dependent over that of momentum-independent mean field potentials has yet to surface. Consideration of the functional dependence on momenta that the momentum-dependent potentials respect indicates that the attractive momentum-dependent term is minimum when the denominator is maximum. The latter corresponds to $(\vec{p} - \vec{p}')$ for MDYI[5], assuming a maximum (c.f. equations (3.7) and (3.11)). Thus, leading[6] projectile and target nucleons will experience a rapid drop in the attractive part of the potential just as the two nuclei begin to interpenetrate. Compared to the potential experienced by a nucleon with a momentum-independent mean field, the potential for the momentum-dependent mean field at this point is more repulsive. In addition, figures 3.2 and 3.3 indicate that, for momentum-dependent potentials, the loss in the attractive part is stronger for larger momenta. Thus, for momentum-dependent potentials, higher momentum particles are less tightly bound to the surrounding nuclear medium than compared with the momentum-independent mean field potentials. In this scenario, we thus expect high momentum particles to escape more effectively from the former potential. This picture was indeed found to be the case.

Larionov [153] has also investigated the elliptic flow in this energy regime in conjunction with data from ^{197}Au+Au collisions from the FOPI-LAND collaboration[154]. In that work, a MDYI-type momentum-dependent potential was employed using the (Gaussian smoothed) test-particle method, however, they have to our knowledge

[5]For the GBD potential, this condition is for $(\vec{p} - < \vec{p}' >)$.

[6]The leading nucleons are more sensitive to the non-equilibrium situation present at the beginning of the collision.

assumed a local zero temperature nuclear matter distribution for the nuclei at all times. Thus, one might expect non-equilibrium effects to have a smaller effect in that model. Furthermore, as we do observe sensitivity to saturation properties (at densities greater than normal nuclear matter densities) of the momentum-dependent mean field potential (c.f. the GBD and MDYI differences in the mean field as shown in figures 3.2 and 3.3) this observable would seem to provide a nice test bed for different implementations of momentum-dependent potentials used in the literature. We stress that the effect observed in this work is a non-equilibrium effect that is not observed with the momentum-independent potential. In fact, the latter depends solely on density and does not care about the local momentum distribution, and is thus insensitive to the non-equilibrium momentum distribution of the nucleons.

Previously, we had mentioned that the self-consistent in-medium nucleon-nucleon cross section developed here gave substantially different predictions (for in-medium cross sections) than that of the simple density-dependent parameterization. Furthermore, we showed that these differences are more pronounced at higher energies. Thus, we turn to measurements of the Bi+Bi elliptic flow for laboratory bombarding energies of $E_k/A = 700$ and 1000 MeV/A. As we are interested in the behaviour of the in-medium cross section, we consider only the MDYI-type mean field of compressibility $K = 210$ MeV. In figure 6.5, we present the results we have thus obtained with the MDYI-type momentum-dependent mean field with and without the self-consistent in-medium cross section for energies of $E_k/A = 200$, 400, 700 and 1000 MeV. For 400 MeV/A, the results from figure 6.4 have been re-plotted. Our results indicate that at 700 MeV/A, we obtain excellent agreement with the data both with and with-out the in-medium cross section. At 1000 MeV/A, both parameterizations of the cross section agree with the data only for $p_\perp < 700$ MeV/c. For transverse momenta larger than this, our results start to diverge from the data trend. As far as the differences between the free space and in-medium cross sections are concerned, we find as expected, that the effect of the self-consistent in-medium correction to the

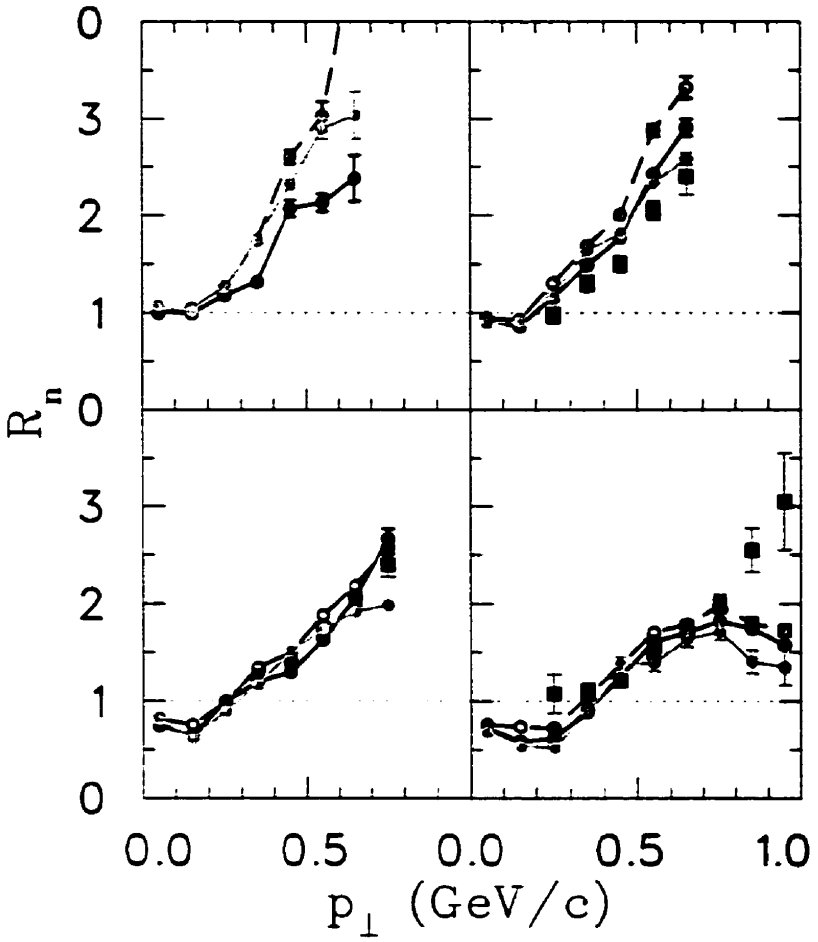

Figure 6.5: Same as figure 6.4 for the MDYI-type momentum-dependent mean field with and without the self-consistent in-medium cross section. We have used the soft equation of state of compressibility $K = 210$ MeV. Moving from left to right and top to bottom the laboratory bombarding energies shown are 200, 400, 700 and 1000 MeV per nucleon respectively. The filled squares are as in figure 6.4. The open circles, dark solid circles and shaded solid circles are for a free-space, self-consistent and density-dependent reduction in the in-medium nucleon-nucleon cross section. There are no data points available at $E_k/A = 200$ MeV.

free space cross section decreases with increasing bombarding energy. That is. the reduction of the elastic cross section due the self-consistent in-medium correction is more pronounced at low energies.

We have also employed the density-dependent modification to the in-medium cross section as discussed in section 3.2. The results for these calculations are also displayed in figure 6.5. Inspection of this figure indicates that this parameterization of the in-medium cross section is more pronounced at *high* energies, in contrast to the self-consistent in-medium cross section. This is as expected, since higher densities are probed at higher energies. As far as the anisotropy ratios are concerned. we find that (for $E_k/A = 400.\ 700.$ and 1000 MeV) the density-dependent in-medium modification differs from the self-consistent modification for high momentum nucleons only. However. for the lowest energy case ($E_k/A = 200$ MeV). the self-consistent in-medium modification produces a considerably smaller anisotropy ratio for all nucleons with transverse momenta in excess of 300 MeV/c. These results are consistent with figure 3.8. In addition. these results are also consistent with the spectator shadowing scenario previously mentioned. In this case. a smaller value of the in-medium cross section results in a larger nucleon mean free path which allows nucleons to escape into the reaction plane through the spectator matter with greater ease.

Chapter 7

Conclusion

The problem presented in this work, namely, a solution to the many-fermion problem for dynamical studies of collisions of heavy nuclei has been realized with a momentum-dependent lattice Hamiltonian solution of the BUU equation. This is the first realization of this model as applied to heavy ion collisions and as such represents significant advancement in continuing the predictive power of the BUU equation for low energy studies of collisions of heavy ions.

Of the main features, we have implemented a momentum-dependent mean field that closely matches the experimentally observed nucleon optical potential as well as modern detailed microscopic calculations of the nuclear equation of state. Furthermore, we have refined the two-body collision term by incorporating an in-medium effect on the nucleon-nucleon cross section that consistently takes into account the momentum-dependence of the nuclear mean field. This is the first time such an approach has been implemented in the study of heavy ion collisions and adds considerable flexibility to our model.

We have implemented our model at energies ranging from $\sim \epsilon_f$ to 1000 MeV/A. As previous implementations of the momentum-dependent BUU model at low energies had been plagued with energy conservation issues, the lattice Hamiltonian solution that we have adopted here for momentum-dependent mean fields represents

a great leap in the predictive power of the BUU equation in this energy regime. In particular, we have attained energy conservation far better than previous attempts with a momentum-dependent mean field. And as such the model developed here represents a state-of-the-art code suitable for low energy studies.

The experimental results that we have addressed in this work range from directed flow inversion and linear momentum transfer in the energy range of $E_k/A : 20 \rightarrow 150$ MeV/A, to elliptic flow in the energy range of $E_k/A : 200 \rightarrow 1000$ MeV/A. We have qualitatively reproduced the observed flow inversion at low energy. For the linear momentum transfer data, comparison with our model favours a MDYI-type momentum-dependent nuclear mean field of compressibility $K = 215$ MeV. In addition, these same observables are in better agreement with our model when we incorporate the self-consistent in-medium modification to the nucleon-nucleon cross section. For the higher energy elliptic flow data, we find that at energies of $E_k/A = 400$ and 700 MeV/A, the MDYI mean field potential supplemented with the self-consistent in-medium cross section successfully reproduces the experimentally observed signals. At the highest energy $E_k/A = 1000$ MeV, our model shows good agreement with the data for low transverse momenta. At high transverse momenta and high energy we begin to see our model breakdown.

We have demonstrated that the momentum-dependence (along with its implied in-medium modification of the nucleon-nucleon cross section) of the nuclear mean field plays a strong role in the study of elliptic flow. However, for all studies presented in this work, the compressibility has played a minor role. It has been shown that the directed flow inversion at low energy is however sensitive to all three aspects of the nuclear many body problem considered here: compressibility, momentum-dependence and in-medium nucleon-nucleon cross section. However, as these three aspects combine in a highly non-linear fashion, it is difficult to disentangle the role each plays. Since the self-consistent in-medium cross section with a momentum-dependent mean field is most heavily influenced at low momenta, further low energy

studies with our model should prove valuable.

To summarize, we have for the first time implemented a momentum-dependent lattice Hamiltonian solution to the BUU transport equation. Furthermore, we have also for the first time coupled this equation to a numerical solution of the self-consistent in-medium modification to the nucleon-nucleon cross section and obtained results that show good agreement with experiment.

Appendix A

TDHF and Vlasov equation formalisms

A.1 Two-Body Density Matrix

Starting from the totally anti-symmetric many-body wave function for an A nucleon system, from equation (2.2) written in the single-particle basis (c.f. [40] for a discussion), we have:

$$|\Psi>= a_1^\dagger a_2^\dagger \cdots a_A^\dagger |0> . \tag{A.1}$$

Let us transform the creation and annihilation operators from the general basis to the same basis that the many-body wave function is written as shown above. This yields

$$\begin{aligned} a_\alpha^\dagger &= \sum_i c_{\alpha i} a_i^\dagger \\ a_\beta^\dagger &= \sum_j c_{\beta j} a_j^\dagger \\ a_\delta &= \sum_k c_{\delta k}^* a_k \\ a_\gamma &= \sum_l c_{\gamma l}^* a_l . \end{aligned} \tag{A.2}$$

First, lets examine what the one-body density matrix looks like. Substituting equations (A.1) and (A.2) into the one-body density matrix, we get:

$$\begin{aligned}
\rho_{\alpha\beta} &= <\Psi|a_\beta^\dagger a_\alpha|\Psi> \\
&= \sum_{ij} c_{\beta j} c_{\alpha i}^* <\Psi|a_j^\dagger a_i a_1^\dagger a_2^\dagger \cdots a_i^\dagger \cdots a_A^\dagger|0> \\
&= \sum_{ij} c_{\beta j} c_{\alpha i}^* (-1)^{i-1} <\Psi|a_j^\dagger a_1^\dagger a_2^\dagger \cdots a_{i-1}^\dagger a_{i+1}^\dagger \cdots a_A^\dagger|0> \\
&= \sum_{i} c_{\beta i} c_{\alpha i}^* <\Psi|a_1^\dagger a_2^\dagger \cdots a_A^\dagger|0> \\
\Longrightarrow \rho_{\alpha\beta} &= \sum_i c_{\beta i} c_{\alpha i}^*. \qquad \text{(A.3)}
\end{aligned}$$

a sum of overlaps.

Now, we turn to the two-body density matrix from equation (2.7). Performing exactly the same steps for the one-body case we get:

$$\begin{aligned}
<\Psi|a_\alpha^\dagger a_\beta^\dagger a_\delta a_\gamma|\Psi> &= \sum_{ijlk} c_{\alpha i} c_{\beta j} c_{\delta k}^* c_{\gamma l}^* <\Psi|a_i^\dagger a_j^\dagger a_k a_l a_1^\dagger a_2^\dagger \cdots a_A^\dagger|0> \\
&= \sum_{ijlk} c_{\alpha i} c_{\beta j} c_{\delta k}^* c_{\gamma l}^* (-1)^{l-1} (-1)^{k-1} \\
&\times <\Psi|a_i^\dagger a_j^\dagger a_1^\dagger a_2^\dagger \cdots a_{k-1}^\dagger a_{k+1}^\dagger \cdots a_{l-1}^\dagger a_{l+1}^\dagger \cdots a_A^\dagger|0> \\
&= \sum_{ijlk} c_{\alpha i} c_{\beta j} c_{\delta k}^* c_{\gamma l}^* <\Psi|a_1^\dagger a_2^\dagger \cdots a_A^\dagger|0> (\delta_{jk}\delta_{il} - \delta_{jl}\delta_{ik}) \\
&= \sum_{l} c_{\alpha l} c_{\gamma l}^* \sum_k c_{\beta k} c_{\delta k}^* - \sum_k c_{\alpha k} c_{\delta k}^* \sum_l c_{\beta l} c_{\gamma l}^* \\
&= \rho_{\gamma\alpha}\rho_{\delta\beta} - \rho_{\delta\alpha}\rho_{\gamma\beta}. \qquad \text{(A.4)}
\end{aligned}$$

So we see that the two-body density matrix can be factorized into a linear combination of products of one-body density matrices. The above result was obtained using the fermion creation/annihilation commutation relations from equation (2.3).

A.2 TDHF Derivation

Starting from equation (2.10), and using equation (2.11), our aim is to show equation (2.12). We will break up the two terms in equation (2.10) into a kinetic and potential part and calculate them separately.

A.2.1 Kinetic term

Setting $\hat{V} = 0$ in $\hat{\mathcal{H}} = \hat{T} + \hat{V}$, equation (2.10) becomes:

$$\dot{\rho}_{\alpha\beta} = \frac{1}{i\hbar} < \Psi | [a^\dagger_\beta, \hat{T}] a_\alpha + a^\dagger_\beta [a_\alpha, \hat{T}] | \Psi > . \tag{A.5}$$

Expanding the commutators in the above and using equation (2.4), we obtain:

$$\begin{aligned} \dot{\rho}^{kin}_{\alpha\beta} &= \frac{1}{i\hbar} \sum_{\mu\nu} < \mu | \hat{t} | \nu > \\ &\times \; < \Psi | - a^\dagger_\mu a_\nu a^\dagger_\beta a_\alpha + a^\dagger_\beta a_\alpha a^\dagger_\mu a_\nu | \Psi > . \end{aligned}$$

Using the commutation relations from equation (2.3) to normal order the creation and annihilation operators and cancelling some terms, we obtain:

$$\dot{\rho}^{kin}_{\alpha\beta} = \frac{1}{i\hbar} \sum_{\mu} \left(< \alpha | \hat{t} | \mu > \rho_{\mu\beta} - \rho_{\alpha\mu} < \mu | \hat{t} | \beta > \right) . \tag{A.6}$$

A.2.2 Potential term

Setting $\hat{T} = 0$ in place of the $\hat{V} = 0$ from the last section, the TDHF equation becomes:

$$\dot{\rho}_{\alpha\beta} = \frac{1}{i\hbar} < \Psi | [a^\dagger_\beta, \hat{V}] a_\alpha + a^\dagger_\beta [a_\alpha, \hat{V}] | \Psi > . \tag{A.7}$$

Next, insert equation (2.5) for the total potential energy operator into the above and normal order the creation and annihilation operators. Rearranging indices, we arrive at the following result:

$$\begin{aligned} \dot{\rho}^{pot}_{\alpha\beta} = \frac{1}{i\hbar} \frac{1}{2} \sum_{\mu\sigma\nu} (\quad & (v_{\alpha\nu\sigma\mu} - v_{\nu\alpha\sigma\mu}) < \Psi | a^\dagger_\beta a^\dagger_\nu a_\mu a_\sigma | \Psi > \\ - \quad & (v_{\mu\nu\beta\sigma} - v_{\mu\nu\sigma\beta}) < \Psi | a^\dagger_\mu a^\dagger_\nu a_\sigma a_\alpha | \Psi >) \end{aligned}$$

Insertion of equation (A.4) into the above and collecting some terms we have the intermediate step:

$$\dot{\rho}^{pot}_{\alpha\beta} = \frac{1}{i\hbar} \sum_{\mu} \left(\left(\sum_{\sigma\nu} (v_{\alpha\nu\mu\sigma} - v_{\alpha\nu\sigma\mu}) \rho_{\sigma\nu} \right) \rho_{\mu\beta} - \rho_{\alpha\mu} \left(\sum_{\sigma\nu} (v_{\mu\nu\beta\sigma} - v_{\mu\nu\sigma\beta}) \rho_{\sigma\nu} \right) \right) . \tag{A.8}$$

We now utilize the single-particle potential energy operator introduced in equation (2.11). Pulling out these factors from the above equation, the time derivative of the potential part of the one-body density matrix reads:

$$\dot{\rho}^{pot}_{\alpha\beta} = \frac{1}{i\hbar}\sum_{\mu}\left(<\alpha|\hat{u}|\mu>\rho_{\mu\beta} - \rho_{\alpha\mu}<\mu|\hat{u}|\beta>\right). \tag{A.9}$$

Combining the results from equations (A.6) and (A.9), we arrive at the desired result given by equation (2.12).

A.3 Time derivative of the Wigner Transform

In this section, we seek to reduce the potential part of the time derivative of the Wigner function given in equation (2.16). We will use the assumption in equation (2.17), which asserts that our potential depends on position only (see footnote on page 15). With this assumption, we have:

$$\begin{aligned}\dot{f}^{pot}_{w}(\vec{r},\vec{p}) &= \frac{1}{i\hbar}\frac{1}{(2\pi\hbar)^3}\int d^3s\, e^{-i\vec{p}\cdot\vec{s}/\hbar} \\ &\times \left(u(\vec{r}+\vec{s}/2) - u(\vec{r}-\vec{s}/2)\right)\rho_{\vec{r}+\vec{s}/2,\vec{r}-\vec{s}/2}\end{aligned} \tag{A.10}$$

If we assume that the potential is infinitely differentiable, we can expand it about $\vec{r}$ using the exponential form for the Taylor series expansion (where $D \equiv d/dx$)

$$f(x+a) = \sum_{n=0}^{\infty}\frac{a^n D^n}{n!}f(x) = e^{aD}f(x).$$

Writing

$$\frac{\vec{s}}{2}e^{-i\vec{p}\cdot\vec{s}/\hbar} = \frac{i\hbar}{2}\nabla_{\vec{p}}e^{-i\vec{p}\cdot\vec{s}/\hbar},$$

equation (A.10) becomes:

$$\dot{f}^{pot}_{w}(\vec{r},\vec{p}) = \frac{2}{\hbar}\frac{1}{(2\pi\hbar)^3}\frac{1}{2i}\int d^3s \quad \left(e^{+i\hbar/2\nabla_{\vec{p}}\cdot\nabla_{\vec{r}}} - e^{-i\hbar/2\nabla_{\vec{p}}\cdot\nabla_{\vec{r}}}\right)u(\vec{r})e^{-i\vec{p}\cdot\vec{s}/\hbar}$$

$$\times\rho_{\vec{r}+\vec{s}/2,\vec{r}-\vec{s}/2},$$

with the caveat that $\nabla_{\vec{r}}$ acts only on the potential $u(\vec{r})$, and the $\nabla_{\vec{p}}$ acts only on the exponential $e^{-i\vec{p}\cdot\vec{s}/\hbar}$ appearing in the above equation[1]. Moving the quantity in large brackets and $u(\vec{r})$ outside the integral, we then arrive at equation (2.18), the desired result.

[1] As we have suppressed any momentum-dependence appearing in u, this is obvious, however, it must be kept in mind that our single-particle potential u allows for momentum-dependent terms.

Appendix B

Lattice Hamiltonian solution for GBD

B.1 Equations of Motion

Starting from the continuous version of the GBD mean field potential energy density from equation (3.10), and substituting equation (4.7) for the discrete form factor, the discretized version of the former reads:

$$V_\alpha^{GBD} = \frac{A}{2}\frac{\rho_\alpha^2}{\rho_0} + \frac{B}{\sigma+1}\frac{\rho_\alpha^{\sigma-1}}{\rho_0^\sigma} + \frac{C\rho_\alpha}{\rho_0}\sum_j \frac{R(\vec{r}_\alpha - \vec{r}_j)}{1+\left(\frac{\vec{p}_j - <\vec{p}>_\alpha}{\Lambda}\right)^2}. \tag{B.1}$$

where

$$<\vec{p}>_\alpha = \frac{\sum_j R(\vec{r}_\alpha - \vec{r}_j)\,\vec{p}_j}{\sum_j R(\vec{r}_\alpha - \vec{r}_j)}. \tag{B.2}$$

The GBD single-particle potential can be obtained from the potential energy density by unfolding one single-particle distribution function from the latter. This is the equivalent of taking the functional derivative of equation (3.11), with respect to $f(\vec{r},\vec{p})$. After substitution of the Lattice Hamiltonian phase space form factor from equation (4.7), we arrive at:

$$u_\alpha^{GBD}(\vec{p}_i) = A\left(\frac{\rho_\alpha}{\rho_0}\right) + B\left(\frac{\rho_\alpha}{\rho_0}\right)^\sigma$$

$$+\frac{C}{\rho_0}\sum_j \frac{R(\vec{r}_\alpha - \vec{r}_j)}{1+\left(\frac{\vec{p}_j - <\vec{p}>_\alpha}{\Lambda}\right)^2} + \frac{C\rho_\alpha}{\rho_0}\frac{1}{1+\left(\frac{\vec{p}_i - <\vec{p}>_\alpha}{\Lambda}\right)^2}, \qquad \text{(B.3)}$$

Now solving the equations of motion given by equation (4.9), using equations (B.1), (B.2) and (B.3) we get the following:

$$\begin{aligned}
\frac{\partial \vec{r}_i}{\partial t} = \frac{\vec{p}_i}{m} &+ \mathcal{N}_{ens}(\delta x)^3 \sum_\alpha R(\vec{r}_\alpha - \vec{r}_i) \\
&\times \left(\nabla_{\vec{p}_i} u_\alpha^{GBD}(\vec{p}_i) + \left(1 - \frac{R(\vec{r}_\alpha - \vec{r}_i)}{\rho_\alpha}\right)\vec{\mathcal{F}}_\alpha\right) \\
\frac{\partial \vec{p}_i}{\partial t} = &- \mathcal{N}_{ens}(\delta x)^3 \times \sum_\alpha \\
&\times \left(u_\alpha^{GBD}(\vec{p}_i) - (\vec{p}_i - <\vec{p}>_\alpha)\cdot\vec{\mathcal{F}}_\alpha\right)\nabla_{\vec{r}_i} R(\vec{r}_\alpha - \vec{r}_i). \qquad \text{(B.4)}
\end{aligned}$$

where

$$\vec{\mathcal{F}}_\alpha = \frac{2C\Lambda^2}{\rho_0}\sum_j \frac{R(\vec{r}_\alpha - \vec{r}_j)(\vec{p}_j - <\vec{p}>_\alpha)}{(\Lambda^2 + (\vec{p}_j - <\vec{p}>_\alpha)^2)^2}. \qquad \text{(B.5)}$$

If we now replace the finite form factor $R(\vec{r}_\alpha - \vec{r}_j)$ in equation (B.5) with the delta function form factor $\mathcal{N}_{ens}^{-1}\delta(\vec{r}_\alpha - \vec{r}_j)$, and keeping in mind that for an infinitesimal grid $<\vec{p}>_\alpha = \vec{p}_\alpha$, then the $\vec{\mathcal{F}}_\alpha$ in equations (B.4) is zero[1], and we obtain the test-particle equations of motion as discussed in section 4.2.2.

[1] In order for this to remain true, we must assume that no two particles have *exactly* the same configuration space coordinate $\vec{r}$.

Bibliography

[1] Bohr and Mottelson. *Nuclear Structure. Volume 1* (Benjamin. New York. 1969).

[2] G. Baym and C. Pethick. Ann. Rev. Astron. Astrophys. **17**, 415 (1979).

[3] S. E. Woosley and T. A. Weaver. Ann. Rev. Astron. Astrophys. **24**, 205 (1986).

[4] M. Prakash *et al.*. Phys. Rep. **280**. 1 (1997).

[5] V. R. Pandharipande. Phys. Lett. B **31**. 635 (1970).

[6] J. P. Blaizot, D. Gogny, and B. Grammaticos. Nucl. Phys. A **265**. 315 (1976).

[7] J. P. Blaizot. J. F. Berger. J. Deschargé. and M. Girot. Nucl. Phys. A **591**. 435 (1995).

[8] H. Satz. Nucl. Phys. A **544c**. 371 (1992).

[9] H. Meyer-Ortmanns. Rev. Mod. Phys. **68**. 474 (1996).

[10] G. D. Westfall *et al.*. Phys. Rev. Lett. **37**, 1202 (1976).

[11] S. Das Gupta and C. S. Lam. Phys. Rev. C **20**. 1192 (1979).

[12] S. Das Gupta and A. Z. Mekjian, Phys. Rep. **72**. 131 (1981).

[13] R. Serber. Phys. Rev. **72**. 1114 (1947).

[14] J. Cugnon. T. Mizatani. and J. Vandermeulen. Nucl. Phys. A **352**. 505 (1981).

[15] P. Bonche. S. E. Koonin. and J. W. Negele. Phys. Rev. C **13**, 1226 (1976).

[16] R. Y. Cusson *et al.*. Phys. Rev. Lett. **36**. 1166 (1976).

[17] P. Quentin and H. Flocard. Ann. Rev. Nucl. Sci. **28**, 523 (1978).

[18] J. Aichelin and H. Stöcker. Phys. Lett. B **176**, 14 (1986).

[19] J. Aichelin *et al.*. Phys. Rev. C **37**, 2451 (1988).

[20] J. Aichelin. Phys. Rep. **202**. 233 (1991).

[21] G. F. Bertsch. H. Kruse. and S. Das Gupta. Phys. Rev. C **29**. 673 (1984).

[22] G. F. Bertsch and S. Das Gupta. Phys. Rep. **160**. 189 (1988).

[23] J. C. Slater. *Quantum theory of atomic structure* (McGraw-Hill Book Company. Inc.. New York. 1960).

[24] N. H. March. *Self-consistent fields in atoms. Hartree and Thomas-Fermi Atoms* (Permagon Press. Oxford. 1975).

[25] E. K. U. Gross. E. Runge. and O. Heinonen. *Many Particle Theory* (Adam Hilger. Philadelphia. 1991).

[26] B. Friedmann and V. R. Pandharipande. Phys. Lett. B **100**. 205 (1981).

[27] V. R. Pandharipande and S. C. Pieper. Phys. Rev. C **45**. 791 (1992).

[28] C.-Y. Wong. Phys. Rev. C **25**. 1460 (1982).

[29] D. Persram and C. Gale. nucl-th/**9901019** (1999).

[30] R. J. Lenk and V. R. Pandharipande. Phys. Rev. C **39**. 2242 (1989).

[31] P. Danielewicz. Nucl. Phys. A **673**. 375 (2000).

[32] L. P. Csernai. *Introduction to Relativistic Heavy Ion Collisions* (Wiley. New York. 1994).

[33] W. Scheid. H. Müller. and W. Greiner. Phys. Rev. Lett. **32**. 741 (1974).

[34] V. E. Viola *et al.*. Phys. Rev. C **26**. 178 (1982).

[35] M. Fatyga *et al.*. Phys. Rev. C **32**. 1496 (1985).

[36] A. Fahli *et al.*. Phys. Rev. C **34**. 161 (1986).

[37] R. C. Lemmon *et al.*. Phys. Lett. B **446**. 197 (1999).

[38] D. Brill *et al.*. Z. Phys. A **355**. 61 (1996).

[39] J. C. Slater. Phys. Rev. **34**. 1293 (1929).

[40] P. Ring and P. Schuck. *The nuclear many-body problem* (Springer-Verlag, New York. 1980).

[41] U. Fano. Rev. Mod. Phys. **29**. 74 (1957).

[42] D. R. Hartree. Proc. Cambridge Phil. Soc. **24**, 89 (1928).

[43] G. F. Bertsch. *in:* Frontiers of Nuclear Dynamics (Plenum Press, New York, 1985).

[44] J. W. Negele. Rev. Mod. Phys. **54**, No. 4 (1982).

[45] G. E. Brown. *Unified Theory of Nuclear Models* (North-Holland Publishing Company, Amsterdam, 1964).

[46] T. Koopmans. Physica **1**, 104 (1934).

[47] W. H. Bassichis and M. R. Stanger. Ann. Phys. **66**, 457 (1971).

[48] H. Kohler and Y. C. Lin. Nucl. Phys. A **167**, 305 (1971).

[49] A. A. Vlasov. *Many Particle Theory and its application to Plasma* (Gordon and Breach, Science Publishers Inc., New York, 1961).

[50] C. Grégoire. in *Nuclear Matter and Heavy Ion Collisions*, edited by M. Soyeur, H. Flocard, B. Tamain, and M. Porneuf (Plenum Press, New York, 1989).

[51] C. Y. Wong, T. A. Welton, and J. A. Maruhn. Phys. Rev. C **15**, 1558 (1977).

[52] C. Y. Wong and J. A. McDonald. Phys. Rev. C **16**, 1196 (1977).

[53] E. Wigner. Phys. Rev. **40**, 749 (1932).

[54] M. Hillery, R. F. O'Connell, M. O. Scully, and E. P. Wigner. Phys. Rep. **106**, 121 (1984).

[55] E. A. Remler. Ann. Phys. **95**, 455 (1975).

[56] E. Wigner *et al.*, in *Lecture Notes in Physics: The Physics of Phase Space*, edited by Y. S. Kim and W. W. Zachary (Springer-Verlag, Berlin, 1986).

[57] G. M. Welke. Ph.D. thesis, SUNY, 1990.

[58] J. Randrup and B. Remaud. Nucl. Phys. A **514**, 339 (1990).

[59] L. W. Nordheim. Proc. Roy. Soc. **A119**, 689 (1928).

[60] E. Uehling and G. Uhlenbeck. Proc. Roy. Soc. London **A119**, 259 (1930).

[61] E. Uehling and G. Uhlenbeck. Phys. Rev. **43**, 552 (1933).

[62] C. Y. Wong and H. H. K. Tang. Phys. Rev. Lett. **40**, 1070 (1978).

[63] C. Y. Wong and H. H. K. Tang. Phys. Rev. C **20**, 1419 (1979).

[64] G. E. Brown and A. D. Jackson, *The Nucleon-Nucleon Interaction* (North-Holland Publishing Company, Amsterdam, 1976).

[65] R. Machleidt, in *Adv. Nucl. Phys. 19*, edited by J. Negele and E. Vogt (Plenum Press, New York, 1989).

[66] H. Yukawa, Proc. Phys. Math. Soc. Japan **17**, 48 (1935).

[67] T. H. R. Skyrme, Nucl. Phys. **9**, 615 (1959).

[68] D. Vantherin and D. M. Brink, Phys. Rev. C **5**, 626 (1972).

[69] L. Zamick, Phys. Lett. **45B**, 313 (1973).

[70] J. P. Blaizot, Phys. Rev. **64**, 171 (1980).

[71] G. M. Welke *et al.*, Phys. Rev. C **38**, 2101 (1988).

[72] C. Gale *et al.*, Phys. Rev. C **41**, 1545 (1990).

[73] L. P. Csernai, G. Fai, C. Gale, and E. Osnes, Phys. Rev. C **46**, 736 (1992).

[74] C. Gale, G. Bertsch, and S. Das Gupta, Phys. Rev. C **35**, 1666 (1987).

[75] M. Prakash, T. T. S. Kuo, and S. Das Gupta, Phys. Rev. C **37**, 2253 (1988).

[76] Q. Pan and P. Danielewicz, Phys. Rev. Lett. **70**, 2062 (1993).

[77] J. Aichelin *et al.*, Phys. Rev. Lett. **58**, 1926 (1987).

[78] F. Haddad *et al.*, Phys. Rev. C **52**, 2013 (1995).

[79] P. Hodgson, *The Nuclear Optical Potential* (World Scientific, singapore, 1994).

[80] M. M. Sharma *et al.*, Phys. Rev. C **38**, 2562 (1988).

[81] J. Zhang, S. Das Gupta, and C. Gale, Phys. Rev. C **50**, 1617 (1994).

[82] E. Baron, J. Cooperstein, and S. Kahana, Phys. Rev. Lett. **55**, 126 (1985).

[83] E. Baron *et al.*, Phys. Rev. Lett. **59**, 736 (1987).

[84] C. M. Perry and F. G. Perry, At. Data Nucl. Data Tables **17**, 1 (1976).

[85] M. Bauer, E. Hernández-Sladaña, P. E. Hodgson, and J. Quintanilla, J. Phys. G. **525**, 525 (1982).

[86] L. G. Arnold *et al.*, Phys. Rev. C **25**, 936 (1982).

[87] R. B. Wiringa, Phys. Rev. C **38**, 2967 (1988).

[88] R. B. Wiringa, V. Fiks, and A. Fabrocini, Phys. Rev. C **38**, 1010 (1988).

[89] I. E. Lagaris and V. R. Pandharipande, Nucl. Phys. A **359**, 331 (1981).

[90] J. Carlson, V. R. Pandharipande, and R. B. Wiringa, Nucl. Phys. A **401**, 59 (1983).

[91] R. Schiavilla, V. R. Pandharipande, and R. B. Wiringa, Nucl. Phys. A **449**, 219 (1986).

[92] B. Friedmann and V. R. Pandharipande, Nucl. Phys. A **361**, 502 (1981).

[93] A. Akmal and V. R. Pandharipande, Phys. Rev. C **56**, 2261 (1997).

[94] A. Akmal, V. R. Pandharipande, and D. G. Ravenhall, Phys. Rev. C **58**, 1804 (1998).

[95] R. B. Wiringa, V. G. J. Stoks, and R. Schiavilla, Phys. Rev. C **51**, 38 (1995).

[96] V. G. J. Stoks, R. A. M. Klomp, M. C. M. Rentmeester, and J. J. de Swart, Phys. Rev. C **48**, 792 (1993).

[97] J. L. Forest, V. R. Pandharipande, and J. L. Friar, Phys. Rev. C **52**, 568 (1995).

[98] B. S. Pudliner, V. R. Pandharipande, J. Carlson, and R. B. Wiringa, Phys. Rev. Lett. **74**, 4396 (1995).

[99] M. Prakash, T. L. Ainsworth, and J. M. Lattimer, Phys. Rev. Lett. **61**, 2518 (1988).

[100] C. H. Lee, T. T. S. Kuo, G. Q. Li, and G. E. Brown, Phys. Rev. C **57**, 3488 (1998).

[101] M. B. Tsang, G. F. Bertsch, W. G. Lynch, and M. Tohyama, Phys. Rev. C **40**, 1685 (1989).

[102] B.-A. Li and S. J. Yennello, Phys. Rev. C **52**, 1746 (1995).

[103] J. Cugnon, D. L'Hôte, and J. Vandermeulen, NIM **B111**, 215 (1996).

[104] G. F. Bertsch, W. G. Lynch, and M. B. Tsang, Phys. Lett. B **189**, 384 (1987).

[105] C. A. Ogilvie *et al.*, Phys. Rev. C **42**, 10 (1990).

[106] G. D. Westfall *et al.*, Phys. Rev. Lett. **71**, 1986 (1993).

[107] D. Klakow, G. Welke, and W. Bauer, Phys. Rev. C **48**, 1982 (1993).

[108] H. Feldmeier and P. Danielewicz (unpublished).

[109] S. S. Wong. *Introductory Nuclear Physics* (Prentice Hall, New Jersey, 1990).

[110] M. Warda, B. Nerlo-Pomorska, and K. Pomorski. Nucl. Phys. A **635**, 484 (1998).

[111] B.-A. Li, Z. Ren, C. M. Ko, and S. Yennello. Phys. Rev. Lett. **76**, 4492 (1996).

[112] R. Pak *et al.*, Phys. Rev. Lett. **78**, 1022 (1997).

[113] R. Pak *et al.*, Phys. Rev. Lett. **78**, 1026 (1997).

[114] C. W. de Jager, H. de Vries, and C. de Vries, At. Data Nucl. Data Tables **14**, 479 (1974).

[115] J. Aichelin and G. F. Bertsch, Phys. Rev. C **31**, 1730 (1985).

[116] D. Persram and C. Gale, in *Toward the Theory of Everything: MRST'98*, edited by J. Cline, M. Knutt, G. Mahlon, and G. Moore (American Institute of Physics, Woodbury, New York, 1998).

[117] D. Persram and C. Gale, in *High Energy Physics at the Millennium: MRST'99*, edited by P. Kalyniak, S. Godfrey, and K. Kamal (American Institute of Physics, Melville, New York, 1999).

[118] P. Danielewicz *et al.*, Phys. Rev. Lett. **81**, 2438 (1998).

[119] V. Greco, A. Guarnera, M. Colonna, and M. D. Toro, Phys. Rev. C **59**, 810 (1999).

[120] J. J. Monaghan, Comp. Phys. Rep. **3**, 71 (1985).

[121] I. J. Schoenberg, Quart. J. Appl. Math IV **401**, 45 (1946).

[122] J. J. Monaghan, Annu. Rev. Astron. Astrophys. **30**, 543 (1992).

[123] C. E. Aguiar, T. Kodama, T. Osada, and Y. Hama, hep-ph/**0006239** (2000).

[124] D. Klakow, G. Welke, and W. Bauer, nucl-th/**9304008** (1993).

[125] M. P. Allen and D. J. Tildesley, *Computer Simulations of Liquids* (Clarendon Press, Oxford, 1987).

[126] D. Kroftcheck *et al.*, Phys. Rev. Lett. **63**, 2028 (1989).

[127] J. P. Sullivan *et al.*, Phys. Lett. B **249**, 8 (1990).

[128] C. A. Ogilvie *et al.*, Phys. Rev. C **42**, R10 (1992).

[129] D. Kroftcheck *et al.*, Phys. Rev. C **43**, 350 (1991).

[130] G. D. Westfall *et al.*, Phys. Rev. Lett. **71**, 1986 (1993).

[131] R. Pak *et al.*, Phys. Rev. C **53**, R1469 (1996).

[132] R. Pak *et al.*, Phys. Rev. C **54**, 2457 (1996).

[133] G. F. Bertsch, W. G. Lynch, and M. B. Tsang, Phys. Lett. B **189**, 384 (1987).

[134] V. de la Mota, F. Sebille, B. Remaud, and P. Schuck, Phys. Rev. C **46**, 677 (1992).

[135] S. Soff *et al.*, Phys. Rev. C **51**, 3320 (1995).

[136] C. Liewen, Z. Fengshou, and J. Genming, Phys. Rev. C **58**, 2283 (1998).

[137] S. Kumar, M. K. Sharma, and R. K. Puri, Phys. Rev. C **58**, 3494 (1998).

[138] P. Danielewicz and G. Odyniec, Phys. Lett. B **157**, 146 (1985).

[139] B. Schürmann and W. Zwermann, Phys. Rev. Lett. **59**, 2848 (1987).

[140] P. Danielewicz *et al.*, Phys. Rev. C **38**, 120 (1988).

[141] E. Conlin *et al.*, Phys. Rev. C **57**, 1032 (1998).

[142] F. Haddad *et al.*, Phys. Rev. C **53**, 1437 (1996).

[143] H. Stöcker, J. A. Maruhn, and W. Greiner, Phys. Rev. Lett. **44**, 725 (1980).

[144] H. Gutbrod *et al.*, Phys. Lett. B **216**, 267 (1989).

[145] H. Gutbrod *et al.*, Phys. Rev. C **42**, 640 (1990).

[146] Y. Ollitrault *et al.*, Phys. Rev. D **46**, 229 (1992).

[147] M. B. Tsang *et al.*, Phys. Rev. C **53**, 1959 (1996).

[148] J. Barrette *et al.*, Phys. Rev. Lett. **73**, 2532 (1994).

[149] P. Danielewicz, Phys. Rev. C **51**, 716 (1995).

[150] Y. Ollitrault, Nucl. Phys. A **638**, 195c (1998).

[151] S. Voloshin and Y. Zhang, Z. Phys. C **70**, 665 (1996).

[152] A. M. Poskanzer and S. A. Voloshin, Phys. Rev. C **58**, 1671 (1998).

[153] A. B. Larionov, W. Cassing, C. Greiner, and U. Mosel, Phys. Rev. C **62**, 06461 (2000).

[154] D. Lambrech *et al.*, Z. Phys. A **350**, 115 (1994).